Measurements of Hot Electron Spectra From High Irradiance Laser Plasmas

Özgür Culfa

Doctor of Philosophy

University of York

Physics

March 2014

Abstract

This thesis presents measurements of the production of hot electrons during laser interactions in the irradiance range 10^{16} -10^{20} $\mathrm{W\,cm^{-2}}$. This intensity regime is accessible with modest ultra-short lasers at $\sim 10^{16}$ $\mathrm{W\,cm^{-2}}$ where resonance absorption dominates the electron acceleration. At the higher irradiances ($10^{18}-10^{20}$ $\mathrm{W\,cm^{-2}}$), petawatt class lasers are required where $\mathbf{J}\times\mathbf{B}$ electron acceleration occurs. Fast electron generation using the VULCAN Petawatt laser (irradiances $\sim 10^{20}$ $\mathrm{W\,cm^{-2}}$) and the LASERIX facility (irradiances $\sim 10^{16}$ $\mathrm{W\,cm^{-2}}$) have been investigated. Using the Vulcan Petawatt laser, with pulse duration of 1 - 2 ps at intensities greater than 10^{20} $\mathrm{W\,cm^{-2}}$, electron energies up to 120 MeV with temperatures 20 - 30 MeV have been observed. A pre pulse was used to create an expanding plasma in which the high irradiance pulse was incident and the scale length of the pre pulse produced plasma was measured using optical probing. It was found that the number of hot electrons produced at $10^{20}\,\mathrm{W\,cm^{-2}}$ linearly increases with the measured pre pulse plasma scale length indicating that the electron acceleration is dependent on the pre-pulse plasma volume. 2D PIC simulations are in agreement with experimentally measured temperatures, while 1D PIC simulations only agree for shorter scale length plasmas ($L \lesssim 7.5\,\mu\mathrm{m}$). Plasma channels are formed with longer scale length plasmas, but these channels do not result in greater acceleration of electrons as they are not sufficiently narrow. The role of hot electrons in heating solid targets is experimentally examined and it is found that radiation effects on target heating when a pre pulse is present dominate over hot electron heating.

Contents

List of Figures

Acknowledgements

First and foremost I would like to thank my supervisor Professor Greg Tallents for his patience and the support and the guidance he has given me throughout this work. His experience and knowledge has been invaluable throughout the completion of this thesis.

During my time at the University of York I have had great opportunity to know and work with amazing people in the laser plasma physics group namely Andy Rossall, Lucy Wilson, Mohammed Shahzad, Reem Alraddadi, Robert Crowston, Rachel Dance and Tom Fox. In particular, I am grateful to Nigel Woolsey for his support and advice in my first year and Erik Wagenaars for his advice and leadership in the VULCAN experiment. I am grateful to Chris Ridgers for his advice to improve the work presented in this thesis and his help with using EPOCH PIC code. I would also like thank John Pasley for his great lectures and friendship. I would like to extend my thank to Zulfikar Najmudin for his advice and comments to improve my thesis.

I would also like to thank the rest of the fusion DTN students especially namely Lee Morgan, Jack Snape, Tom Williams, Andy Allen and Peshwaz Abdoul for their encouragement and support over the last 3 and half years and Selahattin Kosunalp for his support and friendship throughout my time in York.

I am grateful for the support and supplying PIC code I have used in this work to Alex Robinson. I would like to extend my thanks to Margaret Notley, Nicola Booth, Rob Clarke, James Green, Kate Lancaster and all Target Area staff and engineering department at the Central Laser Facility without their assistance the experiments would not have been a success. I would like to extend my thanks to C.D. Murphy and the group he worked with to design the electron spectrometer which is used in the work presented in this thesis and for sharing the magnetic map of the spectrometer with me. I am also grateful to EPOCH code developers for giving free access and their supports.

Finally, I would like to thank my sister İlknur and my mum Zeliha for their patience, encouragement and support over the years.

Author's Declaration

I declare that the work presented in this thesis, except where otherwise stated , is based on my own research and has not previously been submitted for a degree at this or any other university.

Parts of the work presented in this thesis have been published in some of the papers listed in Appendix A.

Özgür Culfa

March, 2014

For my loving family ...

Chapter 1

Introduction

The potential for clean and safe energy from nuclear fusion has been apparent for many years. There are two main approaches: Magnetic Confinement Fusion (MCF) [1] and Inertial Confinement Fusion (ICF) [2, 3]. While MCF confines hot plasma fusion fuel with magnetic fields, ICF involves compressing a spherical target containing deuterium - tritium fuel with lasers or x-rays and relying on a disassembly time for the fusion (DT) reactions to occur.

Laser fusion was brought to the world's attention in 1972 with the publication of a classic, but over-optimistic paper in Nature by Nuckolls et al [4]. Nuckolls describes how a pellet containing deuterium and tritium isotopes of hydrogen, could be compressed to high densities sufficient for fusion to occur after irradiation by laser beams. When the laser energy is absorbed and converted into thermal plasma energy, the pellet shell material ablates radially outwards and momentum conservation results in the compression of the fuel initially frozen on the inside of the pellet shell. Due to the spherical symmetry, the fuel implosion, causes densities ρ of several hundred g cm^{-3} and temperatures T_e of 10 keV or higher.

Fast ignition and particle acceleration [5, 6] has been proposed as a technique to reduce the laser energy required for ICF. After compressing the deuterium-tritium fuel to a lesser extent than proposed by eg Nuckolls, an ultra intense short pulse laser is incident into the plasma to generate a beam of fast electrons. The fast electrons are accelerated near the critical density, but reach the compressed DT fuel and deposit their energy generating a hot spot which ignites the DT fuel.

The cone guided geometry for fast ignition is a further step from the basic fast ignition method. Here, a hollow cone is embedded in the fuel capsule (see figure 1.2). The cone provide an open evacuated path free of coronal plasma for the ignitor laser beam and allows the laser beam to interact closer to the hot compressed fuel [6, 7].

Hot electrons can also have a deleterious effect on inertial fusion [8]. Hot electrons can preheat the fuel, potentially degrading compression in the implosion. The amount of preheat depends on the hot electron source characteristics and the time duration over which electrons can deposit energy into the fuel. Preheating the fuel makes the compressibility of the pellet more difficult.

In laser interactions with a solid target, generated hot electrons can penetrate through the target and ionise a proton layer on the back of the target. Only a small fraction of hot electrons can escape into the vacuum behind the target due to the capacitance of target. Electric potential sheaths can form due to the hot electrons which induce a quasi static electric field on both sides of the target. These sheaths can accelerate protons and ions up to tens of MeVs [9, 10].

1.1 Inertial Confinement Fusion

There are two ICF approaches with lasers to compress DT to the necessary density for fusion to occur: direct drive and indirect drive. In direct drive, the laser is directly incident on the fuel capsule, driving the implosion due to ablation of the shell. In indirect drive, lasers interact in a hohlraum (black body cavity) of high Z material and produces thermal x-rays which irradiate the fuel capsule (see figure 1.1 (a) and (b)) and cause ablation of the capsule shell and subsequent compression.

In both methods, energy should be transferred to the ablator in a short time scale ($\sim$ ns). Successive shock waves are used to enable the fuel to be compressed adiabatically as this requires less energy than attempting to compress heated fuel. The required temperature for fusion ignition with DT is around 5 keV as there are then sufficiently energetic D and T atoms in the tail of the Maxwellian distrubution of speeds for the fusion reactions to produce more energy than bremsstrahlung losses.

Indirect drive is less efficient than direct drive due to the need to convert laser energy to x-rays. Total laser to capsule coupling is around 10 - 15 % [3]. However, indirect drive can heat the target uniformly and reduce instabilities.

With the DT reaction, 80 % of the released energy is in the form of neutron kinetic energy. The neutrons leave the plasma without any interaction. The rest of the released energy is associated with the kinetic energy of the alpha particles. The alpha particle energy is transferred to the plasma and causes further plasma heating enabling an ignition hot spot to cause the fusion of most of the remainder of the surrounding fuel.

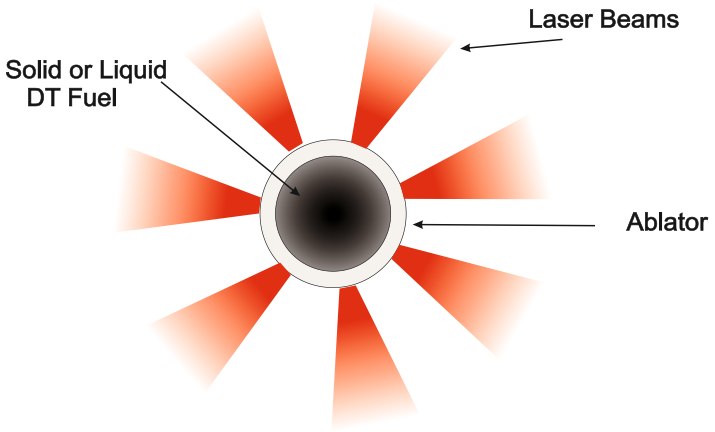

(a)

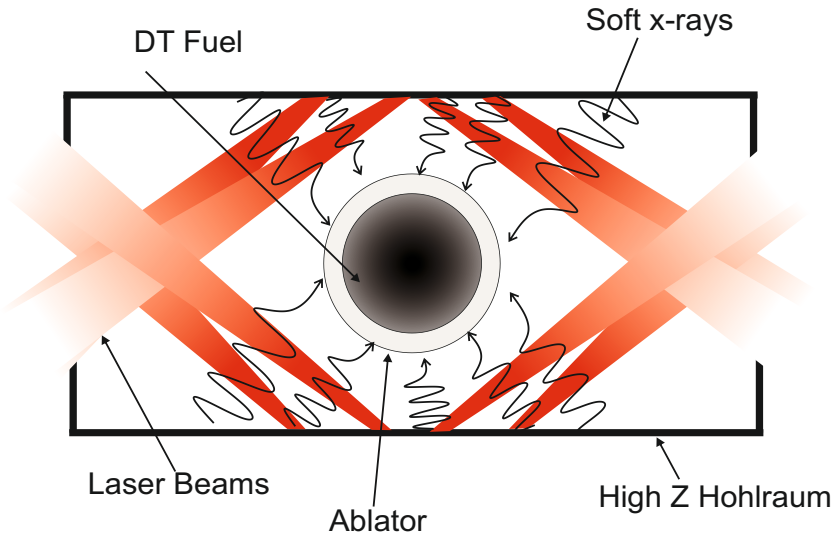

(b)

Figure 1.1: Schematic illustration of (a) direct and (b) indirect drive inertial confinement fusion.

Thermonuclear ignition of the fuel occurs when internal heating by α particles exceeds the losses due to radiation, thermal conduction and expansion. A certain temperature is needed for the ignition process which has a dependence on the fusion fuel and loss mechanisms such as bremsstrahlung. Radiative losses by bremsstrahlung emission is the dominant energy loss mechanism.

The produced alpha particles move through the plasma and deposit their energy via Coulomb collisions with other charged particles. When alpha particles deposit their energy into the DT plasma, this energy drives an outward propagating burn wave.

1.2 Fast Ignition

Recent developments in laser technology have allowed laser pulse powers to reach the petawatt level (10^{15} W). Fast ignition involves highly energetic fast electron beams produced by petawatt class lasers. The generation of fast electrons by lasers, the energy transport of hot electrons through dense plasma and plasma instabilities generated by hot electrons are key issues of investigation in the fast ignition approach.

In the fast ignition scheme, lasers heat the fusion target surface rapidly and ablation of the surface compress the fuel. When compression reaches the maximum level, an ultra intense laser with a short pulse (1-10 ps) can be used to ignite a small part of the fuel. Thermonuclear burn can then spread out through the compressed DT fuel. One of the main advantages of the fast ignition method is that lower compressed densities are needed. Instabilities are likely to play a less active role as the compressed density is lower.

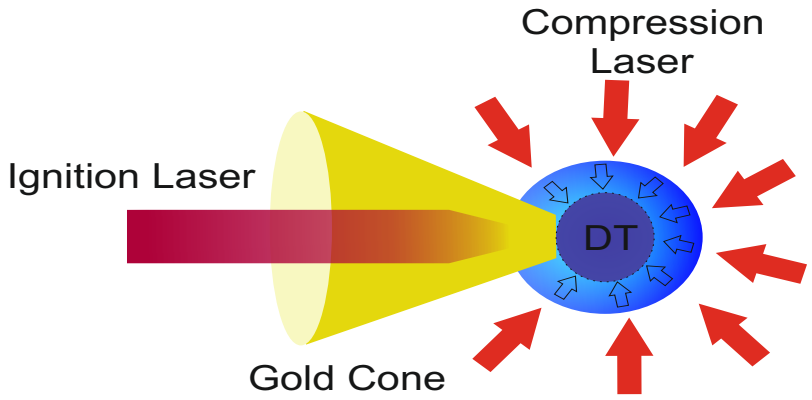

Figure 1.2: Schematic illustration of Fast Ignition method.

One of the main problems of fast ignition is finding a way to bring the laser beam close to the fuel core. One proposal is to bore a hole into the overdense plasma by another laser beam. Another approach is to guide the laser beam by a gold cone which is embedded in the DT pellet (see figure 1.2) [11–13].

A high conversion efficiency from laser to hot electrons to ignite the fuel is one of the most important criteria for fast ignition. At the required laser parameters for fast ignition (irradiance $> 10^{18}$ W cm^{-2} with 1 μm laser wavelength and pulse duration of 1 to 10 ps) the laser electron coupling is around 20 % (independent of pulse duration) [14]. Generated hot electrons typically have a Maxwellian spectrum, characterised by a temperature T_h. Laser solid interaction studies show that T_h has a dependence on a laser intensity and wavelength [15] (see section 2.3). Since the hot electrons can heat the fusion fuel, it is essential to understand hot electron heating on targets for different materials and laser intensities.

In chapter 6, we have introduced laser solid interactions with moderate intensities (10^{16} W cm^{-2}) and investigated hot electron generation as well as hot

electron target heating for ultra short laser solid interactions.

One of the main concerns in producing fast electrons for fast ignition is the contrast level of the laser and how much preplasma the laser pedestal will create in the cone. The preplasma may cause filamentation or self focussing and push the critical surface away from the tip of the cone which changes the properties of the electrons produced [16].

Laser intensity, wavelength and angle of incidence affect the electron acceleration mechanisms (see section 2.2). Electron acceleration at lower laser intensities ($< 10^{18}$ W cm^{-2}) is generally understood, but for the relativistic intensities ($> 10^{18}$ W cm^{-2}) electron acceleration mechanisms are under active investigation (see section 3.5).

In the work presented in this thesis, we have investigated the effect of controlled laser pre-pulse and the main pulse on electron generation and how preformed plasma affects the hot electron temperatures (chapter5).

It is clear that the study of the generation and transport of fast electrons is essential to understanding high intensity laser solid interactions since they are a major factor in the absorption and transport of the laser energy.

We have seen that laser absorption in a plasma can create hot electrons. Since these hot electrons can penetrate through the centre of the target, fuel can be preheated and become less compressible if the hot electrons arrive before or during the compression.

Hot electron generation is also important in other applications of laser plasmas such as in fast ion generation. In solid target experiments with focussed intensities approaching 10^{20} W cm^{-2}, hot electron generation and energetic protons have been observed on the back and front side of the target [9, 10, 17–21].

The generated hot electron cloud in the laser produced pre plasma, can accelerate through the target and ionise the proton layer on the back of the target. Only a small fraction of hot electrons can escape into the vacuum behind the target due to the capacitance of target. Once the target is sufficiently charged, escaping from the target is difficult even for MeV electrons. Those electrons are confined to the target and circulate back and forward through the target so that the charge separation field on both sides of the target enlarges. The induced electric field accelerates protons and target ions to tens of MeVs over distances of tens of μm (associated with the Debye length of the plasma). These highly energetic ion beams are preferentially accelerated in a direction perpendicular to the emitting surface. The mechanism is known as Target Normal Sheath Acceleration (TNSA).

A new laser driven ion acceleration mechanism using ultra thin targets, known as laser breakout afterburner (BOA), has recently received attention [22–24]. This mechanism can be divided into two stages. The first stage is similar to the TNSA mechanism. The generated hot electrons set up a sheath field on the rear side of the target. For a sufficiently thin target ($\approx$ 10 s of nm) the laser converts many electrons into hot electrons, resulting in the overdense target becoming underdense and also introducing a longitudinal electric field. Secondly, relativistic mass increase of electrons can increase the laser critical density so that the target becomes transparent to the laser and electrons at the rear of the target are further accelerated. This after burner mechanism accelerates ions to much higher energies using similar laser intensities to TNSA experiments. Another ion acceleration mechanism is known as Radiation Pressure Acceleration (RPA). Here a large accelerating field arises by charge separation sustained by the ponderomotive pressure of laser radiation on the electrons. The laser solid interaction causes

a rapid deformation on the plasma surface and ions are accelerated into the target by a hole boring process. If the target is sufficiently thin, the hole boring extends to the rear target surface during the laser pulse, and the laser can accelerate all ions in the laser path and the whole target is pushed in the direction of the laser beam. This is sometimes called the "light-sail" regime [25–27]. Applications of these accelerated ions are the subject of significant research [21, 28–30].

In the work presented in this thesis, we have investigated electron acceleration in an "ion channel" produced by the laser ponderomotive force and compared our theoretical approach to previous work for moderate laser intensities ($10^{16} - 10^{17}\,\mathrm{W\,cm^{-2}}$) (chapter 3).

1.3 Chapter Outline

The outline of this thesis is as follows. Chapter 2 covers a general overview of background relevant to this work: the absorption of laser pulses in plasmas, fast electron generation, the characteristic of fast electrons and laser wakefield acceleration, fast electron penetration in solids and plasma emissivity. A discussion of the simulation codes used in this work is also presented.

Chapter 3 investigates a single electron motion in an electromagnetic field. The effect of the geometry of an imposed electric field on electron acceleration due to the propagation of an electromagnetic wave has been studied.

Chapter 4 details diagnostics used in the experiments presented in this work. An electron spectrometer and optical probe shadowgraphy for the VULCAN experiment are discussed. Errors for the electron spectrometer response have been determined. An optical probe shadowgraphy technique is examined. X-ray diodes

are discussed and their role in plasma electron temperatures described.

Chapter 5 presents the result obtained from a VULCAN experiment. Electron spectra and shadowgraphy analysis have been explained and compared with 1D and 2D PIC code simulations. Experiment and simulations are in approximate agreement with lower scale lengths but increasing scale length causes a drop in the electron temperature which could not be explained with 1D simulations. 2D simulation suggest that laser filamentation in the plasma occur and affects the electron temperatures produced. The number of electrons per solid angle has been found to increase linearly with scale length.

Chapter 6 represents the results from an experiment using an EUV laser and fs laser irradiation. X-ray diodes have been used to measure the electron temperature from x-rays emission due to bremsstrahlung. The laser was operated with varying angles of incidence onto solid targets. The EPOCH code was run for different angles and different scale lengths and comparison of the simulation to compare to the experimental results. Generated electron temperatures are in agreement for a 0.65 μm scale length density profile. Analytic solutions of resonance absorption as well as HYADES expectations regarding plasma scale length show that the plasma scale length is approximately 0.6 μm at 30° incidence angle which agrees with the experimental data. Electron target heating was investigated to show that the generated fast electrons do not significantly heat the target. Chapter 7 presents the overall conclusion of this work.

1.4 Work Undertaken by the Author

The author operated and enhanced the code written by G.J.Tallents which simulates single electron motion in an electro magnetic field detailed in chapter 3 and modelled the electron behaviour in a static electric field inside a formed channel.

The author determined precise analytic solution for the dispersion of a circular geometry B field electron spectrometer (chapter 4). To his knowledge, this had not been calculated previously. The calculated dispersion agreed with empirical and approximate formulas developed by others. Original error estimates for the electron spectrum were also evaluated. A magnetic field map which gives information about fringing field effect recorded by C.D.Murphy has been used to deduce the effects of fringing fields on the electron spectrometer dispersion.

Chapter 5 and 6 include experimental and theoretical work. The author was involved in the VULCAN Petawatt laser experiment and ran the diagnostics to obtain the data from the experiment detailed in chapter 5. The author has performed all the analysis for this experiment and ran the simulation codes. The diagnostic which is used to determine the hot electron energy (electron spectrometer) was designed by C.D. Murphy and the group he worked with at Imperial College.

The experiment discussed in chapter 6 was undertaken on the LASERIX facility. The author was not present during the experiment, but all analysis and simulation concerning the x-ray diagnostic as determined in chapter 6 were undertaken by the author. HYADES simulations run by L.A.Wilson are presented in this chapter and the diagnostic (silicon diode) discussed in this chapter were run by M.Shahzad and A.K.Rossall during the experiment.

Chapter 2

Laser Plasma Interactions

2.1 Introduction

This chapter reviews some background physics behind the work of the thesis. Laser ablation of solid targets, including electromagnetic wave propagation in plasmas and different processes which occur in laser produced plasmas are reviewed. Laser absorption processes and their relevance to particle acceleration and inertial confinement fusion (ICF) in particular are discussed.

2.2 The Absorption of Intense Laser Pulses in Plasmas

2.2.1 Electromagnetic Wave Propagation in Plasmas

The linear dispersion relationship in a uniform plasma is given by $\omega^2 = \omega_{pe}^2 + k^2c^2$ for the planar electromagnetic wave with electric field variation $\mathbf{E}\,(\mathbf{z}, \mathrm{t})=$

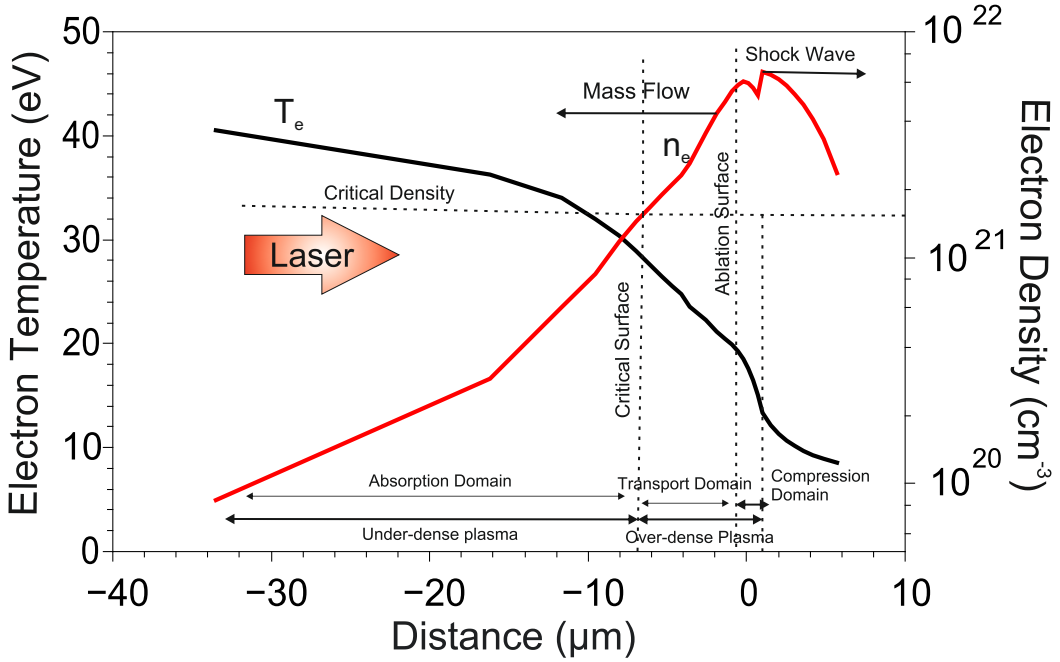

Figure 2.1: Different regions and typical electron temperatures T_e and electron densities n_e in a laser plasma interaction, as simulated by the 1D radiation hydrodynamic code HYADES [32] for a pre-pulse of irradiance 1.5×10^{15} W cm^{-2} which is followed later by 20 ps before a main pulse of irradiance 3×10^{16} W cm^{-2}. Both pulses have duration of 35 fs in a Gaussian shaped pulse of wavelength 0.8 μm. Electron temperature and density are plotted at 100 ps after the pre-pulse is incident on the target. (Code output supplied by L.A.Wilson)

$\mathbf{E_o} \exp[\mathrm{i}(\mathbf{k}.\mathbf{z} - \omega \mathrm{t})]$ where ω_{pe} is the plasma frequency. Here $\mathbf{k}$ is the wave vector and ω is the angular frequency. The plasma frequency is defined by $\omega_{pe}^2 = (n_e e^2/m_e \varepsilon_0)$, where n_e is the electron density, m_e is the mass of the electron, e is the electric charge and ϵ_0 is the permittivity of free space. A critical density which is given by $n_c = 4\pi^2 c^2 m_e \varepsilon_0 / (e^2 \lambda^2)$ cm^{-3} $= 1.1 \times 10^{21}$ $(1\mu\mathrm{m}/\lambda)^2$ cm^{-3} can be defined as the maximum density where light of wavelength λ can penetrate [31]. The plasma where the electron density is less than the critical density is referred to as under-dense and the region where the electron density is greater than the critical density is referred to as over-dense.

Different laser absorption mechanisms occur in different plasma regimes. In underdense plasmas, laser absorption is primarily due to inverse bremsstrahlung with the laser intensities of $10^{14} - 10^{17}\,\mathrm{W\,cm^{-2}}$ [33]. At the critical surface, resonance absorption can occur [34]. Figure 2.1 shows the different regions of the plasma after irradiation by a laser pulse. Absorbed energy from the laser pulse is transported to the ablation surface at the solid target. This energy transfer occurs mainly via thermal conduction. However, some electrons gain higher energies (called "hot electrons" see section 2.3) and these higher energetic electrons can propagate further into the solid than thermal conduction and pre heat the target. Radiation from hot expanding plasma also penetrates the solid target and can heat it before thermal conduction heating can penetrate.

Due to momentum conservation, shock waves generated by ablating plasma can propagate away from the absorption region into the solid target and cause compression of solid material (see figure 2.1). If the ablating plasma is isothermal, the density profile of the plasma is exponential with $n_e = n_0\,\exp(-\frac{z}{L})$ where n_e is electron density, n_0 is the solid density and L is a plasma scale length given approximately by $L = c_s t$ where c_s is the speed of sound and t is time [31].

At higher irradiances, the laser pulse can apply light pressure P_L on the plasma [35, 36] such that;

$$P_L = \frac{I_L}{c}\,(1+R) \approx 3.3\,\mathrm{Mbar}\left(\frac{I_L}{10^{16}\,\mathrm{W\,cm^{-2}}}\right)(1+R) \tag{2.1}$$

where R is the reflectivity of the laser. Density gradients near the critical surface can steepen due to the effect of light pressure as well as the localised heating at the critical density [35, 36]. The laser electromagnetic propagation in a plasma can be

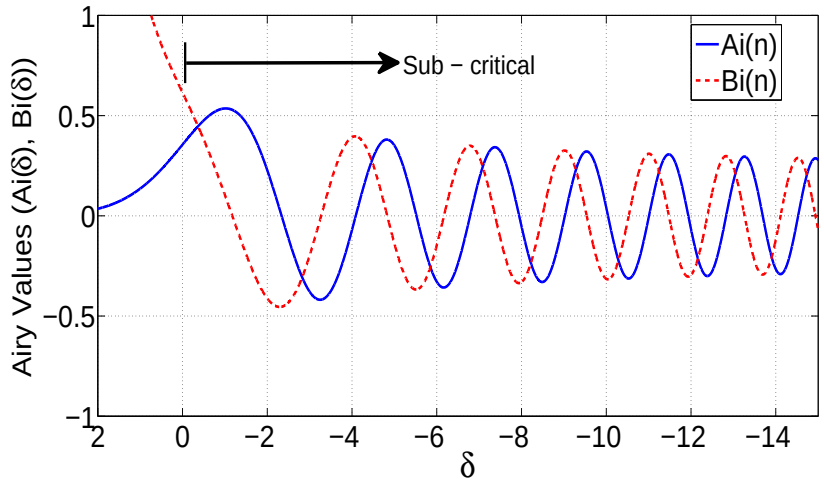

Figure 2.2: Airy values as a function of δ. $Ai(\delta)$ represents the electric field of the laser pulse.

solved analytically by assuming a linear density profile [31] with $n_e = n_c \frac{z}{L}$, where $z = 0$ is the plasma critical density and L is the plasma scale length. With a linear electron density profile, the dielectric function of a plasma, $\epsilon = 1 - \frac{n_e}{n_c} = 1 - \frac{z}{L}$ and applying to the wave equation gives

$$\frac{d^2\mathbf{E}(z)}{dz^2} + \frac{\omega^2}{c^2}\left(1 - \frac{z}{L}\right)\mathbf{E}(z) = 0 \quad . \tag{2.2}$$

A change of variables to the dimensionless variable $\delta = \left(\frac{\omega^2}{c^2 L}\right)^{1/3}(z - L)$ gives

$$\frac{d^2\mathbf{E}(\delta)}{d\delta^2} - \delta\mathbf{E}(\delta) = 0 \tag{2.3}$$

which is known as the Stokes differential equation. This differential equation defines the Airy functions, Ai and Bi, such that;

$$E(\delta) = \alpha Ai(\delta) + \beta Bi(\delta) \tag{2.4}$$

where α and β are amplitude coefficients found using the plasma boundary conditions. Figure 2.2 shows the values for Ai and Bi as a function of δ. As $Bi(\delta) \to \infty$ as $\delta \to \infty$, $\beta = 0$ in equation 2.4 at $\delta = 0$. The laser cannot propagate behind the critical density of the plasma. Therefore the electric field behaviour of the laser inside the plasma can be represented by the Airy function, $Ai(\delta)$. Features observed in figure 2.2 for $Ai(\delta)$ found in most laser-plasma experiment include an increase in electric field amplitude near the critical density and an evanescent wave decaying in amplitude at densities above the critical density.

2.2.2 Inverse Bremsstrahlung

One of the most important mechanisms for laser plasma coupling is inverse bremsstrahlung. In this process, laser light is absorbed up to the critical surface as the laser electric field oscillates electrons in the plasma. Electron-ion collisions convert the oscillation energy to thermal energy. Bremsstrahlung and inverse bremsstrahlung processes are inverse processes related in their rates by detailed balance. In bremsstrahlung, a free electron is accelerated in the field of an ion and emits a photon, while in inverse bremsstrahlung a photon is absorbed by an electron and causes electron acceleration in the field of an ion.

For the under dense plasma region, electron acceleration $\frac{d\mathbf{v}}{dt}$ due to a laser electric field $\mathbf{E}$ can be modelled by;

$$\frac{d\mathbf{v}}{dt} = \frac{-e\mathbf{E}}{m_e} - \nu_{ei}\mathbf{v} \tag{2.5}$$

where ν_{ei} is the electron-ion collision frequency, $\mathbf{v}$ is the electron velocity and e and m_e are the electron charge and mass. The electron-ion collision frequency

can be written as;

$$\nu_{ei} = \frac{4(2\pi)^{1/2} e^4 Z n_e \ln\Lambda}{3\sqrt{m_e}(k_b \mathrm{T_e})^{3/2}} \quad \approx 2.9 \times 10^{-6} Z n_e \ln\Lambda (\mathrm{T_e(eV)})^{-3/2} \tag{2.6}$$

where $\ln\Lambda$ is the Coulomb logarithm for electron-ion collisions with the usual limits of b_{min} and b_{max} of the electron-ion scattering cross-section where b_{max} is the Debye length λ_D and $b_{min} = Ze^2/k_B T_e$ is the de Broglie wavelength. We write

$$\Lambda = \frac{b_{max}}{b_{min}} = \lambda_D \frac{k_B T_e}{Ze^2} = \frac{9N_D}{Z} \tag{2.7}$$

using $\lambda_D = \left(\frac{\epsilon_0 k_B T_e}{n_e e^2}\right)^{1/2}$ and $N_D = \frac{4\pi}{3}\lambda_D^3 n_e$ where N_D is the number of electron in the Debye sphere. Here T_e and n_e are the electron temperature and number density, Z is the ion charge. The effect of electron-ion collisions when electrons oscillate in the laser electric field is to remove energy from the laser field giving rise to an effective absorption coefficient κ_{ib} which can be written [33, 37] ;

$$\kappa_{ib} = \frac{\nu_{ei}(n_c)}{c} \frac{n_e}{n_c} \left(1 - \frac{n_e}{n_c}\right)^{-\frac{1}{2}} \quad . \tag{2.8}$$

It can be seen that inverse bremsstrahlung absorption increases rapidly near the critical density.

Due to laser light absorption, the laser intensity I decreases while it propagates in a plasma. For laser propagation in the z-direction with inverse bremsstrahlung absorption, we have

$$\frac{dI}{dz} = -\kappa_{ib} I \quad . \tag{2.9}$$

Equation 2.9 can be solved analytically, such that

$$\mathrm{I}(z) = I(0)\exp(-\alpha_{ib}) \tag{2.10}$$

with

$$\alpha_{ib} = \int_0^L \kappa_{\mathrm{ib}}\mathrm{dz} \tag{2.11}$$

for a plasma size of L. Here α_{ib} is known as the absorption coefficient. For a linear density profile with $n_e = n_c(-z/L)$ Kruer(1988) [31] showed that;

$$\alpha_{ib} = \frac{4}{3}\frac{\nu_{ei}(n_c)L}{c} \quad . \tag{2.12}$$

The reflected wave decreases with amplitude of $\exp(-4\nu_{\mathrm{ei}}(\mathrm{n_{cr}})L/3c)$ or energy of $\exp(-8\nu_{\mathrm{ei}}(\mathrm{n_{cr}})L/3c)$ assuming a constant temperature with distance up to the critical surface. Here $\nu_{ei}(n_c)$ is the electron-ion collision frequency at the critical surface. At higher laser intensities ($> 10^{16}\,\mathrm{W\,cm^{-2}}$) with higher electron temperature ($\sim$ 2 keV), as the collision frequency $\nu_{ei} \propto T_e^{-3/2}$, inverse bremsstrahlung becomes less efficient and other absorption processes become relatively more important [38].

Even if this section is not directly relevant with the work presented in this thesis, it is important to know the laser absorption mechanisms for lower laser intensities to explain collisionless absorption mechanisms.

2.2.3 Resonance Absorption

Near the critical surface, the electric field of an incoming laser field becomes large (see eg. figure 2.2). In the WKB approximation, an incident electric field **E** swells

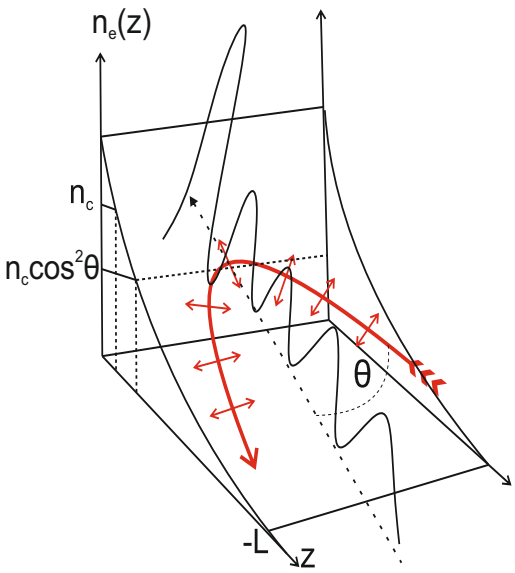

Figure 2.3: Schematic picture of p-polarized laser ray path for resonance absorption. The inset shows a schematic of the electric field amplitude.

to $\mathbf{E}/n$ where n is the refractive index. The oscillating electric field accelerates electrons and generates electrostatic waves. These electrostatic waves can transfer their energy into thermal energy and heat the plasma.

Resonance absorption (see figure 2.3) occurs when a laser is obliquely incident at angle of incidence θ into a density profile with plasma expanding normally to the target surface. The laser light penetrates to a turning point at density $n_c\cos^2\theta$ with an evanescent wave tunnelling to the critical density n_c where the value of the electric field swells. With p-polarized laser light, the electrons are accelerated parallel to the density gradient by the swollen electric field and so can gain a net velocity. For a linear density gradient ($n_e = n_c z/L$) the absorbed power due to resonance absorption is given by [31, 35, 39];

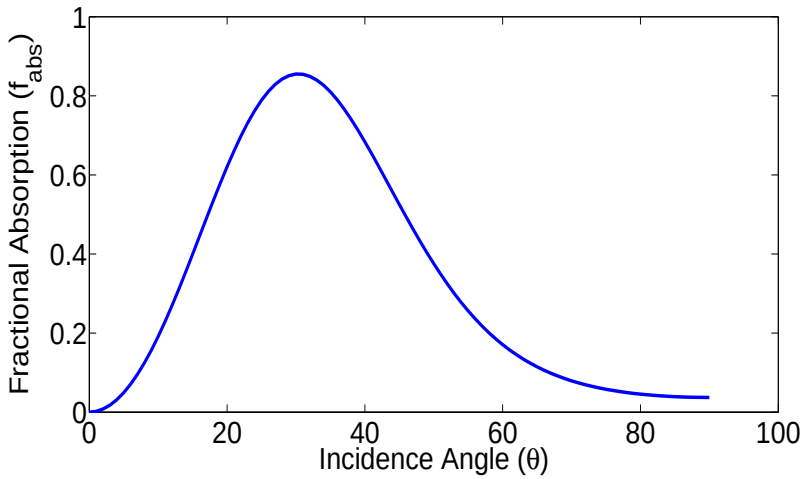

Figure 2.4: Fractional laser absorption in different angles for the 0.5 μm scale length and 0.8 μm laser wavelength.

$$P_{abs} \simeq \frac{\pi}{2}\epsilon_0 c L^2 E_d^2 \tag{2.13}$$

where E_d is the component of the laser electric field which oscillates the electrons through the density gradient and is given by;

$$E_d = \frac{E_0}{\sqrt{2\pi\omega L/c}}\alpha(\eta) \tag{2.14}$$

where ϵ_0 is the permittivity of free space, E_0 is the amplitute of the laser electric field in a free space, $\alpha(\eta) \simeq 2.3\,\eta \exp(-2\eta^3/3)$ and $\eta \simeq (\omega L/c)^{1/3}\sin\theta$. Another way of writing eq.2.13 is

$$P_{abs} = \frac{\epsilon_0 L c^2 f_{abs} c E_0^2}{2\omega} \tag{2.15}$$

where f_{abs} is the fractional absorption of the incident light wave with $f_{abs} \simeq \alpha(\eta)^2/2$. The angle of laser incidence for peak resonance absorption is given by ;

$$\theta_{max} \simeq \sin^{-1}\left[0.8\left(\frac{c}{\omega L}\right)^{1/3}\right] \tag{2.16}$$

for a linear density gradient. Figure 2.4 shows the fractional absorption f_{abs} as a function of laser incidence angle θ for 0.8 μm laser wave and $L = 0.5$ μm scale length.

Resonance absorption has been observed in the work presented in this thesis in chapter 6 for the ultrashort laser light solid interactions and used to determine the scale length generated by a pre-pulse.

2.2.4 Brunel Type Absorption

Resonance absorption stops working in its regular form in high electron density gradients. Here the amplitude of the resonantly driven plasma wave at the critical density is approximately the same as the incident laser field E_0. Electrons are oscillated along the density gradient with an amplitude $x_p \simeq eE_0\sin\theta/m_e\omega^2 = v_{os}\sin\theta/\omega$. When the spatial extent of electron oscillation goes beyond the density scale length L, expressions for resonance absorption are no longer valid.

For electrons in a steep density gradient, the laser electric field can push electrons out into the vacuum beyond the thermal Debye sheath length λ_D. When the field reverses direction, these electrons will move with the laser field and are accelerated back into the plasma. The electric field cannot propagate into the overdense region (penetrating only to a skin depth $\sim c/\omega_{pe}$), so as the electrons move into overdense plasma their electron energy is absorbed due to collisions.

This mechanism was first proposed by Brunel [40]. A capacitor approximation was developed where the $\mathbf{v} \times \mathbf{B}$ term on the electrons is neglected and it is as-

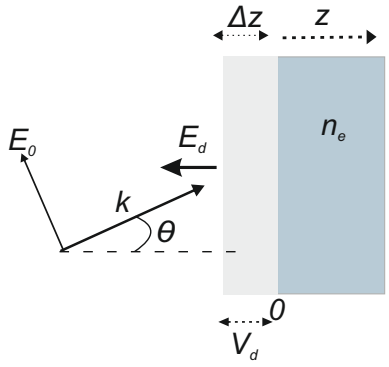

Figure 2.5: Capacitor model of Brunel heating mechanism

sumed E_0 has some component E_d normal to the target surface which accelerates electrons back and forward across their equilibrium position (see figure 2.5).

If the laser wave is at incident angle θ, the driving electric field will be with the factor 2 arising if we assume total reflection at the critical density.

$$E_d = 2E_0 \sin\theta \quad . \tag{2.17}$$

If this electric field accelerates an electron cloud to a distance Δz from its initial position, the number density of electrons on the surface of this layer is $\rho = n_e \Delta z$ so the electric field ΔE generated between $z = \Delta z$ and $z = 0$ is given by ;

$$\Delta E = e\rho/\epsilon_0 \quad . \tag{2.18}$$

When the charged electron cloud returns to its initial position, it will have gained a velocity $v_d \simeq 2v_{os}\sin\theta$ where $v_{os} = \frac{eE_0}{m_e\omega}$. If it is assumed that all the electrons energy is lost in the solid target, the average energy density absorbed

per laser cycle is given by;

$$P_a \simeq \frac{\epsilon_0}{4\pi}\frac{e}{m_e\omega}E_d^3 \tag{2.19}$$

when the incoming laser power is $P_L = \epsilon_0\, c\, E_0^2 \cos\theta/2$, we acquire the fractional absorption rate:

$$\eta_a \equiv \frac{P_a}{P_L} = \frac{4}{\pi}a_0\frac{\sin^3\theta}{\cos\theta} \tag{2.20}$$

where $a_0 = v_{os}/c$. According to equation 2.20, larger incidence angles and higher irradiance causes higher absorption.

There are two corrections for the above treatment. Taking account of less than 100% reflection at the critical density reduce E_d (equation 2.21), so that.

$$E_d = [1 + (1 - \eta_a)^{1/2}]\, E_0 \sin\theta \quad . \tag{2.21}$$

In addition when the absorption fraction η_a is greater than 30% assuming 45° incident angle and $L/\lambda = 0.1$, the return electrons can have relativistic velocities at intensities higher than 10^{18} W cm^{-2} so their kinetic energy E_k becomes relativistic with $E_k = (\gamma - 1)m_e c^2$. A more complex expression for the fraction of incident laser power absorbed due to Brunel absorption is thus given by ;

$$\eta_B = \frac{1}{\pi a_0} f\left[(1 + f^2\, a_0^2 \sin^2\alpha)^{1/2} - 1\right]\frac{\sin\theta}{\cos\theta} \tag{2.22}$$

where $f = 1 + (1 - \eta_a)^{1/2}$ is the laser electric field amplification factor. The dependence on angle and scale length have been theoretically [15, 41] and experimentally [42, 43] investigated.

2.3 Fast Electron Generation

The generation and transport of laser produced electrons in plasma is an important topic in high power laser interactions. In this section the generation of fast electrons and hot electron sources are discussed. Electrons with energy > 0.511 MeV are strongly affected by relativistic mass increases.

2.3.1 Laser Energy Absorption for Fast Electrons

In our discussion in section 2.2, we have implicitly assumed that accelerated electrons lose energy in collisions with the bulk of electrons which are in a thermal distrubution. However, with laser absorption mechanisms apart from inverse bremsstrahlung, accelerated electrons can have little interaction with slow moving thermal electrons as the cross-section for a collision drops approximately as $1/\mathbf{p}^2$, where $\mathbf{p}$ is the electron momentum. Accelerated electrons are more likely to thermalise with other electrons of comparable velocity, producing a hot electron component of much higher temperature than the typical temperature (~ 500 eV) of the bulk of the electrons [39, 44, 45].

Considering a solid target irradiated by a plane polarised intense laser pulse as in figure 2.6, ionisation of the target surface generates a plasma extending out into the vacuum with an exponential density profile for a one dimensional isothermal expansion ($n_e = n_s \exp(-z/L)$) [31, 33]. The laser pulse can penetrate up to the critical density (n_c) at which the plasma oscillation frequency is equal to the laser drive frequency. The acceleration of an electron in the electric $\mathbf{E}$ and magnetic $\mathbf{B}$ of a laser is given by the Lorentz equation. The force on an electron can be

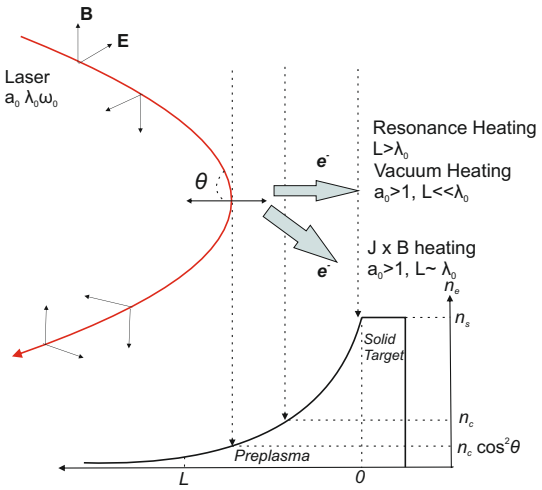

Figure 2.6: Schematic illustrating of resonance heating and the $\mathbf{J} \times \mathbf{B}$ acceleration mechanisms in the propagation of a linear polarised laser pulse onto a solid target with a preformed plasma density gradient.

written

$$\mathbf{F_L} = \frac{d\mathbf{p}}{dt} = m_e \frac{d(\mathbf{v}\gamma)}{dt} = -e(\mathbf{E} + \mathbf{v} \times \mathbf{B}) \tag{2.23}$$

where $\mathbf{p}$ and $\mathbf{v}$ are the electron momentum and velocity, respectively. The electric field of the laser oscillates the electrons in the electron field direction transverse to the laser direction with velocity;

$$v_\perp = \frac{eE_0}{m_e \omega_0} \tag{2.24}$$

where E_0 is the amplitude of the laser electric field and ω_0 is the laser frequency. At high laser intensities, the force which accelerates electrons in the laser propagation direction due to the $e(\mathbf{v} \times \mathbf{B})$ force component becomes comparable to the electric field force and is referred to as the $\mathbf{J} \times \mathbf{B}$ force.

For a linearly polarised electromagnetic wave travelling along the z - axis, the

z component of this force at non relativistic velocities becomes [34];

$$F_{p_z} = \frac{-m_e}{4}\frac{d}{dx}v_\perp^2(1-\cos(2\omega_0 t)) \quad \cdot \tag{2.25}$$

The $\mathbf{J}\times\mathbf{B}$ force accelerates electrons in the laser propagation direction with frequency $2\omega_0$. This acceleration mechanism is clearly different to resonance absorption in which the electrons are accelerated in the direction of the target normal by the laser electric field with an amplitude varying with the laser frequency ω_0.

2.3.2 Characteristics of the Fast Electrons

The random electron acceleration in the laser field results in fluctuations in their trajectories and their gained energies. The averaging of these single particle distributions over time results in a Maxwellian distrubution, with a characteristic hot electron temperature $k_B T_h$. A single temperature Maxwellian distrubution can be defined as a function of hot electron energy, E_h, as;

$$f(E_h) = N_0\sqrt{\frac{4E_h}{\pi(k_B T_h)^3}}\exp(-\frac{E_h}{k_B T_h}) \tag{2.26}$$

where N_0 is the total number of hot electrons. The electron energy spectrum is given by the Maxwell - Juttner distrubution at laser intensities for which $k_B T_h$ approaches $m_e c^2$ [46].

$$f(\gamma) = N_0\frac{\gamma^2\beta}{\theta\, K_2(1/\theta)}\exp\left(\frac{-\gamma}{\theta}\right) \tag{2.27}$$

where $\beta = v/c$, $\gamma = \frac{1}{\sqrt{1-\beta^2}}$, K_2 is a second order Bessel function and $\theta = \frac{k_B T_h}{m_e c^2}$. To describe the full energy distribution of electrons, the superposition of two

Table 2.1: Short pulse hot electron temperature scaling (right hand column), the irradiances regimes of validity ($I_0\lambda_0^2$ and L/λ_0 columns), and the angle θ of maximum absorption. The *Type* column indicates whether the result is from theory, simulation or experimental (data from cited references).

Scaling	*Type*	$I_0\lambda_0^2$	L/λ_0	θ	k_BT_h(keV)
Resonance [47]	Sim.	$< 10^{17}$	> 1	$\sin^{-1}\left(\frac{c}{2\omega_0 L}\right)^{1/3}$	$14(k_BT_eI_{16}\lambda_{\mu m}^2)^{1/3}$
Brunel [48]	The.	$> 10^{17}$	< 1	$73°$	$3.7(I_{16}\lambda_{\mu m}^2)$
Gibbon [41]	Sim.	$< 10^{17}$	≤ 0.1	$45°$	$7(I_{16}\lambda_{\mu m}^2)^{1/3}$
Beg [45]	Exp.	$< 10^{19}$	> 1	$30°$	$215(I_{18}\lambda_{\mu m}^2)^{1/3}$
Haines [44]	The.	$> 10^{18}$	$-$	$-$	$511[(1+(I_{18}\lambda_{\mu m}^2)^{1/2})^{1/2}-1]$
Wilks [36]	Sim.	$> 10^{18}$	~ 1	$0°$	$511[(1+0.73I_{18}\lambda_{\mu m}^2)^{1/2}-1]$

Maxwellian distributions with two different temperatures is employed with cold electron temperature T_c and hot electron temperature T_h.

The hot electron temperature, k_BT_h, is a measure of the average energy of the initial hot electron population and has dependence on laser irradiance There are various power law scalings reported in the literature, depending on the absorption regime accessed. In the relativistic regime the $\mathbf{J}\times\mathbf{B}$ scaling can be applied [36]. For a linearly polarised laser field , the hot electron temperature is given by;

$$k_BT_h = m_ec^2(\sqrt{1+a_0^2/2}-1) \tag{2.28}$$

where a_0 is the normalised laser amplitude defined as;

$$a_0 = \sqrt{\frac{I_0\,(\mathrm{W\,cm^{-2}})\,\lambda_0^2\,(\mu\mathrm{m}^2)}{1.37\times10^{18}}} \quad . \tag{2.29}$$

Table 2.1 summarizes the hot electron temperature produced according to different authors under different assumed plasma conditions.

In Inertial Confinement Fusion (ICF) relativistic electrons have been proposed as an igniter of the fusion fuel [5, 44]. Hot electron generation in laser-plasmas, which is discussed in chapter 5 and 6, is also important in applications where a source of fast electrons is required [49] and because of their role in accelerating ions for applications [21, 50–54].

2.3.3 Laser Wakefield Acceleration (LWFA)

Electrons can be accelerated by laser wakefield acceleration (LWFA) in a sub-critical density plasmas [55–57]. In the standard LWFA acceleration approach, a single short laser pulse excites an electron plasma wave via the ponderomotive force which pushes electrons away from high intensity regions while the ions remain in-situ. A space charge field is set up which pulls electrons back to their initial position. As a laser pulse propagates through underdense plasma a plasma wave travelling in the direction of the laser pulse in set-up with a group velocity $v_g/c \simeq (1 - \omega_{pe}^2/\omega_0^2)^{1/2} \backsimeq 1$, where ω_0 is the laser frequency, is excited and oscillates at the plasma frequency $\omega_{pe} = \sqrt{\frac{n_e e^2}{m_e \epsilon_0}}$ where e, m_e and n_e denote charge, mass and density of electrons, respectively. Charged particles can be accelerated in these plasma waves due to their large longitudinal electric fields which interact with particles travelling close to the speed of light. Electrons, which are trapped by the electric field of the plasma wave, can be accelerated to relativistic energies.

2.3.3.1 Betatron Resonance in Channels

Betatron resonance electron acceleration is a laser acceleration method first discussed by Pukhov et al.[58]. Electrons in the wake of a propagating laser pulse through sub-critical plasma make transverse oscillations due to the laser electric

field. The relativistic electrons oscillates transversely at the betatron frequency $\omega_\beta \approx \omega_{pe}/(2\gamma)^{1/2}$ in these fields while moving along the channel together with the light due to a wakefield where γ is the relativistic factor and ω_{pe} is the plasma frequency. When the betatron frequency coincides with the laser frequency, a resonance occurs causing a large energy exchange between the laser and electrons. The electron acquire a large transverse velocity $\mathbf{v}$ and a large amount of longitudinal electron acceleration due to the $\mathbf{v} \times \mathbf{B}$ force, where $\mathbf{B}$ is the laser magnetic field. It is effectively an inverse free electron laser mechanism [59–61], where the wiggler field is replaced by the self generated quasi-static electric and magnetic fields. Figure 2.7 shows the betatron resonance electron acceleration schematically where the radial electric field produced by the partial electron depletion in the channel due to the electrons which are pushed out by the light pressure and a further azimuthal magnetic field due to the electron current flowing in the channel which serves to focus electrons. These both fields work together to confine the relativistic electron beam in the channel [62–65].

This subject has been discussed due to the relevance of the work presented in chapter 3

2.4 Fast Electron Penetration in Solids

Recent developments in laser technology have supplied intensities greater than 10^{18} W cm^{-2} with shorter laser pulses (< 1 ps) focussed to < 10 μm spots. These developments have made it possible to generate energetic electrons. These fast electrons can transport absorbed energy further into the target where the laser cannot propagate. The transport of fast electrons generated by ultra intense laser

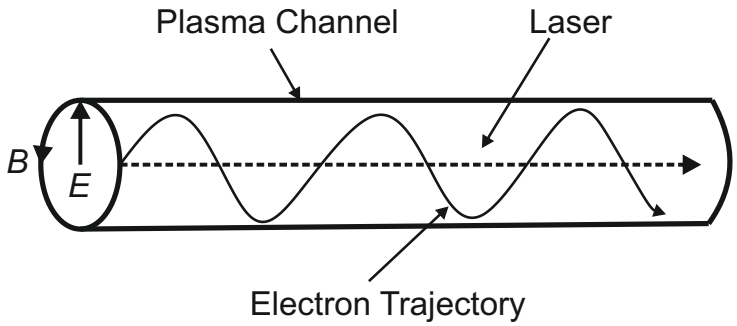

Figure 2.7: Direct laser acceleration in a self-focussing plasma channel. The produced electric and magnetic field cause the electron oscillation in transverse direction while the laser light propagates longitudinal direction. (Image modified from reference [57].)

pulses ($I > 10^{18}$ W cm^{-2}) in an overdense plasma has been investigated by many experimental [17, 66–68] and theoretical research groups [69–71]

The transport of fast electron beam is affected by collisions with the electrons within the target. The electrons lose their energy via excitation, ionisation and radiation emission. The stopping power which is a function of the incident electron energy and the characteristics of material quantifies the loss of electron energy.

The work presented in this thesis will mainly discuss the hot electron generation in chapter 5 and 6. The fast electron penetration and absorption in solids is also interest of our research due to the relevance of fast ignition and target heating.

2.4.1 Stopping Power of Electrons

High energy electrons passing through material lose some of their energy due to various mechanisms such as scattering, Coulomb collisions, ionization and bremsstrahlung radiation. These mechanisms effect the electron direction caus-

ing fluctuating electron paths. The range or linear penetration distance into the material will be very different from the electron path. Stopping power is defined as the loss of energy per unit path length. The expressions for the energy loss per unit path length for electrons (which are known as the Bethe formula) are given by [72] for respectively collisions;

$$\left(\frac{dE}{dx}\right)_c = \left(\frac{e^2}{4\pi\epsilon_0}\right)^2 \frac{2\pi N_0 Z\rho}{m_e c^2 \beta^2 A}\left[\ln\frac{E_0(E_0+m_e c^2)^2\beta^2}{2I^2 m_e c^2} + (1-\beta^2) - \right.$$
$$\left. \ln 2(2\sqrt{1-\beta^2} - 1 + \beta^2) + 0.125(1-\sqrt{1-\beta^2})^2\right],$$

and radiation;

$$\left(\frac{dE}{dx}\right)_r = \left(\frac{e^2}{4\pi\epsilon_0}\right)^2 \frac{Z^2 N_0 (E_0 + m_e c^2)\rho}{137 m_e^2 c^4 A}\left[4\ln\frac{2(E_0+m_e c^2)}{m_e c^2} - \frac{4}{3}\right], \tag{2.30}$$

where $\beta = v/c$, e is the electric charge, Z, A and ρ are the atomic number, atomic weight and density of the stopping material, N_0 is Avogadro's number and m_e is the mass of electron. The parameter E_0 is the kinetic energy of the electron and I is the mean excitation energy of the atomic electrons. In practise, $I \simeq 10Z$ eV, it is 166 eV for aluminium.

The amount of lost energy by an electron while it travels through matter depends on the incident energy of the electron and the type of the material. For low energy electrons ($<$ 1 MeV), the collisional stopping power dominates, but for high energy electrons ($>$ 1 MeV), the total stopping power is dominated by radiative process.

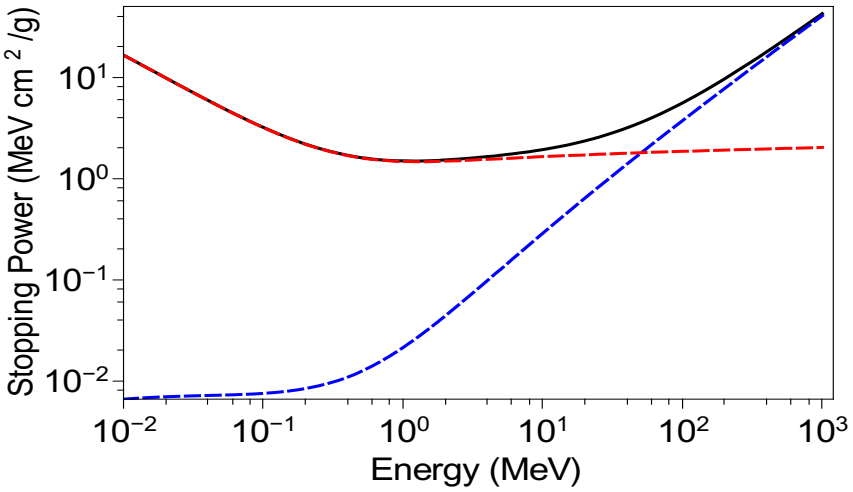

Figure 2.8: Stopping power of electrons for aluminium (Al). Blue dashed line represents radiative effect, red dashed line represents collisional effects and black solid line represents total energy loss of electrons for aluminium (Al) matter.

The total energy loss is calculated by adding collisional and radiation processes together such that

$$\left(\frac{dE}{dx}\right)_{total} = \left(\frac{dE}{dx}\right)_{c} + \left(\frac{dE}{dx}\right)_{r} \quad . \tag{2.31}$$

The range of electrons can be calculated by integrating equation 2.31 over the energies of electrons such that

$$R = \int_{E_0}^{0} \left(-\frac{dE}{dx}\right)^{-1}_{total} dE \quad . \tag{2.32}$$

Integration of the total energy loss over electron energy gives that the range of electrons is ~ 3.9 cm for 20 MeV energy electrons in an aluminium target with a density $\rho = 2.7\ \mathrm{g\,cm^{-3}}$.

Figure 2.8 shows stopping power of plasma as a function of electron energy. This data is available using the ESTAR database provided by the National Institute for Standards in Technology (NIST) [73].

2.4.2 Return Currents

The penetration depth of an electron beam is normally deduced by collisions and radiation inside the target. However, the calculations which have been done by A.R.Bell et al [74] shows that when the Bethe-Bloch formula is applied for electron produced in laser - plasmas, the absorbed laser energy is much higher than the laser energy itself. The discrepancy is resolved by the appearance of generated return currents to keep charge neutrality. Hot plasma behaves like a superconductor with zero resistivity so $j_h + j_c \simeq 0$ can be easily satisfied. However, in the case of cold-solid density plasma, the resistivity will be finite so $j_c << j_h$ which will rapidly induce an electric field which prevents hot electron penetration into the target to a value much less than the mean free path for energy loss. This penetration depends on the conductivity of the target.

The fast electron current j_h generates an electrostatic field E which slows down the fast electrons. This electric field creates the return current of the target free electrons (j_c), according to the Ohm's law $j_c = -j_h = \sigma_e E$ where σ_e is the electrical conductivity of the thermal plasma. This implies that not only the number of hot and cold electrons must be balanced but also everywhere within the target the two currents must be nearly in balance.

The penetration depth into the target can be written as

$$x_0 = \left(\frac{T_h}{100(\mathrm{keV})}\right)^2 \left(\frac{\sigma_e}{10^6(\Omega^{-1}\,\mathrm{m}^{-1})}\right)^{-1} \left(\frac{I_{abs}}{10^{18}(\mathrm{W\,cm}^{-2})}\right)^{-1} 3\,\mu\mathrm{m} \qquad (2.33)$$

where x_0 is the effective penetration depth of the fast electrons while the laser is incident. Assuming the parameters for $T_h = 20$ MeV, $I_{abs} = 5 \times 10^{20}$ W cm^{-2}

and conductivity has been measured for temperatures up to 100 eV as $\sigma_e = 10^6$ $\Omega^{-1}\mathrm{m}^{-1}$ [75] for a solid aluminium target which gives a 240 μm penetration depth for the fast electrons. This is a lot shorter distance than predicted by the Bethe - Bloch formula.

2.5 Plasma Emissivity

The emission of radiation from plasmas acts to cool the plasmas and is also a signature of the conditions in the plasma and so can be used to diagnose the plasma parameters. Radiation emission from a hot component of a laser - plasma can also heat cooler plasma regions such as the solid target.

Free-Free emission is the main x-ray emission process represented in chapter 6.

2.5.1 Free-Free Emission

As mentioned in section 2.2.2, inverse bremsstrahlung and bremsstrahlung are inverse process. Bremsstrahlung which is also known as free-free emission occurs when a free electron accelerates in the field of an ion and a photon is emitted.

The Bremsstrahlung emission in units of power per unit volume from plasma in the photons energy range $\hbar\omega$ to $\hbar\omega + d(\hbar\omega)$ is given by [76]

$$P_{ff}(\hbar\omega)d(\hbar\omega) = \frac{32}{3}\sqrt{\frac{\pi}{3}}r_0^2 c\left(\frac{E_H}{T_e}\right)^{1/2}\bar{Z}^2 n_i n_e \exp(-\frac{\hbar\omega}{T_e})d(\hbar\omega) \tag{2.34}$$

where $r_0 = e^2/m_e c^2 = 2.212 \times 10^{-13}$ cm is the electron radius, c is the speed of

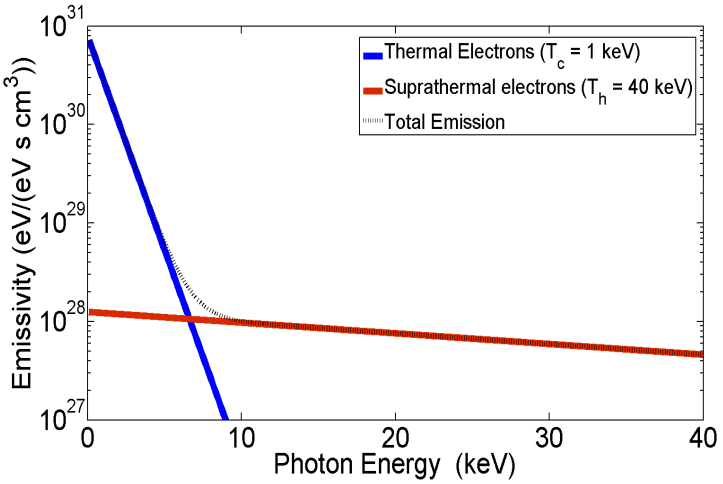

Figure 2.9: Hot and cold temperature component x-ray energy spectrum for a sample of free-free emission for a copper plasma with cold electron density $n_e = 1 \times 10^{22}$ cm^{-3} and hot electron density of 10^{21} cm^{-3}.

light, E_H is the ground state hydrogen atom binding energy (13.605 eV), n_i and n_e is the electron and ion densities and T_e is the plasma temperature. Figure 2.9 shows a sample bremsstrahlung x-ray spectrum for copper. A bi-Maxwellian electron energy distrubution is assumed with an electron density $n_e = 1 \times 10^{22}$ cm^{-3} for the cold electrons. The number density of hot electrons is assumed to be 10^{21} cm^{-3}. Temperatures of 1 keV and 40 keV are assumed.

2.5.2 Free-Bound Emission

Radiative recombination (free-bound emission) occurs when a free electron is captured by an ion and a photon is emitted. This radiation emission featured sharp emission edges related to the binding energies of the various ionisation states. The power emitted due to a recombination radiation for photons with energy greater

than the binding energy, $E_{\zeta-1,m}$, of the ion after recombination is given by [76]

$$P_{fb} = \frac{64}{3}\sqrt{\frac{\pi}{3}}\, c\, r_0^2\, \zeta n_i n_e \left[\left(\frac{E_{\zeta-1,m} - \Delta\chi_{\zeta-1}}{kT_e}\right)\right]^{3/2} \times \left(\frac{1}{n_p^3}\right) \exp\left(\frac{-\hbar\omega}{kT_e}\right) [1 - P_{\zeta,m}] \tag{2.35}$$

where m is the quantum numbers of the state, $m = (n_p, l)$ n_p and l are the principal and orbital quantum numbers of the bound state, $\Delta\chi_{\zeta-1}$ is the continuum lowering and $P_{\zeta,m}$ is the population probability of the final bound state. The last factor of the equation , $(1 - P_{\zeta,m})$, is taken into account for the number of unoccupied states in the recombining ion. The units of P_{fb} is also eV/(eV s cm^3).

2.5.3 Bound-Bound Emission

Spectral line emission (bound-bound) occurs when an electron decays from excited state to lower energetic quantum state of the ion. The emitted photon energy is equal to the energy difference between the levels. The power of line emission can be calculated using [76]

$$P_{bb} = N_{\zeta,m'}\, \hbar\, \omega_{\zeta,m'\to\zeta,m}\, A(\zeta, m' \to \zeta, m)\, L(\hbar\omega) \tag{2.36}$$

where ζ is the ion charge, m and m' are the lower and upper states, $\hbar\omega_{\zeta,m'\to\zeta,m}$ is the transition energy which is equal to the emitted photon energy and N_ζ, m' is the ion density with charge ζ and state m'. $A(\zeta, m' \to \zeta, m)\, L(\hbar\omega)$ is the Einstein A coefficient for the decay from m' to m. $L(\hbar\omega)$ is the normalised line profile factor in units of eV^{-1}.

2.6 Computer Simulation Codes

There are different PIC (particle in cell) codes available for the simulation of laser plasma interactions. The aim of this section to introduce the PIC codes used in the work contained in this thesis.

2.6.1 EPOCH

EPOCH (Extendable PIC Open Collaboration)[77] is a plasma physics simulation which uses the particle in cell (PIC) method [31]. It is based on an older code PSC written by Hartmut Ruhl. It is written in FORTRAN90. In the PIC method, a smaller number of pseudoparticles are used to represent the physical particles. Electric and magnetic fields are generated by the motion of these particles and calculated using a finite difference time domain technique on an underlying grid of fixed spatial resolution. These calculated fields apply forces on the pseudoparticles which are used to update the pseudoparticle velocities. These velocities are used to modify the pseudoparticle positions.

EPOCH is used by many different users and uses the SI unit system. An example of initial density profile for a target which has 10 μm scale length is shown in figure 2.10. The computed electron temperature for a 0.2 ps pulse length and irradiance is 1×10^{20} W cm^{-2} with 7 μm focal spot for a 1.054 μm wavelength laser light is presented in figure 2.11. The laser electric field for this example is shown in figure 2.12.

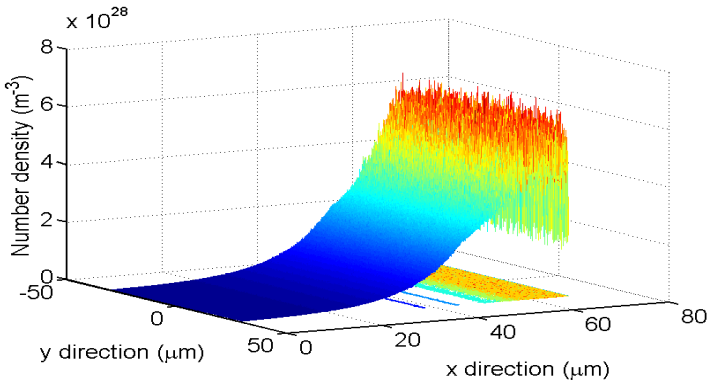

Figure 2.10: A sample of an exponential density profile with a 10 μm scale length as set up for the initial condition in a PIC code simulation.

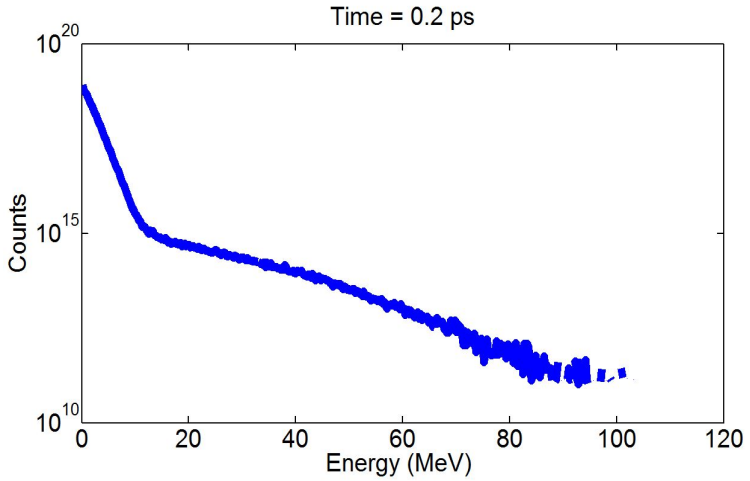

Figure 2.11: A sample of a hot electron energy distribution for 1×10^{20} W cm^{-2} laser irradiance, 0.2 ps pulse length and 1.054 μm wavelength at normal incidence simulated using EPOCH 2D PIC code.

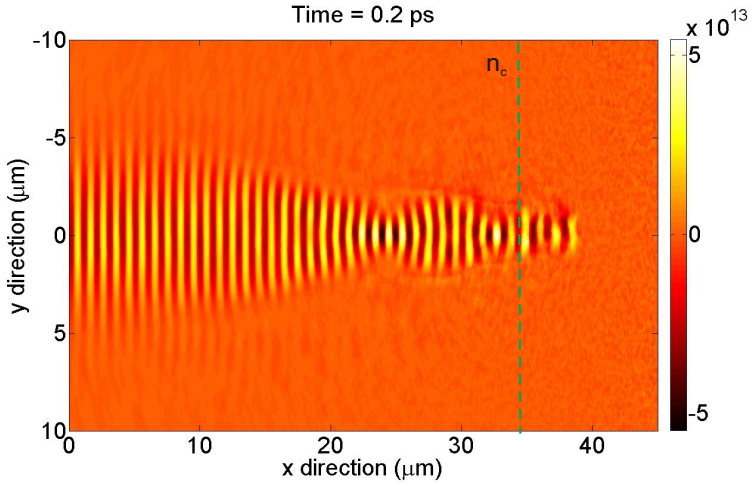

Figure 2.12: Laser electric field behaviour for the 10 μm scale length and time assumed is 0.2 ps after the start of irradiation as far the conditions of figure 2.11.

2.6.2 ELPS

Another PIC code which is used in this research is ELPS (Entry Level PIC Simulations) [78]. 1D Particle -in-cell code which is developed by Dr.Alex Robinson at the CLF. It is designed to study short-pulse laser plasma interactions. The code is a single processor code written in the Fortran language. The algorithms used by the code are the classic PIC algorithms described by Birdsall and Langdon [79].

2.7 Conclusion

This chapter has introduced some theoretical principles behind the work presented in the following chapters. It has defined terminology and explained electromagnetic wave behaviour during propagation within a laser produced plasma. The

next chapter will discuss single electron acceleration.

Chapter 3

Laser Interaction with a Single Electron

3.1 Introduction

This chapter gives a general overview of electron acceleration in an electromagnetic field. The equations of motion of a single electron in a laser electromagnetic field are presented and discussed. The effects on electron acceleration of an ion channel with transverse electric field are investigated. A simple code to model the motion of a single electron in an electromagnetic field is described. The effects of a realistic transverse electric field as would be found with laser channel formation are investigated.

3.2 Single Electron Motion in a Laser Field at High Irradiance

The momentum **p** of an electron in the presence of a light wave with electric **E** and magnetic **B** fields perpendicular to each other is given by the Lorentz equation,

$$\frac{d\mathbf{p}}{dt} = -e(\mathbf{E} + \mathbf{v} \times \mathbf{B}) \quad . \tag{3.1}$$

For electrons accelerated to velocities **v** close to the speed of light, $\mathbf{p} = \gamma m_e \mathbf{v}$ with $\gamma = \frac{1}{\sqrt{1-v^2/c^2}}$ where m_e is the rest mass of the electron. The electric field **E** induces a velocity parallel to **E**, which engenders a velocity in the direction of the beam propagation (the $\mathbf{E} \times \mathbf{B}$ direction) due to the $\mathbf{v} \times \mathbf{B}$ term in equation 3.1. Assuming a polarized plane wave travelling in the positive z - direction with electric field $E(x) = E_\circ \cos(\mathrm{kz} - \omega_\circ t)$ directed in the x-direction, the electron starts to drift in the direction of the beam propagation direction with an average velocity $< v_D >$. It can be shown [15, 31] that;

$$\frac{< v_D >}{c} = \frac{a_\circ^2}{4 + a_\circ^2} \tag{3.2}$$

where $a_\circ$ is the dimensionless laser amplitude which is related to the laser intensity given by equation 2.29.

As **E** for an electromagnetic field oscillates, equation 3.1 indicates that electrons in the presence of electromagnetic wave have an oscillatory motion. The oscillatory motion in the frame of reference of the z drift motion is the famous figure of eight shape motion of electrons in a laser field (see figure 3.1). In the

laboratory frame of reference, the figure of eight motion is not evident (see figure 3.1b).

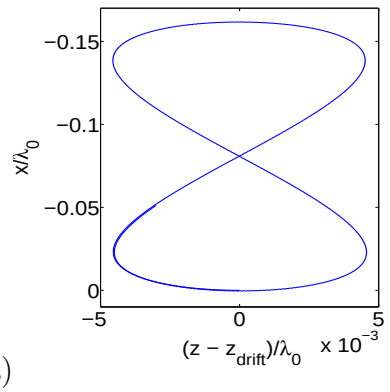

(a)

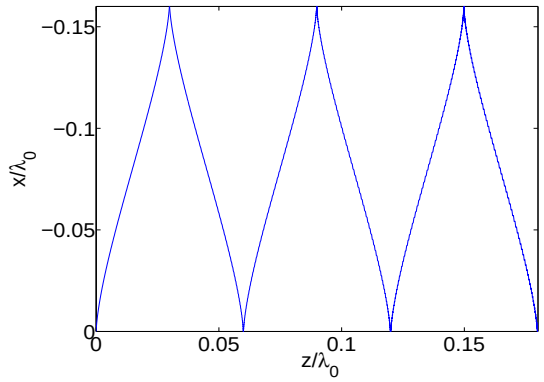

(b)

Figure 3.1: a)Single electron motion which is irradiated by 3×10^{17} W cm^{-2} laser intensity relative to the electron z drift in an electromagnetic wave. b)Electron path in a plane linearly polarized electromagnetic wave relative to the laboratory frame irradiated by 3×10^{17} W cm^{-2} laser intensity (calculated using the code described in section 3.3).

3.3 Code to Model Single Electron Motion

An Excel spreadsheet has been set up to model electron motion in an electromagnetic wave. Sample calculations for an infinitely wide beam (constant electric field amplitude in the x-direction) are given in figure 3.1. The code has been enhanced to model a finite beam size laser with an electric field in the x-direction given by $\mathbf{E} = \mathbf{E}_\circ(\mathbf{x}) \exp(-(\mathbf{x}/\Delta \mathrm{r})^2) \cos(\omega_\circ \mathrm{t})$ where Δr is a measure of the beam radius. Analytic solutions of the z-drift velocity from equation 3.2 and calculated values by the code are shown in figure 3.2 indicating that the model is in agreement with analytic solutions.

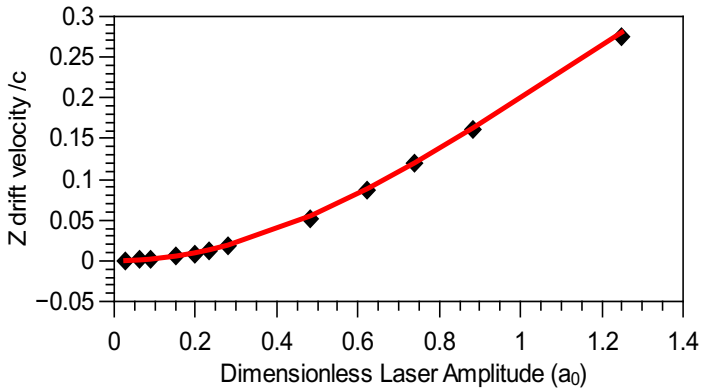

Figure 3.2: Electron drift velocity v_D in the laser propagation direction (z-direction) in units of the speed of light for different laser intensities calculated on a single electron motion code are compared with an analytical solution (equation 3.2). The red line represents the analytical solution and black diamonds are code results.

3.4 The Ponderomotive Force

Associated with electron motion due to the electric field of an electromagnetic wave, an important effect arises when there are gradients of electric field strength. Electrons initially close to the centre of a focussed laser beam are accelerated transversely in the direction of the electric field, but then experience a weaker acceleration back towards the centre when the laser electric field direction changes. There is an effective net force (known as the ponderomotive force) pushing the electrons away from the region of the peak laser intensity [15, 31, 33, 57]. For the non-relativistic case of single electron oscillations near the centre of a focused laser beam, the equation of motion equation 3.1 for the electrons is given by;

$$\frac{\partial v_x}{\partial t} = -\frac{e}{m_e} E_\circ(x) \quad . \tag{3.3}$$

As before, the laser electromagnetic wave is assumed to be propagating along the z-direction with a radial electric field $E_\circ(x)$ variation in the x axis direction. To introduce the ponderomotive force, the equation of motion for the electron fluid are used such that,

$$m_e n_e(\partial \mathbf{v}/\partial t + \mathbf{v}.\nabla \mathbf{v}) = -en_e\mathbf{E} - (en_e)\mathbf{v} \times \mathbf{B} - \nabla p_e \tag{3.4}$$

where e is the electron charge, n_e is the electron number density, $\mathbf{v}$ is the electron velocity, $\mathbf{E}$ and $\mathbf{B}$ is the laser electric and magnetic field, respectively. ∇p_e represents the gradient of the electron thermal pressure.

Assuming the laser electric field is $\mathbf{E} = \mathbf{E}_\circ \mathrm{cos}(\omega_\circ \mathrm{t})$, integration of $\partial \mathbf{B}/\partial t = -\nabla \times \mathbf{E}$ gives the corresponding magnetic field for the laser which is

$$\mathbf{B} = (-1/\omega_\circ)\nabla \times \mathbf{E}_\circ \mathrm{sin}(\omega_\circ t)\cdot \tag{3.5}$$

By writing the electron velocity for its first and second order such that $\mathbf{v} = \mathbf{v}_1 + \mathbf{v}_2$, the first order of the electron velocity can be found as

$$\mathbf{v}_1 = \frac{-e}{m_e \omega_\circ}\mathbf{E}_\circ \mathrm{sin}(\omega_\circ t)\cdot \tag{3.6}$$

The non-linear terms of equation 3.4 can be re-written using the equation 3.6 such that

$$m_e \mathbf{v}_1.\nabla \mathbf{v}_1 = \frac{e^2}{m_e \omega_\circ^2}\mathbf{E}_\circ.\nabla \mathbf{E}_\circ \mathrm{sin}^2(\omega_\circ \mathrm{t}) \tag{3.7}$$

and

$$-e\mathbf{v}_1 \times \mathbf{B}_\circ = \frac{e^2}{m_e\omega_\circ^2}\mathbf{E}_\circ \times (\nabla \times \mathbf{E}_\circ)\sin^2(\omega_\circ \mathrm{t}) \quad \cdot \tag{3.8}$$

By using $\nabla E^2/2 = \mathbf{E}_\circ.\nabla\mathbf{E}_\circ + \mathbf{E}_\circ \times (\nabla \times \mathbf{E}_\circ)$, two terms on the right hand side of equation 3.4 can be combined into the single term $\nabla E^2/2$. Following that, equation 3.4 can be re-written as

$$m_e n_e \partial\mathbf{v}/\partial t \simeq -en_e\mathbf{E} - \frac{n_e e^2}{4m_e\omega_\circ^2}\nabla E_\circ^2(1-\cos(2\omega_\circ t)) \tag{3.9}$$

where the second term of the equation 3.9 on the right hand side is the called ponderomotive force per electron given by

$$\mathbf{F_p} = -\frac{e^2}{4m_e\omega_\circ^2}\nabla E_\circ^2(1-\cos(2\omega_\circ t)) \quad \cdot \tag{3.10}$$

This ponderomotive force pushes the electrons away from higher intensity to lower intensity. Electrons will drift away from the centre of a focused laser beam.

The model of section 3.3 has also been used to calculate the ponderomotive acceleration on a single electron. Figure 3.3 shows the calculated ponderomotive position of an electron from the model and the analytically solved position of an electron as a function of time using equation 3.10 (as explained below). The electron drifts away radially due to the ponderomotive force.

To use the expression (equation 3.10) for the ponderomotive force to deduce electron motion, we need to set up the electron equations of motion. Assuming the electric field is $E_\circ = E_{peak}\exp(-\left(\frac{\mathrm{x}}{\Delta \mathrm{r}}\right)^2)$, where Δr is the focal spot and x is the distance in the x-axis direction (radial direction), the ponderomotive force

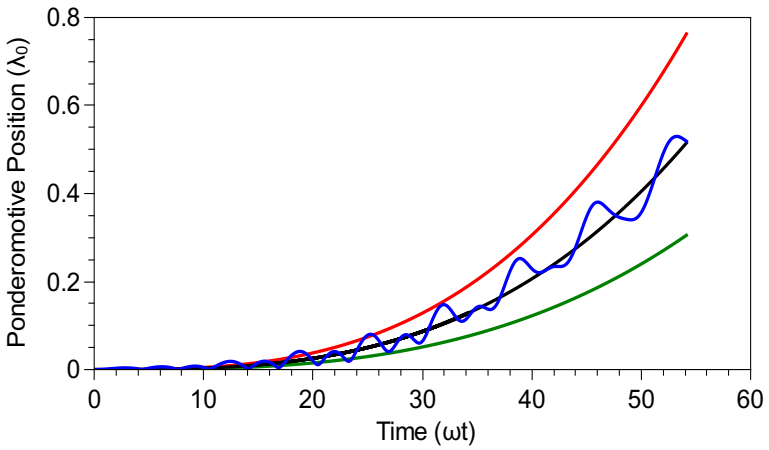

Figure 3.3: Blue line shows the transverse position of a single electron accelerated by a ponderomotive force as a function of time, taken from the model. Black, green and red curves show analytic solutions of the ponderomotive electron position using equation 3.16. Assumed initial velocities are $v_\circ/c = 0.0675$ (black), $v_\circ/c = 0.04$ (green), $v_\circ/c = 0.1$ (red). The applied laser intensity is 5×10^{17} W cm^{-2} within a focal spot of radius 20 $\lambda_\circ$ for the laser wavelength $\lambda_\circ = 1$ μm.

and acceleration can be written as;

$$F_p = \frac{1}{2}\frac{e^2}{m_e\omega^2}\,E_\circ^2\,\frac{x}{\Delta r^2} \tag{3.11}$$

$$a_p = \frac{1}{2}\frac{e^2}{m_e^2\omega^2}E_\circ^2\frac{x}{\Delta r^2} = a_0^2c^2\frac{x}{2\Delta r^2} \quad . \tag{3.12}$$

A ponderomotive acceleration depends on the distance x, a second order linear differential equation is needed to define x. The ponderomotive acceleration is given by an equation of the form ;

$$\frac{\partial^2 x}{\partial t^2} - Ax = 0 \tag{3.13}$$

where $A = a_\circ^2c^2/2\Delta r^2$.

Solutions of this equation take the form $x = B\exp(bt) + C\exp(-bt)$ with the velocity and acceleration given by

$$\frac{\partial x}{\partial t} = B\,b\exp(bt) - C\,b\exp(-bt) \tag{3.14}$$

and

$$\frac{\partial^2 x}{\partial t^2} = B\,b^2\exp(bt) + C\,b^2\exp(-bt) \quad . \tag{3.15}$$

Substituting into equation 3.12 gives

$$(B\,b^2 - A\,B)\exp(bt) + (C\,b^2 - A\,C)\exp(-bt) = 0 \quad . \tag{3.16}$$

If we assume that the initial position of the electron is at $x = 0$ when $t = 0$ we have $B + C = 0$ and $b^2 = A$. If we assume that the electron has an initial velocity $v_\circ$ at $t = 0$, equation 3.14 gives $B - C = v_\circ/b$ so $B = v_\circ/2b$. The x position of the electron can be re-written using these relationships to give

$$x = \frac{v_\circ}{2b}\exp(bt) - \frac{v_\circ}{2b}\exp(-bt) \quad . \tag{3.17}$$

Figure 3.3 shows a comparison of the analytical solution of the ponderomotive force and the code calculations. As the averaged ponderomotive force for a stationary electron at the beam centre ($x = 0$) when there is no gradient of intensity is zero, it is necessary to assume a small transverse initial velocity, which arises due to the plasma temperature. For the analytical solution to agree with the code electron motion requires an initial electron velocity $\simeq 0.07\ c$. We could expect a plasma temperatures between 600- 800 eV [80] for the laser intensity

of $5 \times 10^{17}\,\mathrm{W\,cm^{-2}}$ which ensures that the average electron velocity is close to 0.07 c (see figure 3.4). We have also plotted figure 3.3 for three different initial velocity calculations for $v_\circ/c = 0.1$ (red curve), $v_\circ/c = 0.0675$ (black curve) and $v_\circ/c = 0.04$ (green curve) to emphasize the initial velocity effects on the ponderomotive force analytic solutions.

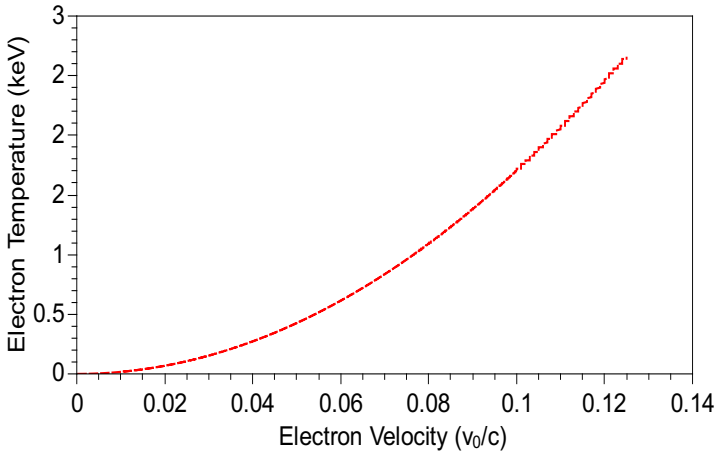

Figure 3.4: Electron temperature as a function of the average electron velocity.

3.5 Electron Acceleration in Channels

It has been proposed that forming a channel in a plasma can result in electron acceleration along the channel [56, 58, 81, 82]. The channel can be formed by the ponderomotive acceleration of electrons (with the plasma ions remaining stationary). Electrons are then accelerated by the electric fields associated with the channel combined with the oscillating electric fields associated with a propagating laser pulse.

An approach for laser driven acceleration of electrons in a plasma channel has

been reported by A.Arefiev [81, 83]. An increase of electron energy occurs when the laser makes an ion channel which confines accelerated electrons. In addition, parametric amplification of the oscillations occurs via the interaction of the laser electric field and transverse channel field and these oscillations enhance the energy gain of electrons in the longitudinal direction. This acceleration is different to betatron oscillation which relies on a short pulse duration (< 100 fs) and the formation of an electric wakefield to accelerate electrons. For betatron oscillations, simulations have been done using laser intensities $\sim 10^{18}$ W cm^{-2} and the laser is required to have linear polarization. Results reported by A.Arefiev show that his parametric electron acceleration mechanism is not sensitive to the polarization of the laser beam and is significant at high irradiance ($\sim 10^{20}$ W cm^{-2}). The parametric channel acceleration process is quasi-steady state and should work for any laser duration (produced the transverse electric field has sufficient time to establish). Electron acceleration in channels has been experimentally observed by different groups [63, 84–86].

3.6 Modelling of Single Electron Motion in an Ion Channel

Our single electron model in an electromagnetic field can be used to investigate electron acceleration in a channel. We introduce an additional transverse electric field and investigate the electron motion in this field upon interaction with the oscillations with the laser electric and magnetic field.

A channel can be formed by the ponderomotive force as a laser propagates

into a plasma. We assume electrons move transversely due to the ponderomotive force with the ions remaining stationary so that an electric field is set up (see figure 3.5). Balancing the ponderomotive force against an electrostatic force gives an electric field in a channel given by

$$E_{ion} = \frac{e}{4m_e\omega_\circ^2}\nabla E^2 \quad . \tag{3.18}$$

Solving the gradient of electric field in terms of cylindrical coordinates gives the solution for a circular geometry associated with a circularly symmetric laser beam (see figure 3.5).

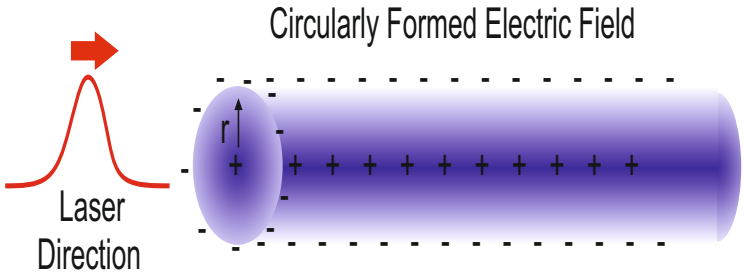

Figure 3.5: Circularly geometry electric field formation in an ion channel.

For an assumed electric field $E = E_\circ \exp(-\left(\frac{\mathrm{r}}{\Delta \mathrm{r}}\right)^2)$ using cylindrical coordinates gives that

$$E^2 = E_\circ^2 \exp(-2\left(\frac{r}{\Delta r}\right)^2) \quad . \tag{3.19}$$

Applying equation 3.19 to equation 3.18 indicates that

$$\frac{E_{ion}}{E_\circ} = \frac{eE_\circ}{m_e\omega_\circ^2}\left(\frac{r}{\Delta r^2}\right)\exp\left(-2\left(\frac{r}{\Delta r}\right)^2\right) \quad . \tag{3.20}$$

Re-writing equation 3.20 in terms the dimensionless laser amplitude a_0 we have

$$\frac{E_{ion}}{E_\circ} = a_\circ \frac{c}{\omega}\left(\frac{r}{\Delta r^2}\right)\exp\left(-2\left(\frac{r}{\Delta r}\right)^2\right) \quad . \tag{3.21}$$

Charge separation which creates the electric field inside the channel can be determined by using Gauss law such that ,

$$\nabla.\mathbf{E_{ion}} = \frac{\rho(r)}{\varepsilon_0} \tag{3.22}$$

where $\mathbf{E_{ion}}$ is the electric field generated inside the channel and $\rho(r)$ is the electron charge density as a function of r.

Solving equation 3.22 using equation 3.21 gives the charge density of the channel ($\rho_\circ$) as a function of radial distance such that (see figure 3.6)

$$\frac{\rho_\circ}{\varepsilon_\circ E_\circ} = a_\circ \frac{\lambda}{\pi\Delta r^2}\exp(\frac{-2r^2}{\Delta r^2})(1-\frac{2r^2}{\Delta r^2}) \tag{3.23}$$

where $\rho_\circ$ is the charge density, $E_\circ$ is the laser electric field peak amplitude, λ is the laser wavelength, $a_\circ$ is the dimensionless laser amplitude, Δr is the laser focal spot radius and r is the radial distance from centre to the edge of the channel. Figure 3.6 shows the charge density for four different laser focal spot radii with the same laser irradiance. It shows that the peak charge created by electron motion has a strong dependence on the laser focal spot. Typical electron number densities inside the channel can be calculated by using the maximum charge density given by figure 3.6. For instance, knowing $\rho_\circ/\varepsilon_\circ E_\circ = 0.8$ for a 0.5 μm focal spot radius,the density Δn_e of electrons removed from the channel centre for this focal spot can be calculated by using $\Delta n_e = \rho_\circ/e$ where e is the electron charge. So

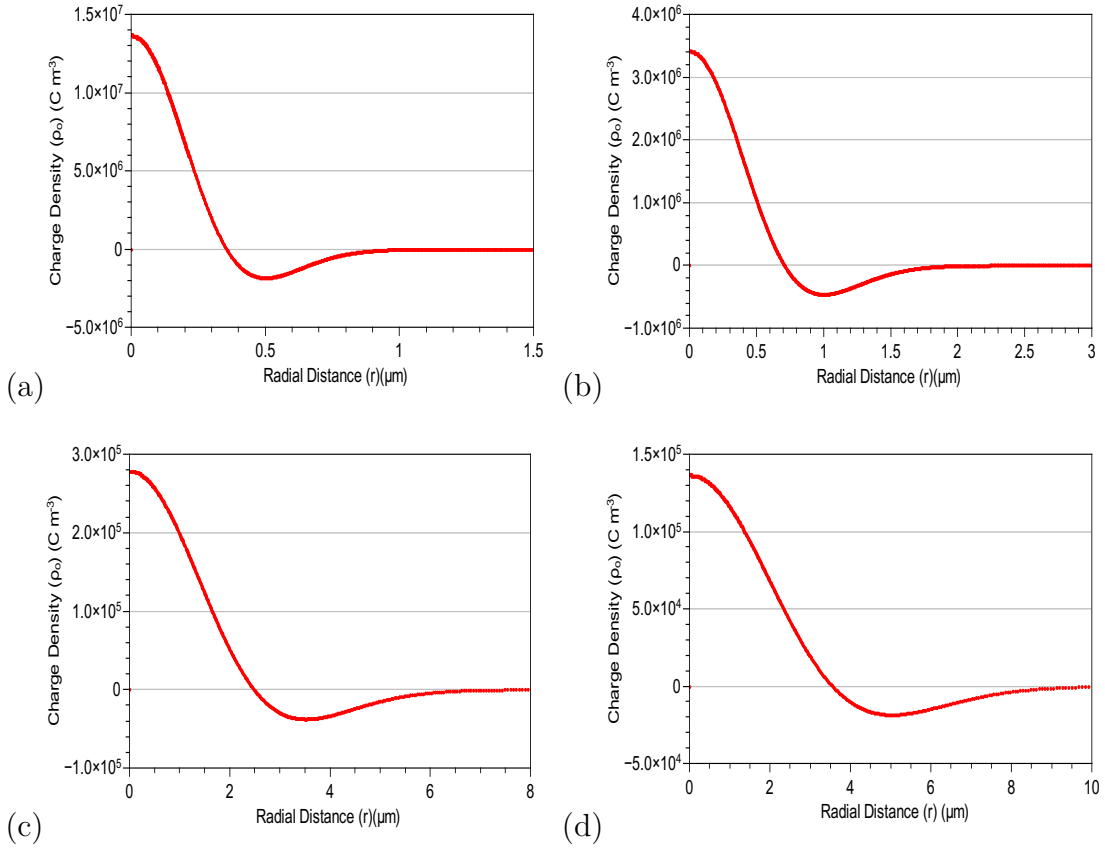

Figure 3.6: Charge density inside a channel formed by the ponderomotive force as a function of radial distance with the laser intensity of $5 \times 10^{17}\,\mathrm{W\,cm^{-2}}$ and the focal spot radius a)$\Delta r = 0.5$ μm , b) $\Delta r = 1$ μm, c) $\Delta r = 3.5$ μm and d) $\Delta r = 5$ μm. The laser wavelength assumed is 1 μm.

the electron number density deficit Δn_e inside the channel which is formed by the ponderomotive force is $\Delta n_e = 8.6 \times 10^{19}\,\mathrm{cm}^{-3}$. Our calculations assume that the total number of electron per unit volume is greater than this value.

It is seen that the electric field generated by the ion channel is significantly larger in a small focal spot and suggests that a large laser focal spot will not affect the electron acceleration.

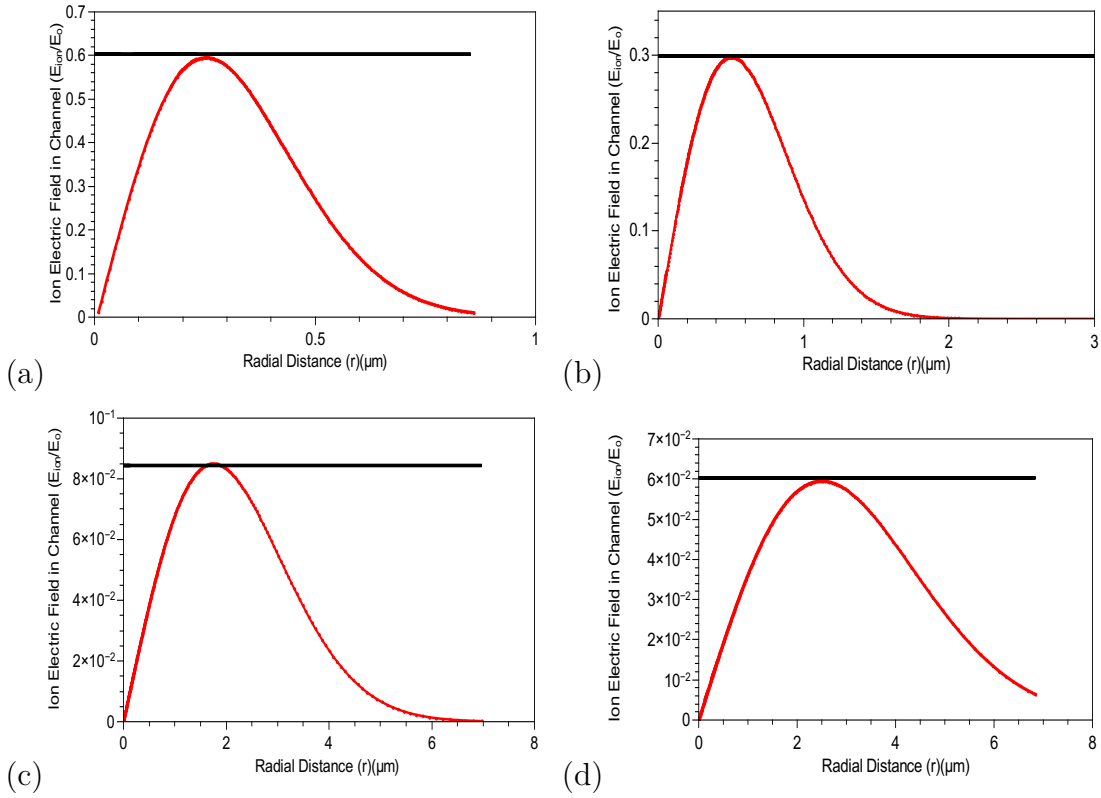

Figure 3.7: The electric field generated inside a channel created by ponderomotive acceleration of electrons (red curve) as a function of channel radial distance from the channel centre. The laser irradiance is constant at $5\times\ 10^{17}$ W cm^{-2} and the laser wavelength is 1 μm. The focal spot radius is a) 0.5 μm, b) 1 μm, c) 3.5 μm and d) 5 μm. An assumed constant electric field is shown as a black line corresponding to ion number densities in the Arefiev model of a) $1.25 \times 10^{20}\,\mathrm{cm}^{-3}$, b) $3.1 \times 10^{19}\,\mathrm{cm}^{-3}$, c) $2.6 \times 10^{18}\,\mathrm{cm}^{-3}$ and d) $1.3 \times 10^{18}\,\mathrm{cm}^{-3}$. The electric field is plotted relative to the on-axis amplitude of the laser electric field.

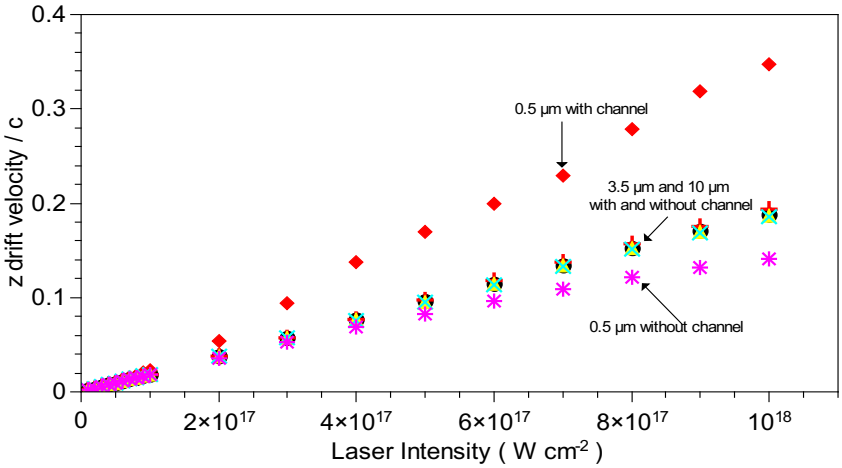

Figure 3.8: Electron drift velocity in the z laser propagation direction in units of the speed of light for different laser focal spots with and without channel formation for different laser intensities. Channel effects are represented by black circles(●) for $\Delta r = 10$ μm, red pluses (+) for $\Delta r = 3.5$ μm and red diamonds(◆) for $\Delta r = 0.5$ μm focal spot radius. No channel effects are shown by yellow triangles (▲) for $\Delta r = 10$ μm, cyan crosses (×) for $\Delta r = 3.5$ μm and magenta stars (✳) for $\Delta r = 0.5$ μm focal spot radius.

Figure 3.7 shows values of the electric field for a laser intensity of 5×10^{17} W cm^{-2} with different focal spots. A uniform electric field is superimposed which is comparable to the peak ponderomotive electric field at different ion number densities following the model of Arefiev. Figure 3.8 shows electron velocities in the laser propagation direction with and without the channel electric field formation due to the ponderomotive force. Decreasing the focal spot size increases the electric field of the channel so the drift velocity at 0.5 μm focal spot is higher than the velocities with 3.5 and 10 μm focal spots. For larger focal spots, the generated ion electric field becomes negligible so the drift velocity of electrons are very similar to the drift velocities without channel formation.

It is clear that at intermediate laser intensities (up to 10^{18} W cm^{-2}), a narrow channel formed by a laser focussed close to the diffraction limit ($\Delta r \simeq 0.5$ - 1 μm)

is required for the channel to significantly affect longitudinal electron acceleration.

The work reported by A.Arefiev has shown that electrons have parametrically unstable oscillations in an underdense plasma with a constant electric field ion channel. In the Arefiev work, all the electrons in a plasma of fixed ion density are assumed to be removed. The assumed uniform channel electric field in the x direction is given by

$$E_{ion}(x) = \frac{n_0 e}{\varepsilon_0}\Delta r \tag{3.24}$$

where n_0 is the ion density and Δr is the focal spot radius [83] . Applying a uniform electric field as given by equation 3.24 with moderate laser intensities, we can compare the effect to a more realistic electron drift velocity with the ponderomotive ion channel electric field discussed above (equation 3.21). To compare the electron drift velocities for the ponderomotive generated electric field and uniform electric field for the same focal spots, we assume comparable electric fields (see figure 3.7). Different ion densities are necessary for the uniform electric field treatment as shown on figure 3.7.

Figure 3.9 shows a comparison of electron velocities in the beam direction for a uniform electric field channel and our calculated circular electric field geometry formed by the ponderomotive acceleration of electrons. Both channel formations give similar velocities for the electrons at higher focal spots as the channel only has a small effect on the electron acceleration. With a tight focus ($\Delta r = 0.5\,\mu$m), there is a significant boost in the electron velocities due to the channel and the more realistic ponderomotive electric field channel has a more significant acceleration effect. Our results indicate that the ponderomotive acceleration of electrons proposed by Arefiev may be viable at irradiances $\sim 10^{18}\,\mathrm{W\,cm^{-2}}$ and can work

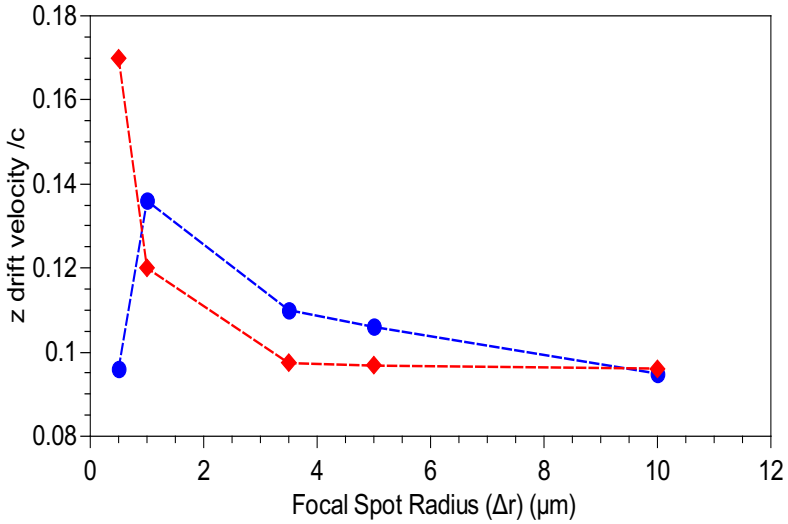

Figure 3.9: Comparison of uniform and pondermotive force shaped electric field on electron drift velocity in the z laser propagation direction in units of the speed of light as a function of focal spot radius. Uniform electric field effects are represented by blue circles (●) and ponderomotive channel formation results are represented by red diamonds (◆). The peak laser intensity is constant at $5 \times 10^{17}\,\mathrm{W\,cm^{-2}}$ and the laser wavelength is 1 μm.

with realistic channel that can be formed by the ponderomotive force.

3.7 Conclusion

Electron motion in an electromagnetic wave has been introduced and a simple model of a single electron motion has been presented. This modelling has been studied to examine electron acceleration which is discussed in chapter 5 since a modifying ion channel with a transverse electric field is possible with tightly focussed laser beams. We have investigated the channel effects on electron acceleration and compared our modelling to a recent electron acceleration model introduced by Arefiev. Channel formation can result in greater acceleration of

electrons enhancing the axial drift velocity by up to a factor of 3 in the laser direction for intensities $10^{18}\,\mathrm{W\,cm^{-2}}$ if the laser focal spot size is sufficiently small ($< 1\mu$m). Such a small size of focussed intensity could be produced by a $f/1$ focussing optic, but is more likely to be produced if laser beam self focussing occurs in a plasma. For our experimental calculations utilised in chapter 5 (focal spot radius 3.5 μm), our modelling shows that channel formation is unlikely to cause significant additional electron acceleration.

Chapter 4

Experimental Diagnostics

4.1 Introduction

This chapter describes the experimental methods and diagnostics which have been used to obtain the results reported in this thesis. One of the main diagnostic which has been used during the experiments is an electron spectrometer for detecting fast electrons produced in laser plasma interactions. An optical probe shadowgraphy technique was used to provide information on density profiles of a laser produced plasmas. This chapter will also discuss silicon diodes used to detect x-ray emission.

4.2 Electron Energy Spectrum Measurements

This section will describe the electron spectrometer used in the experiment reported in chapter 5. We explain how the energy and the number of electrons in an energy range is deduced with the spectrometer and make estimates of the error involved in measuring these quantities.

The electron spectrometer consist of an electro magnet with circular pole pieces of radius $R = 2.54$ cm producing a uniform magnetic field of $B_{spec} = 0.15$ T. The electrons are deflected by the magnetic field onto a detector plane with image plate detector so that the degree of deflection is inversely proportional to the electron energy in the relativistic limit [87].

4.2.1 Dispersion of Electrons by a Circular Magnetic Field

The magnetic field of the spectrometer deflects energetic electrons due to the Lorentz force acting on the electrons (see figure 4.1). The rate of change of the electron momentum $\mathbf{p}$ with time is such that

$$\frac{d\mathbf{p}}{dt} = \frac{-e}{\gamma m_e}\mathbf{p} \times \mathbf{B_{spec}} \tag{4.1}$$

where e is the electron charge, m_e is the electron rest mass and γ is the relativistic mass increase.

In the following, we assume $\mathbf{y}$ is the initial electron propagation direction, $\mathbf{z}$ is the magnetic field direction (out of the page in figure 4.1) and $\mathbf{x}$ is the direction along the detection plane (aligned normally to $\mathbf{y}$).

The magnetic field within the pole pieces of radius R is taken to be given by

$$\mathbf{B_z}(\mathbf{r_b}) = \begin{cases} B_{spec}\mathbf{z} & (r_b \leq R) \\ 0 & (r_b > R) \end{cases} \tag{4.2}$$

where r_b is the radius from the centre of the magnetic pole pieces.

There is an analytic solution for the angular dispersion of electrons passing through the circularly shaped magnetic field which has been determined by the

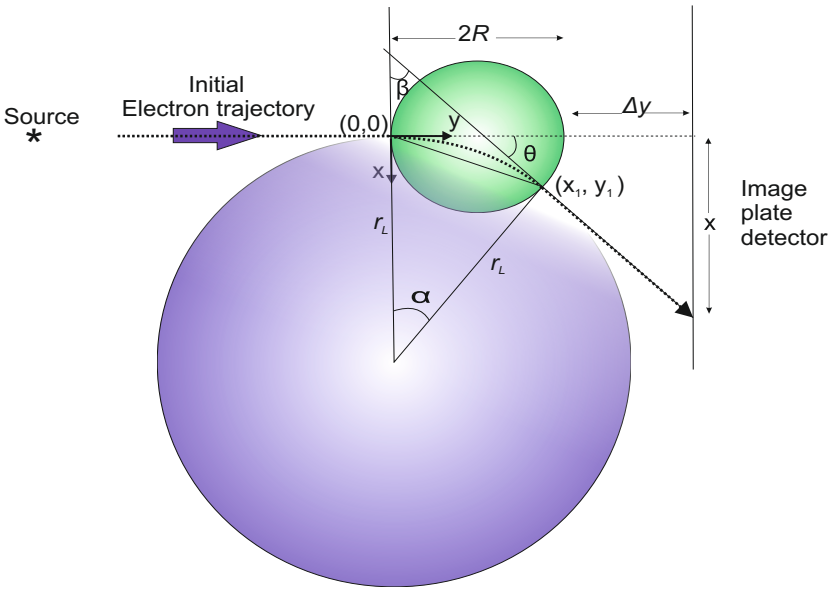

Figure 4.1: A schematic of the electron trajectory on passing through the magnetic field (green circle) of the electron spectrometer. The big purple circle circumference represents the Larmor orbit of the electron in the magnetic field.

author. Figure 4.1 shows the electron trajectory and the magnetic field position and the Larmor radius which is used for the analytic solution of the electron dispersion. An electron follows a path within the magnetic field with Larmor orbit radius r_L in the x-y plane such that,

$$r_L = \frac{p}{eB_{spec}} \quad . \tag{4.3}$$

Equation 4.3 is valid for both relativistic and non-relativistic electrons. From the geometry, we can write equations for the two circles on figure 4.1 assuming an origin (0,0) as marked.

For the magnetic field

$$x^2 + (y - R)^2 = R^2 \quad . \tag{4.4}$$

For the Larmor orbit

$$(x - r_L)^2 + y^2 = r_L^2 \quad . \tag{4.5}$$

Solving equations 4.4 and 4.5 for the position where the two circles intersects yields that $yR = xr_L$. Using this relationships, the point $(x_1,\ y_1)$ where the electron exits the magnetic field region is such that

$$x_1 = \frac{R}{r_L}\left(\frac{2R}{1+\left(\frac{R}{r_L}\right)^2}\right) \quad , \qquad\qquad y_1 = \frac{2R}{1+\left(\frac{R}{r_L}\right)^2} \quad . \tag{4.6}$$

The angle α of electron travel on the Larmor orbit is equal to the deflection angle θ of the electron as it exits the magnetic field. In addition, we have that

$$\sin\left(\frac{\alpha}{2}\right) = \frac{\left(\left(\frac{x_1}{2}\right)^2 + \left(\frac{y_1}{2}\right)^2\right)^{1/2}}{r_L} \tag{4.7}$$

$$= \frac{R}{r_L}\frac{1}{\left(1+\left(\frac{R}{r_L}\right)^2\right)^{1/2}} \quad . \tag{4.8}$$

The equation through the point (x_1, y_1) at angle β where $\beta = 90 - \alpha$ is ;

$$y - y_1 = (x_d - x_1)\tan(\beta) \quad . \tag{4.9}$$

This equation intersects the image plate detector where $y = 2R + \Delta y$ so ;

$$2R + \Delta y - y_1 = (x_d - x_1)\tan(90 - \alpha) \tag{4.10}$$

and the distance x_d along the detector plane is given by

$$x_d = \frac{2R + \Delta y - y_1}{\tan(90 - \alpha)} + x_1 \quad . \tag{4.11}$$

Combining these equations gives the dispersion distance x_d along the detection plane in an exact form. We have ;

$$x_d = \left[2R + \Delta y - \frac{2R}{1 + \left(\frac{R}{r_L}\right)^2} \right] \tan(\alpha) + \frac{2R^2}{r_L} \frac{1}{1 + \left(\frac{R}{r_L}\right)^2} \tag{4.12}$$

where α is given by

$$\alpha = 2\sin^{-1} \left[\frac{\mathrm{R}}{\mathrm{r_L}} \frac{1}{\left(1 + \left(\frac{\mathrm{R}}{\mathrm{r_L}}\right)^2\right)^{1/2}} \right] \quad . \tag{4.13}$$

Figure 4.2 indicates the relationship between electron energy and angular deflection for three different magnetic fields and magnetic field radii calculated using equations 4.12 and 4.13. In each case, the deflection angle α is close to being inversely proportional to the electron energy. We have that $\alpha \propto 1/E$ for small angle deflections ($< 40°$). The dispersion of the magnet changes linearly with the field radius R and field amplitude B_{spec} (proportionally to RB_{spec}). The electron spectrometer is capable of measuring high energy electrons with a small region of high magnetic field or a small magnetic field in a larger area.

Assuming $r_L \gg R$, equation 4.12 can be written as;

$$x_d \cong \frac{2R}{r_L} [R + \Delta y] \quad . \tag{4.14}$$

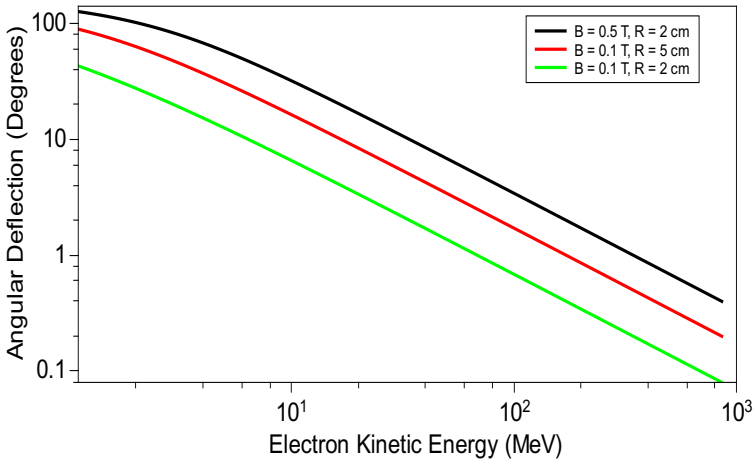

Figure 4.2: The angular deflection α of electrons passing through a magnetic field of strength as shown with circular pole pieces of radius (as shown). The deflection angle α is approximately inversely proportional to the electron energy E and depends on the B magnetic field amplitude and R the radius of the magnetic field.

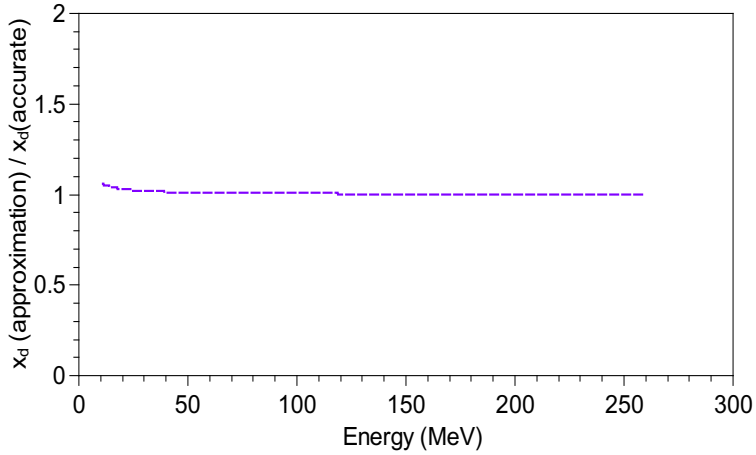

Figure 4.3: The approximate dispersion distance x_d is compared to the accurate x_d dispersion values for highly relativistic electron energies.

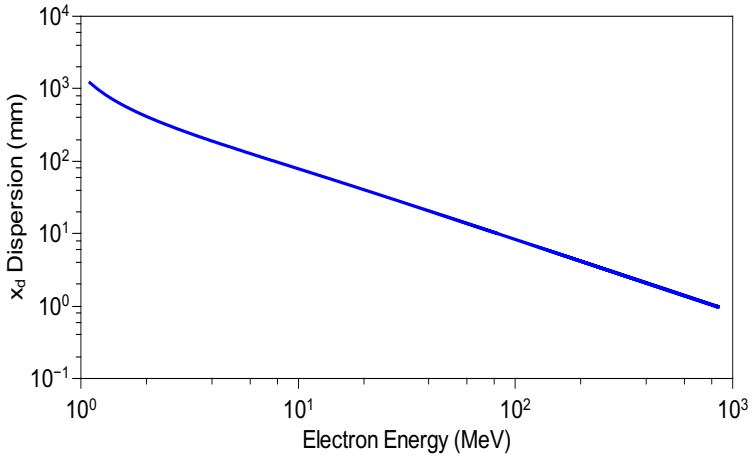

Figure 4.4: The dispersion x_d of electrons passing through the electron spectrometer. Their dispersion distance is approximately inversely proportional to the electron energy $x_d \propto 1/E$. A magnetic field of $B_{spec} = 0.15$ T is applied to the electrons (with $R = 2.54$ cm, $\Delta y = 31.5$ cm).

The accuracy of the approximation that $r_L >> R$, is examined on figure 4.3. We see that the error in neglecting the spherical shape of the magnetic pole pieces is less than %3.

In the non-relativistic limit, applying the Larmor radius $r_L = \frac{m_e v}{eB}$ to equation 4.14 and writing v in terms of energy (E) gives;

$$x_d = \sqrt{2}\, R(R + \Delta y)\, \frac{eB}{m_e^{1/2} E^{1/2}} \quad . \tag{4.15}$$

This result has also been determined by, for example, Lezius et al [88].

For highly relativistic electrons, we use the Larmor radius given by equation 4.3. Applying the relativistic approximation $E = pc$ gives the result for x_d that;

$$x_d = 2R(R + \Delta y)\frac{ecB}{E} \quad . \tag{4.16}$$

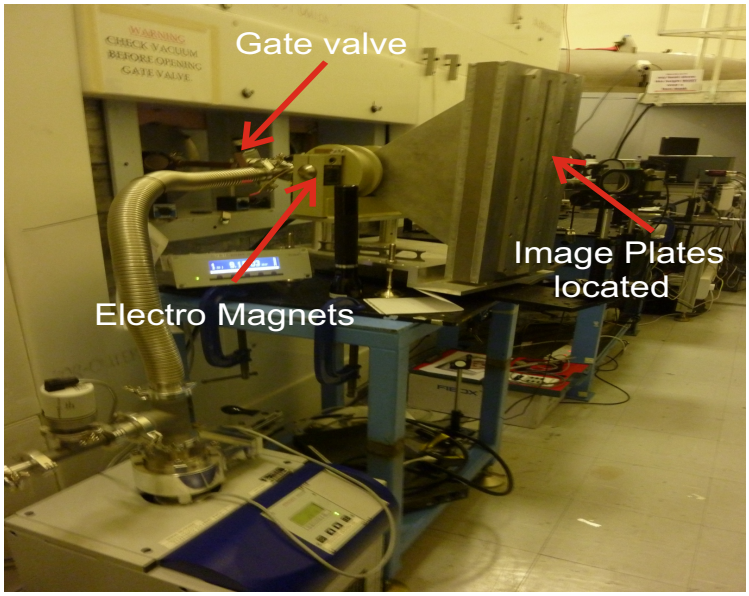

Figure 4.5: An image of the electron spectrometer used during an experiment at the target area Petawatt at the Central Laser Facility described in chapter 5

.

This shows that the dispersion is inversely proportional to the electron energy E in the relativistic regime.

4.2.2 The Effect of Magnetic Fringing Fields

In section 4.2.1, the dispersion of the electron spectrometer has been calculated without taking into account a fringing field created by the electromagnets. In this section, we calculate the effect of the fringing magnetic field which is produced on the edge of the electro magnets. In the design of the electron spectrometer, a yoke has been used to reduce unwanted fringe fields pointing in the opposite direction of the usual magnetic field [87]. Figure 4.6 shows the fringing field from the electro magnet schematically. The electrons are affected by the magnetic field before entering and after leaving the magnets. Measurements have been undertaken by

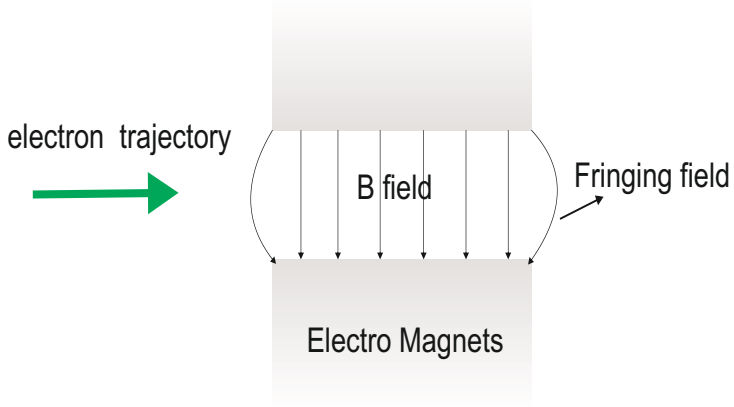

Figure 4.6: Schematic demonstration of the fringing field on magnets.

Murphy [89] using a single axis hall probe to map the actual magnetic field of the electromagnets employed for this thesis (see figure 4.7).

The dispersion of electrons is increased by taking into account the fringing field effect. The effect of the variation of electron momentum perpendicular to the initial direction of electron momentum due to a fringing field can be obtained by integrating over the fringing magnetic field. The change in electron momentum due to the fringing field $B(y)$ is given by

$$\Delta p = \frac{-e}{m\gamma}\frac{p}{c}\int B(y)dy \tag{4.17}$$

assuming that the electrons are relativistic with $dy = cdt$ and the integration is over the fringing field.

From the spectrometer to the image plate detector, we have for relativistic electrons an electron momentum in the direction of the electron dispersion given

by

$$\Delta p_x(out) = -e \int_R^{\Delta y} B(y)dy \quad , \tag{4.18}$$

while from the target to the spectrometer, we have

$$\Delta p_x(in) = -e \int_R^{L} B(y)dy \quad . \tag{4.19}$$

The total effect on the spectrometer dispersion Δx of the fringing field is given by

$$\Delta x = \frac{\Delta p_x(out)\Delta y}{p_y} + \frac{\Delta p_x(in)(\Delta y + 2R)}{p_y} \quad . \tag{4.20}$$

Integrating the fringing field of figure 4.7, shows that the fringing field of the electro magnets causes an additional dispersion Δx, such that $\Delta x/x_d \backsimeq 0.4$, where x_d is the dispersion calculated neglecting fringing fields. For the calculations of electron energy spectra in chapter 5, a total dispersion distance such that

$$x_d(total) = x_d + \Delta x \tag{4.21}$$

has been used.

Figure 4.8 shows the relationship between electron energy and the total dispersion of electrons for our electron spectrometer (with $R = 2.54$ cm, $B_{spec} = 0.15$ T, $\Delta y = 31.5$ cm) calculated using equations 4.3, 4.12, 4.13 and 4.21. In the relativistic regime, where the energy $E \gg 0.511$ MeV, figure 4.8 shows that x_d(total) $\propto \frac{1}{E}$ in agreement with equations 4.16 and 4.21. Our calculations indicates that the relativistic assumption (equation 4.21) is accurate for energies $E > 2$ MeV.

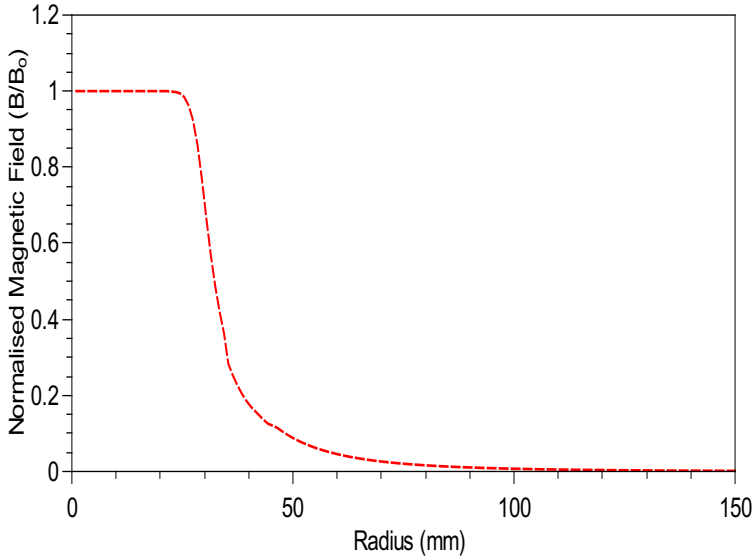

Figure 4.7: Measured magnetic field for the electron spectrometer as a function of radius from the centre of the electromagnet (taken from Murphy [89])

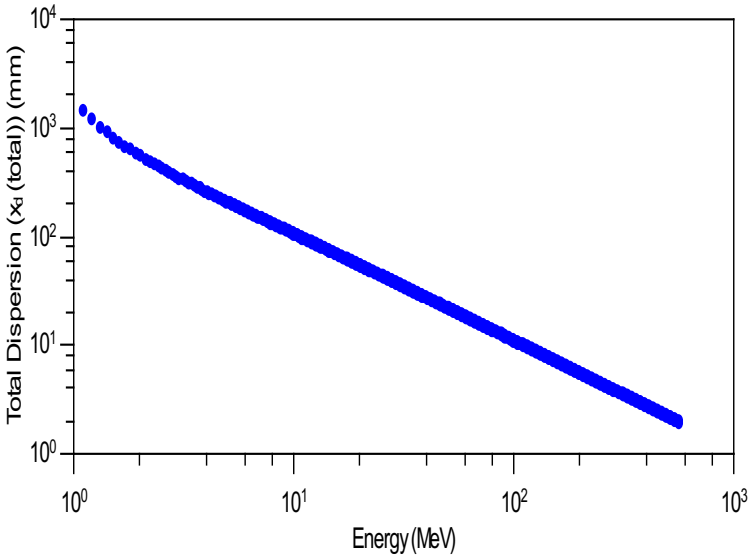

Figure 4.8: The total dispersion $x_d(total)$ of electrons passing through the electron spectrometer when the fringing field is taken into account. A magnetic field of $B_{spec} = 0.15$ T is applied to the electrons (with $R = 2.54$ cm, $\Delta y = 31.5$ cm)

Table 4.1: Parameters for the electron spectrometer used in the experiment.

Source to magnet centre distance	325 cm	x
Magnet centre to detector plane	34 cm	$R+\Delta$ y
Magnet pole radius	2.54 cm	R
Magnetic field amplitude	0.15 T	B_{spec}
Collimator solid angle	1.4×10^{-5} sr	Ω

In practical unit, we have from equation 4.21 that

$$x_d(total)(\text{mm}) = \frac{1025.5}{E(\text{MeV})} \quad . \tag{4.22}$$

4.2.3 Design of the Electron Spectrometer

The electron spectrometer used in this work was designed by Zulfikar Najmudin and his group at Imperial Collage London (see reference [87]). The dimensions of the electron spectrometer used during the experiment are summarized in table 4.1. Figure 4.5 shows an image of the electron spectrometer as used during an experiment in the Petawatt target area at the Central Laser Facility. The spectrometer is located outside the target chamber on the experiment. Figure 4.9 shows the design of the electron spectrometer engineering drawing.

4.2.4 Image Plates

Electrons were detected using image plates (Fuji film BAS-SR 2025 [90, 91]). Electron detection on the image plates is caused by photo-stimulated luminescence (PSL). A 120 μm thick layer of luminescent material is contained in the image plates under a 10μm protective layer of mylar [92, 93]. Deposited energy ionizes europium ions from Eu^{2+} to Eu^{3+} and the released electron is captured in a

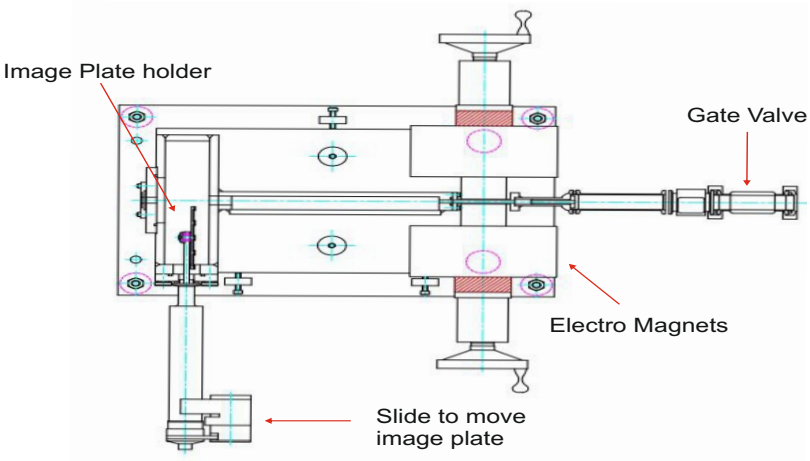

(a)

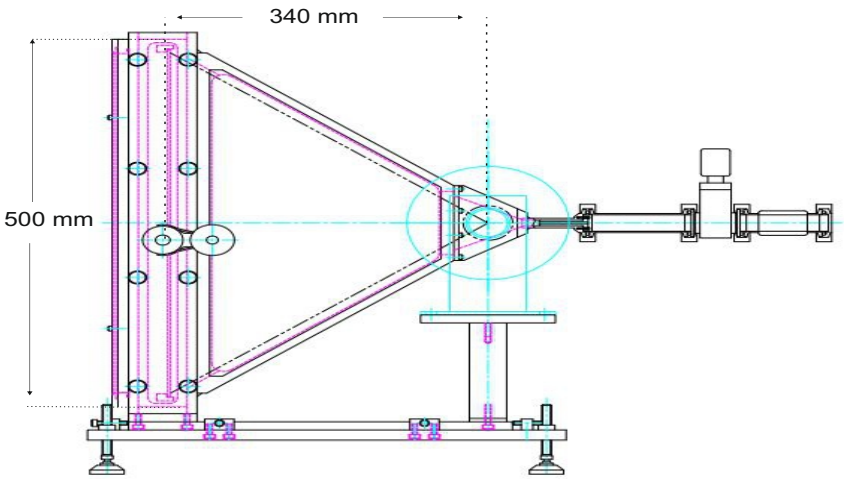

(b)

Figure 4.9: Engineering drawing of electron spectrometer which is used in the experiment a) viewing from top and b) shows the side view of the spectrometer. (Figure taken from CLF Engineering Department)

colour centre metastable state. The deposited energy is effectively stored as a latent image in the plate which can be read by exciting the electron out of the colour centre to the conduction band by visible irradiation.

From the conduction band, the electron recombines with Eu^{3+} to produce Eu^{2+} with the emission of a measurable photon. The amount of energy deposited in the plate is directly related to the number of excited europium ions and the eventual photon emission (after laser irradiation).

The image plate is read using a scanner (FLA 5000) [90]. The surface of the image plate is scanned by visible lasers of wavelength suitable for further excitation of the metastable states generating PSL radiation which is read by a photo multiplier tube (PMT) which converts the optical signal in an electric signal. The spatial resolution is generally 25 μm to 50 μm.

Previous experiments show that image plates accurately measure the total electron energy impinging on the plates [63, 94–96].

An AWE calibration shows that 50 μm resolution scanned image plates have 50 keV energy recorded as 50 electron per PSL [97] for BAS IIIS image plates. The PSL is the digitised unit of exposure recorded by the image plate scanner.

Other image plate calibrations show that the sensitivity of the electron response in the range of 1 to 100 MeV electron energy remains constant [92, 98, 99]. For example, BAS SR 2025 type image plate has been calibrated for 11.5, 30 and 100 MeV electron energies with image plate response of 0.0074 PSL, 0.007 PSL and 0.0064 PSL per electron, respectively [92]. These calibrations also show that when a 200×200 μm square is set for the signal scanning on image plates, the resolution of the electron energy spectrum is 20 keV at the lowest end and 400 keV at the highest point.

A logarithmic compression QL of the PSL data is obtained after scanning of image plates because the outputs of the photomultiplier tubes are logarithmically amplified and are converted with an A/D converter into digital signals (16 bits/pixel) [100, 101]. The conversion from this quantum level QL to PSL intensity is following the relationship

$$PSL = \left(\frac{R}{100}\right)^2 \left(\frac{4000}{S}\right) 10^{L\left(\frac{QL}{G} - \frac{1}{2}\right)} \tag{4.23}$$

where R is the scan resolution in μm, S and L are settings on the scanner called the sensitivity and latitude (set to $S = 4000$ and $L = 5$) and G is the bit depth of the scan ($G = 65535$ for 16 bit scans). Since the QL is proportional to the logarithm of the PSL level, it is important to convert raw data QL to the PSL level before any analysis.

It has been shown that PSL signal levels vary as a function of time before exposure and read-out. In 10 minutes PSL signals can be reduced by 10%, [102] so it is important that data is scanned in a constant time interval after exposure. Our scanning of this image plates was undertaken within 3 minutes of exposure.

4.2.5 Electron Spectrometer Error Calculations

When using the electron spectrometer, the exposure of the image plate is proportional to the deposited energy from hot electrons, while the deviation of the electrons in the magnetic field gives the electron energy. To determine the number dn/dE of hot electrons within an energy range E to $E + dE$ we have that;

$$\frac{dn}{dE} \propto \frac{1}{E} \frac{dN_{sig}}{dE} \tag{4.24}$$

where dN_{sig} is the image plate exposure, over the energy range E to $E + dE$. Calibrations (discussed above) show that the image plates (BAS SR 2025) record 50 keV of electron energy as ~ 0.007 photo-stimulated luminescence (PSL) (1PSL $\backsimeq$ 150 electron) for the range of 1 to 100 MeV [87, 92]. The deviation x_d(total) of electrons of energy E in the spectrometer is such that $x_d(\text{mm})(total) = \frac{1025.5}{E(\text{MeV})}$ (see section 4.2.1 and 4.2.2) giving for the electron spectrometer that

$$\frac{dn}{dE} \propto \frac{1}{E^3}\frac{dN_{sig}}{dx_d} \tag{4.25}$$

where $\frac{dN_{sig}}{dx_d}$ is the signal per unit length along the image plate. The fractional error in the number of electrons detected per unit energy range is thus given by

$$\frac{\Delta\left(\frac{dn}{dE}\right)}{\frac{dn}{dE}} = 3\frac{dN_{sig}}{dx_d}\frac{\Delta E}{E}. \tag{4.26}$$

The error ΔE in the measurement of the energy of the electrons is related to the error measurement Δx_d of distance x_d(total) along the image plate such that

$$\frac{\Delta E}{E} = -\frac{\Delta x_d}{x_d(total)}. \tag{4.27}$$

Sample electron energy spectra showing an estimated error on the number of electrons and electron energy are shown in figure 4.10. The absolute errors in $\frac{dn}{dE}$ versus E shown in figure 4.10 are evaluated using equations (4.26) and (4.27) with $\Delta x_d = 1$ mm which is the uncertainty of the centre of the highest energy point corresponding to undeviated electrons. The electrons are collected by an aperture of area 7.85×10^{-5} m^2 and distance 2.37 m from the target, implying a solid angle of collection of 1.4×10^{-5} sr. The electron numbers detected at each

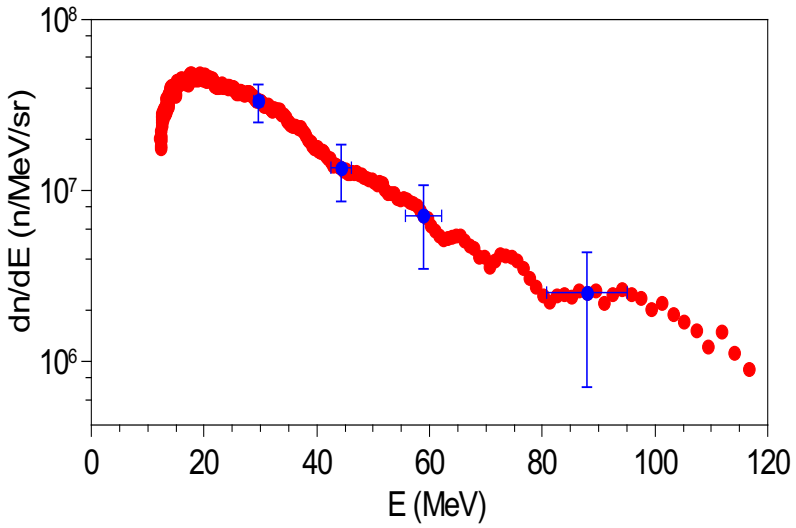

Figure 4.10: A sample electron energy spectrum for a 2.5×10^{12} W cm^{-2} pre-pulse and 5.1×10^{20} W cm^{-2} main pulse intensity on a target showing the absolute errors in the number of electrons and their energy. The electron spectrometer was positioned at the rear side of the target viewing along the laser axis (see chapter 5).

energy are integrated in the non-energy dispersion direction to give a spectrum measured in units of MeV^{-1} sr^{-1}. Low energy electrons (<10 MeV) are affected by space charge and magnetic field effects near the target and consequently their numbers are not recorded accurately.

4.3 Optical Probe Shadowgraphy

Shadowgraphy can be used to gain information about the variation of plasma scale length in an expanding laser produced plasma. The refraction of the probing rays along the target surface depends on the electron density gradient.

Consider a slab of plasma with two rays passing through a distance dz apart (see figure 4.11). The optical path length difference between the two rays is $\lambda\frac{d\phi}{2\pi}$

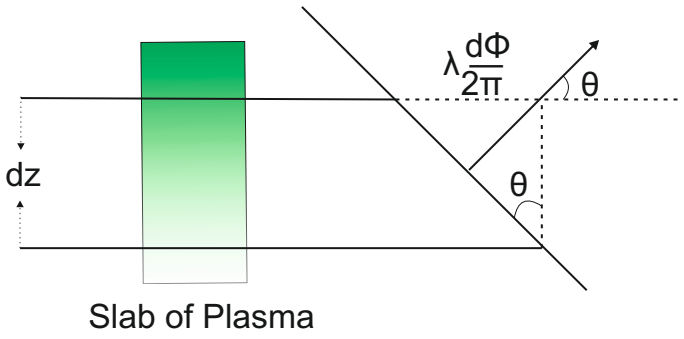

Figure 4.11: Slab of plasma to derive refraction effect.

where λ is the wavelength of the probe light and $d\phi$ is the phase difference. The direction of propagation beam is perpendicular to the resultant phase front. So the angle of diffraction is

$$\theta = \frac{\lambda \frac{d\phi}{2\pi}}{dz} = \frac{d}{dz} \int N dl \tag{4.28}$$

where N is the plasma refractive index.

Assuming an exponential electron density gradient such that the electron density varies with distance z from the target surface such that

$$n_e(z) = n_e(0) \exp(-\frac{z}{L}) \tag{4.29}$$

where L is the electron density scale length, the rays initially parallel to the target surface are deflected by angle [103, 104]

$$\theta = \frac{n_e(z)}{2n_c} \frac{\Delta y}{L} \tag{4.30}$$

for a uniform plasma of width Δy. Here n_c is the critical density for the

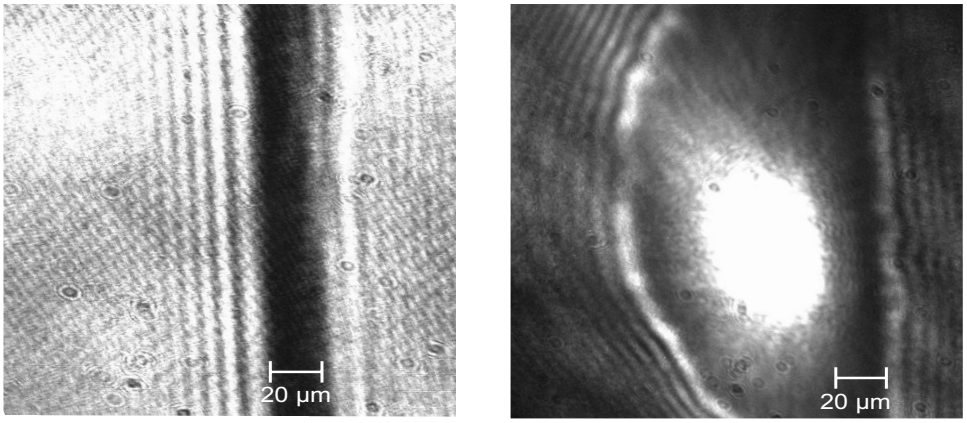

Figure 4.12: An example of shadowgraph, showing generated plasma after the laser shot. Figure a) shows the reference target before the shot and b) shows the same target after the shot irradiated by 2.2×10^{12} W cm^{-2} pre-pulse and 3.8×10^{20} W cm^{-2} main pulse intensity. (b) is taken at the time of peak laser irradiance.

probing radiation. We assume that $n_e(z) \ll n_c$, so that the plasma refractive index is given by $1 - \frac{n_e(z)}{2n_c}$. For an experiment described in chapter 5 with beam imaging optics of $f/5.3$, rays of angle $\theta > \theta_{max} = 0.08$ radian are not detected. Plasma regions where $\theta > \theta_{max}$ appear black in the shadowgrams (see figure 4.12).

Figure 4.12 shows an example of shadowgraph images which was taken during the experiment described in chapter 5 for a 20 μm thick plastic target before and after irradiation by a 2.2×10^{12} W cm^{-2} pre-pulse and 3.8×10^{20} W cm^{-2} main pulse intensity. The shadowgraphy technique allows quantitative information on the scale lengths of the probed plasmas and enables the visualisation of the geometry of the generated plasma.

4.4 Silicon Diode Array

Hot electrons generated by moderate laser intensities ($3 \times 10^{16}\,\mathrm{W\,cm^{-2}}$) cause Bremsstrahlung emission. X-ray emission varies as $\varepsilon(E_p) \propto \int_{E_p}^{\infty} E^{-1/2} f(E) dE$, where $f(E)$ is the electron energy distribution function, so the recorded photon emission can be used to extract hot electron temperatures [105–107].

Filtered silicon diodes are used to record plasma electron temperatures in chapter 6. In this section, the operation and background theory explaining the use of a filtered diode array is reviewed.

4.4.1 Theory of Photodiodes

Silicon photo diodes comprise p and n-type semi conductors joined together or each joined to an intrinsic layer of silicon. In p-type semiconductors, holes are the majority carriers and electrons are the minority carriers. While in an n-type semiconductor, electrons are the majority and holes are the minority carriers. In an n-type semiconductor, the Fermi energy level is greater than that of the intrinsic semiconductor and lies closer to the conduction band than the valence band while in p-type semiconductor, the Fermi energy level is closer to the valance band (see figure 4.13) [108, 109]. When a potential is applied across the junction between n and p-type semiconductor, the built in electric field applies a force (the drift force) on holes and electrons.

In photodiodes, a pn junction is utilised where a boundary is created between p-type material and n-type material known as the depletion region is created. An incident photon with a sufficient energy can excite an electron from the valance

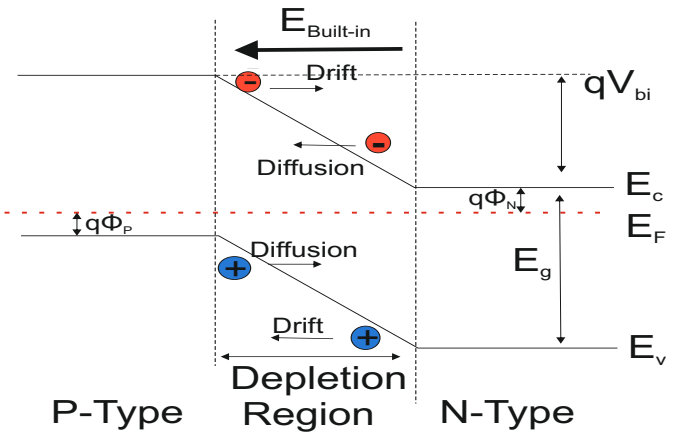

Figure 4.13: Energy band structure of a p-n junction. in thermal equilibrium. $\mathbf{E}_{built-in}$ is the electric field created in the depletion region, E_c and E_v are the energy of conduction band and valance band. E_F represents the Fermi energy level and E_g represents the band gap energy. V_{bi} is the built-in potential, ϕ_P and ϕ_N are the potential difference of holes to the Fermi energy level and for electrons to the conduction band energy level, respectively.

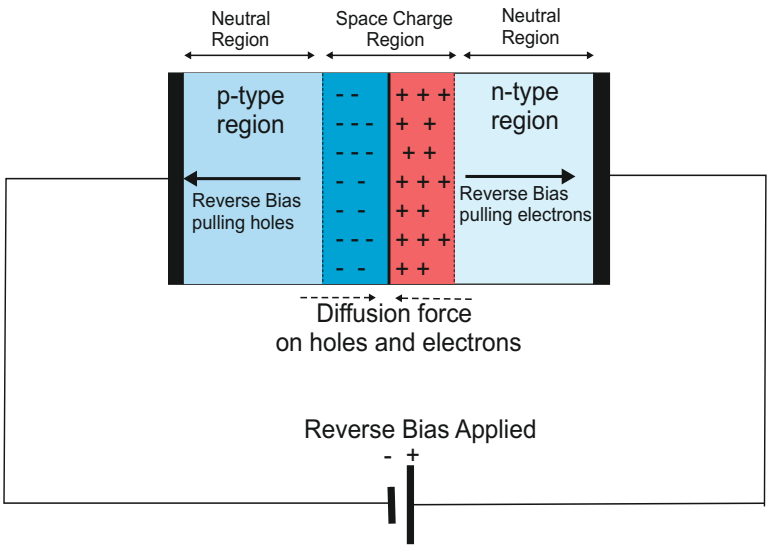

Figure 4.14: Cross section of a p-n junction diode with applied reverse bias.

band to the conduction band of the semiconductor, creating electron-hole pairs which move to complete an external circuit. In silicon, the required energy to create an electron-hole pair is 3.63 eV of incident energy for photons with energy greater than 30 eV [110, 111]. Optical photons with energy above the silicon band gap energy (1.1 eV), produce a single conduction band electron, but with higher photon energies, many electrons can be excited limited by phonon production.

Photodiodes can be operated in a photovoltaic or photoconductive mode. If there is no bias applied across the diode and incident light creates electron-hole pairs, it is called the photovoltaic mode. The photoconductive mode requires a reverse bias across the diode. A photodiode can be reverse biased by applying the negative terminal of the voltage source to the p-type side and positive terminal is connected to the n-type side of the p-n junction (see figure 4.14). When this additional voltage is introduced to the diode, holes and electrons are pulled away from the depletion layer, increasing the width of the depletion layer and preventing current flowing if the light is not impinging. Increasing the voltage increases the width of the depletion layer, until a critical value corresponding to a breakdown voltage is reached [108, 109].

Incident photons penetrating into the depletion layer generate electron-hole pairs with electrons excited from the valence band to the conduction band of the semiconductor. The diodes employed in chapter 6 are XUV-100 diodes manufactured by OSI Optoelectronics [112] (see figure 4.15). They are used to investigate the x-ray region of the spectrum between 10 keV and 40 keV so the depletion layer must be thick enough to absorb significant number of photons inside the depletion region. The depletion layer thickness is 5 mm for the diode employed. The sensitivity of the photo diode was not efficient enough to detect higher energetic

Figure 4.15: X-ray diodes mounted on plastic flange with BNC feedthroughs (left) and covering aluminium housing (right). Each diode covers a 12 mm active region.

photons sufficiently (see figure 4.16) so it was important to investigate the energy region where the photons can be absorbed. Figure 4.16 shows the quantum efficiency of silicon photo diode with a 5 mm silicon depletion layer transmission as a function of photon energy. The sensitivity of the photo diode is given on the company website up to 17.6 keV photon energy [112] where the silicon absorption is %100 efficient. Previous studies show that the diode responsivity increases up to 30 keV then responsivity remains constant [113]. Assuming quantum efficiency increases linearly up to the 30 keV and then remains constant, using the photon absorption of a 5 mm silicon depletion layer, the quantum efficiency as a function of photon energy can be calculated (figure 4.16). The red line shows the quantum efficiency which has been taken from the company website and blue line shows our calculations of quantum efficiency for the higher energetic photons. Above 40 keV, the diode sensitivity decreases since the radiation absorption in the depletion

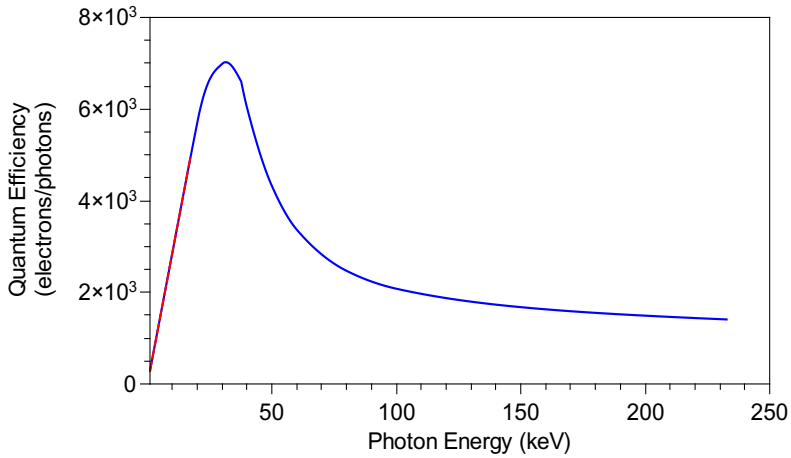

Figure 4.16: Quantum efficiency of silicon photo diode as a function of photon energy. The red line shows the data taken from the company website and blue curve shows the completed quantum efficiency for higher energies.

layer of silicon decreases. This relationship was taken into account in determining the response of the diodes.

4.4.2 Filters

Filters are applied to attenuate different spectral ranges of photons so that the signal from several photodiodes with different filtering enables a deduction of the x-ray spectrum. We assume that the spectrum exhibits an exponential variation of emission ε varying with photon energy $h\nu$, such that

$$\varepsilon \propto \exp\left(-\frac{h\nu}{kT_e}\right) \quad . \tag{4.31}$$

Such a variation is associated with free-free emission or over limited spectral ranges free-bound emission (see section 2.5). The temperatures kT_e here is associated with a hot, non-thermal temperature appropriate to a small number of

Table 4.2: Filter components used for XRD diagnostic, optimised for the energy range 10-40 keV.

Channel Number	Filter Components
Channel 1	75 μm Al
Channel 2	150 μm Al
Channel 3	75 μm Ti
Channel 4	100 μm Cu

electrons in the plasma.

A simple exponential variation of emission as presented in equation 4.31 can be assured if the spectral range is sufficiently high that $h\nu$ is greater than any spectral line or free-bound edge spectral feature.

Filter transmission is calculated using mass attenuation coefficients (μ/ρ (cm^2/g)) which can be found, for example, at reference [73]. Photons with an incident intensity I_0, penetrating a layer of material with mass thickness x (g/cm^2) and density ρ (g/cm^3), emerge with intensity I given by the exponential attenuation law;

$$I/I_0 = \exp(-(\frac{\mu}{\rho}(E_p))x)\cdot \tag{4.32}$$

For the diode array used in chapter 6, each of four diodes is covered with a different filter to restrict the recorded spectral region. The diodes were filtered to mainly record the photon emission above 10 keV so that there is a negligible effect of thermal temperature ($\sim$ 500 eV) plasma on the recorded signal.

The four filters chosen for this diagnostic used a combinations of metal foils in different thicknessess and were chosen to optimise the deduction of the hot electron temperature in the energy regime between 10 to 40 keV. Table 4.2 shows the selected filters.

Combining equation 2.34 and the transmission of each filter gives the trans-

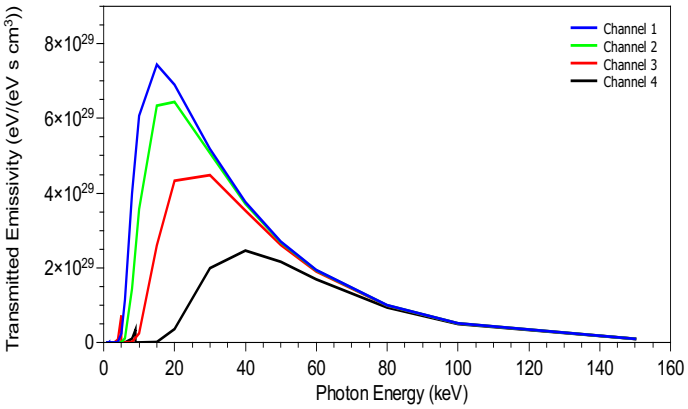

Figure 4.17: Transmitted emissivity from a laser produced plasma with a hot electron temperature of 30 keV. Filters 1,2,3 and 4 are represents by the blue, green, red and black lines, respectively.

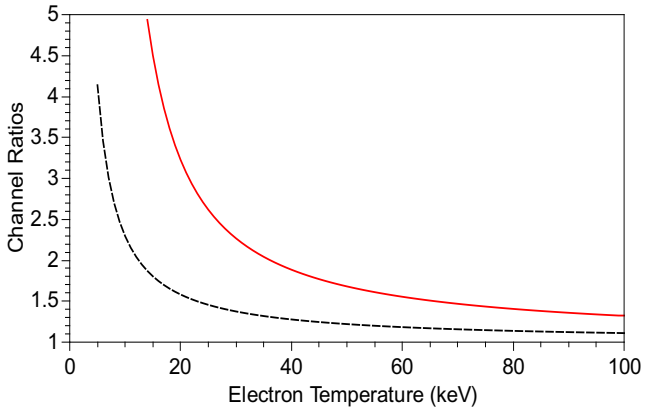

Figure 4.18: The variation of diode signal ratios as a function of the hot electron temperature. Red line shows the ratio of channels 1 and 4, while the black dashed line shows the ratio of channels 1 and 3.

mitted emissivity as a function of incident photon energy assuming x-ray emission is as given by equation 4.31 (see figure 4.17).

Assuming all emission originates from the same volume of plasma over the same time period, plasma volume and emission time terms cancel out if the ratios of channel signals are used. Figure 4.18 shows the variation of the diode signal ratios as a function of hot electron temperature. Hot electron temperatures can be calculated for different shots by using figure 4.18.

4.5 Conclusion

Diagnostics used in the work of this thesis have been presented. An electron spectrometer for measuring energetic electron energies in the range 15 MeV to 120 MeV has been discussed. A detailed expression for the dispersion, fringing field effect on the dispersion and error of measurement has been presented. An optical probing technique to measure length scales in plasmas and an x-ray diode array for measuring hot electron temperature has been presented.

Chapter 5

Hot Electron Production in Laser Solid Interactions With a Controlled Pre Pulse

5.1 Introduction

The experiment described in this chapter used the Vulcan Petawatt laser at the Rutherford Appleton Laboratory, UK. This laser is capable of delivering 500 J pulses with a duration of 500 fs in a micron level focal spot corresponding to laser intensities $\sim 10^{21}$ W cm^{-2}. The motion of electrons in this laser field can be highly relativistic.

Petawatt lasers allow extremely high irradiance ($> 10^{18}$ W cm^{-2}) laser interaction with high density targets for a number of applications. Such lasers may enable fast ignition inertial fusion at lower total laser energy by creating hot electrons which initiate fusion ignition in a compressed deuterium-tritium fuel [5].

The high irradiance used in the present work has produced electrons of temperature 20-30 MeV much greater than required for fast ignition (2-3 MeV). However, it is important to measure and understand the created electron spectrum for other applications. For example, hot electrons enable the production of high energy ions as their dynamics establish steep gradients of electric potential [114, 115].

At irradiances $> 10^{18}$ W cm^{-2}, electrons with velocities close to the speed of light are generated such that relativistic mass increases are important in their motion. For example, quasi-mono energetic electron energies up to GeV levels have been measured at irradiances $\sim 10^{18}$ W cm^{-2} with gas jet targets where a wake-field can form [96, 116]. However, electron temperatures only up to 10 MeV at irradiances of $\sim 10^{19}$ W cm^{-2} have been measured in high contrast laser - plasma interactions on solid targets where there is little pre-plasma on which the high contrast irradiance beam interacts [44, 94, 117]. The importance of pre-formed plasma in the acceleration of ions in laser-plasmas has been examined [53, 54, 118, 119], but the numbers and temperatures of hot electrons in measured scale length plasmas at irradiances $\simeq 10^{20}$ W cm^{-2} have not been reported previously.

High irradiance lasers accelerate electrons by different mechanisms when they interact with a high density target. Resonance absorption at irradiance $> 10^{14}$ W cm^{-2} causes acceleration of electrons at the critical density if the light is incident at an angle to the target normal and is p-polarized [31, 41, 66]. Raman scatter [120–123] and two-plasmon decay [31, 124] can accelerate electrons when laser light propagates in densities up to 1/4 of the critical electron density. Brillouin scatter [31, 125] can cause electron acceleration at densities up to the critical density. Ponderomotive acceleration of electrons proportional to ∇I occurs at high irradiance I ($> 10^{18}$ W cm^{-2}) in a direction perpendicular to the laser

incidence [33, 126]. Acceleration in the direction of the laser results from electron quiver velocities due to the laser electric field interacting with the laser magnetic field [15].

The production of the highest energy electrons requires electron acceleration over a significant length. Channel formation in gas jet targets has enabled electron acceleration over larger lengths (up to 3.3 cm) via the formation of wake-fields. Other channel acceleration mechanisms have been proposed [56, 58, 127, 128] and experimentally observed [84]. In this thesis, we present evidence for the acceleration of significantly more electrons when a high irradiance laser interacts with plasma produced from a solid target by a laser pre-pulse. The generation of large numbers of fast electrons is significant for fast ignition inertial fusion and also in applications where hot electrons set up potential gradients resulting in the acceleration of ions to high energy [129, 130].

This chapter present the measurement of the number and temperature of hot electrons obtained using an electron spectrometer. The results are correlated to the density scale length of the plasma produced by a controlled pre-pulse measured using an optical probe diagnostic. The experimental results show that longer interaction plasmas produced by pre-pulses enable significantly greater number of hot electrons to be produced.

5.2 Experimental Design

The petawatt laser at the Rutherford Appleton Laboratory (RAL) delivered 1.054 μm wavelength laser pulses of 0.7 - 1.1 ps duration and pulse energies 150 $\pm$ 20 J with an intensity contrast of 10^8. These pulses were focused using an f/3

parabolic mirror to a 7 μm (FWHM) spot. A peak intensity of 10^{20} W cm^{-2} in a p-polarized beam was incident at 40° angle to the plane target normal (see figure 5.1). A longer duration (5 ns) prepulse was incident at 17° incidence angle

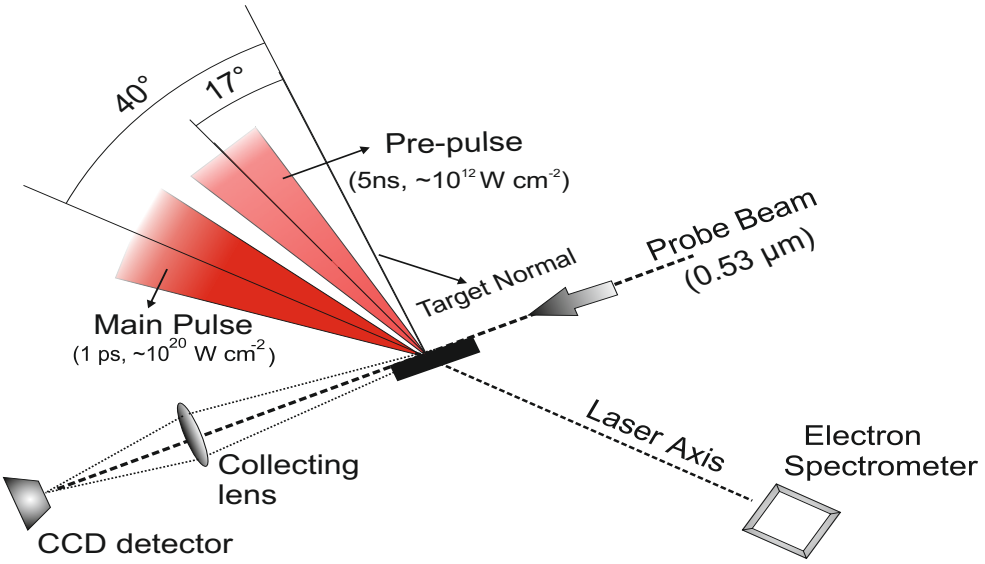

Figure 5.1: Experimental setup in the Vulcan Petawatt Laser Facility.

with the peak of the pulse 1.5 ns before the short pulse. A phase zone plate was utilised to produce a uniform focal region of this pre pulse over the short pulse focal diameter (the pre pulse focal diameter was 300 μm with an approximate top hat profile). The main (1ps) pulse was incident into the centre of the pre-pulse focal region. Plane foil targets of CH in various thicknesses from 6 μm to 150 μm were used. The targets contained a thin (100 nm) layer of aluminium buried at depth $\geq$ 3 μm from the target surface. For results presented here, the variation of measured parameters did not change with target thickness or the depth of the aluminium layer. The Al layer ionises to produce a similar electron density to

mass ratio as plastic.

Figure 5.1 shows the experimental layout of the target chamber and the diagnostics. The main diagnostics utilised were an electron spectrometer, measuring the energy spectrum of the accelerated electrons and an optical diagnostic measuring plasma scale length using frequency doubled laser light (both described in chapter 4).

The electron spectrometer with the detectors was located outside the main target chamber volume attached to the main chamber by a 25 mm diameter vacuum pipe so that electrons could propagate to the electron spectrometer in vacuum. As the electron spectrometer is housed outside the main chamber, background signal on the electron spectrometer image plate detectors is significantly reduced. The background signal mainly comes from x-rays which are produced in the interaction or due to the bremsstrahlung radiation emitted as the electron beam interacts with material in the chamber.

The electron spectrometer used in this experiment is described in chapter 4. Electrons were collected by an entrance aperture of area 7.85×10^{-5} m^2 and distance 2.37 m from the target, implying a solid angle of collection of 1.4×10^{-5} sr. The image plate detectors were placed perpendicularly to the initial electron path 34 cm away from the centre of the magnetic field region.The image plates were located above and below the spectrometer axis to measure both the signal due to the x-ray background and electrons.

Spectra were recorded with FUJI BAS SR 2025 image plates and scanned using an FLA 5000 image plate scanner with a resolution of 25 μm. Background x-rays were observed on both side of the electron signal so the averaged background x-ray signal was subtracted from the main electron signal.

An optical probing diagnostic was employed in the experiment to measure the scale length of plasma formed by the pre pulse. A frequency doubled optical probe beam was used to record the expansion profile of the plasma at the time of the interaction pulse. The probe beam was directed parallel to the target surface passing through the plasma produced by the longer pulse laser target interaction. Images were recorded using a 40 cm focal length and 7.5 cm diameter collection optic which imaged the target onto a CCD camera (see figure 5.10). The probe beam was split from the amplified oscillator pulse creating the $\sim$ 1ps main pulse and had a total energy of $\sim$ 360 mJ after frequency doubling. The CCD detector was filtered using a 4 ND filter and a narrow band filter and the probe beam frequency doubled to reduce the recording of plasma scattered laser light. Figure 5.2 shows the experimental set up for the shadowgraphy technique.

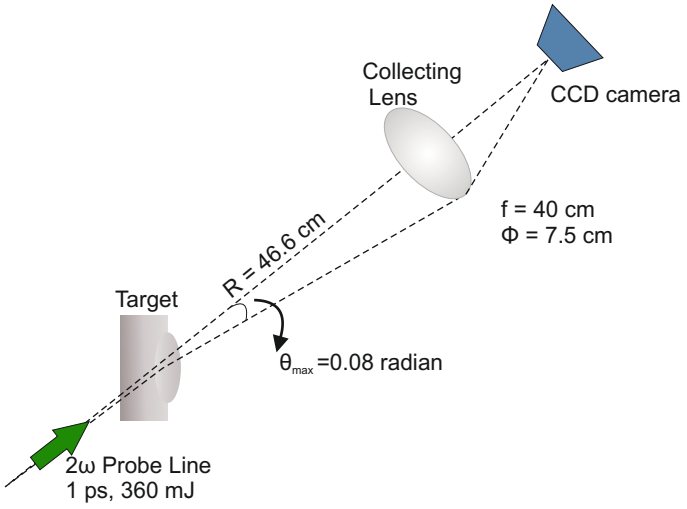

Figure 5.2: Optical probing shadowgraphy experimental set up. The probe line passes through a refracting plasma and images cannot be detected for more than the maximum refraction angle 0.08 radian determined by the lens.

5.3 Experimental Results

Figure 5.3 and 5.4 show the unprocessed signal of the electron energy spectra obtained during the experiment. The big bright spot marked on the axis is caused by energetic protons. If we magnify this region (within the white circle on figure 5.3), there is another bright spot marked on the axis caused by x-rays produced during the interaction which pass through the spectrometer collimator. The mid-point of this x-ray beam is accepted as the position of infinite electron energy and used to calculate the electron energy dispersion.

A clear signal stripe is seen on the right side of the central axis due to electrons which have been deflected by the magnetic field. The marked area within the dashed line on figure 5.3 is integrated vertically in order to produce an electron energy spectrum (see figure 5.5 and 5.8).

Figure 5.5 shows the QL signal obtained from the image plates (see section 4.2.4). The analysis of the electron spectrum is made after converting the recorded signal from QL to PSL numbers (see section 4.2.4). Figure 5.6 shows the recorded electron signal after converting QL numbers to PSL numbers. PSL numbers can be further converted to the number of electrons (see section 4.2.4).

Background noise was removed from the image plate images by subtracting the average of the exposure above and below the electron signal exposure. There are very small localised exposures in the image plates arising due to hard x-ray photon exposure. This noise can be removed by applying a Gaussian filter which works by replacing the data at pixel i with the average of the data from pixels i-N to i+N where $N = 3$. Each pixel has a size 25 μm. This filter was applied to the image plate signal and background data at each pixel on the image plate

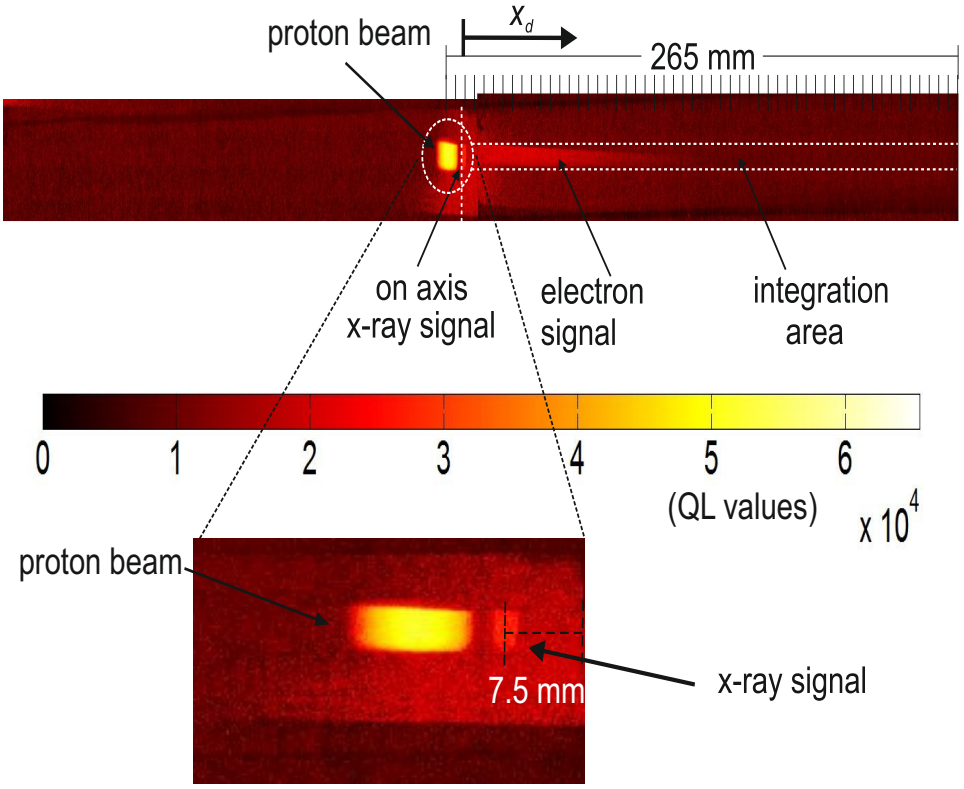

Figure 5.3: An example of an image plate image showing detected electron signals (with a scale length of 11.1 μm.) The centre of the bright spot shows the deposited energy due to x-rays. The electron signal is on the right hand side. On the distance scaling each grid point corresponds to 5 mm distance.

and reduced signal variability (PSL counts) by a small amount.

Figure 5.4 shows some of the original data which was taken during the experiment. For figure 5.4 a) to e), the pre formed scale length of the plasma decreases and it can be clearly seen that the number of hot electrons decreases with decreasing plasma scale length.

Figure 5.6 shows the recorded electron signal as a function of x_d dispersion distance before and after this localised noise processing. The black circles represents the signal before filtering while red circles represent the signal after the

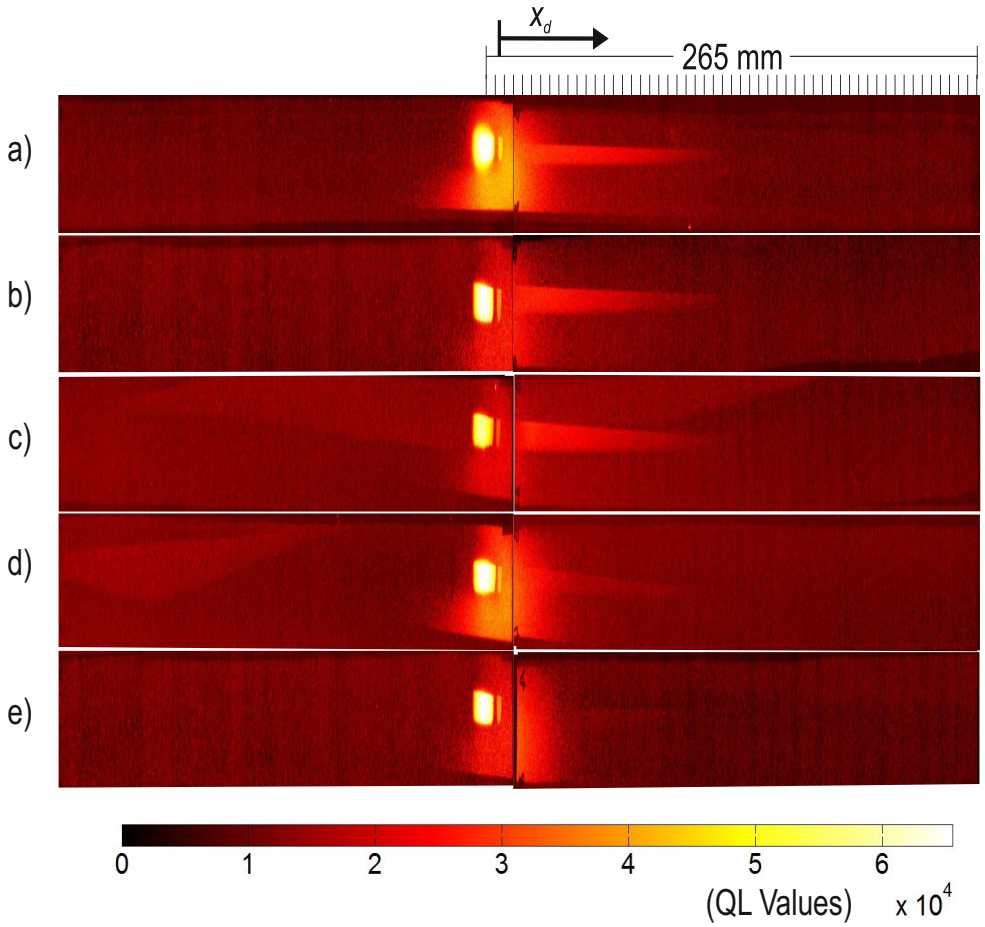

Figure 5.4: Some examples of image plates images showing recorded electron signals with different measured plasma scale lengths a) 9 μm, b) 8 μm, c) 7.2 μm, d) 4.6 μm e)1.2 μm. On the distance scaling each grid point corresponds to 5 mm distance.

signal smoothing process.

Figure 5.7 shows the recorded signal (red circles) and background noise (black circles) from the image plates. This data allowed the subtracting of the background noise as a function of dispersion distance x_d (see figure 5.8). The recorded electron signal starts at $x_d = 10$ mm and exposure could not be detected for $x_d > 90$ mm.

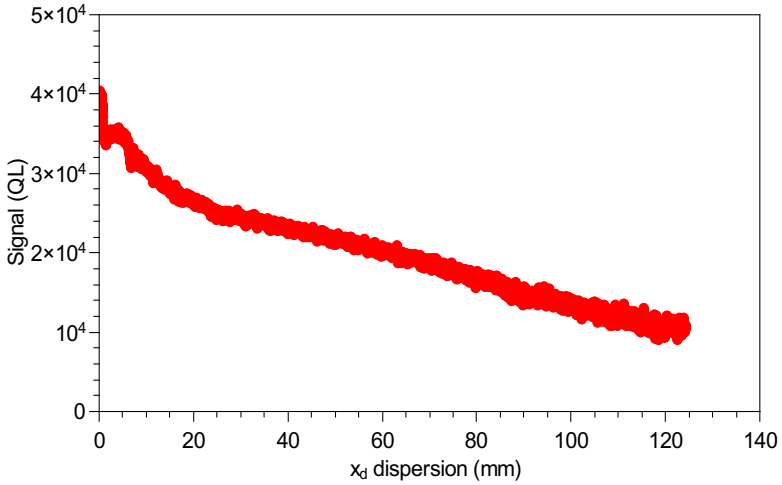

Figure 5.5: Recorded electron signal (QL values) on an image plate as a function of dispersion distance.

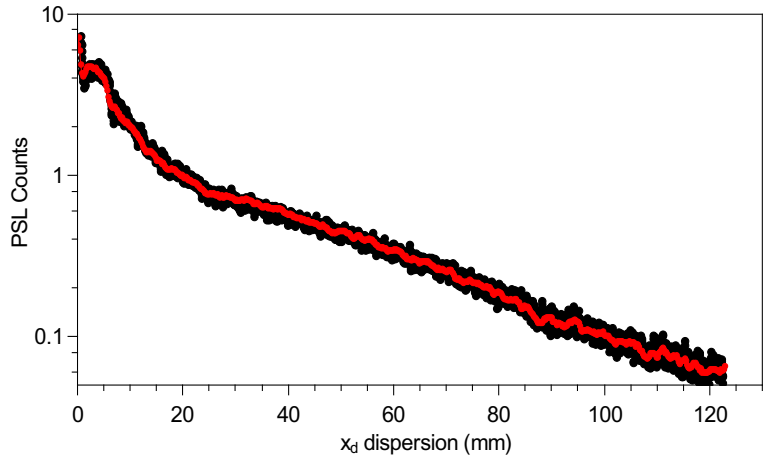

Figure 5.6: Recorded electron signal (PSL values) on an image plate as a function of dispersion distance. Black circles represents the data points before filtering and red circles represents the data after filtering.

The calculation of the corresponding electron energy per dispersion distance has been discussed in section 4.2.1. Using the relationship between energy and distance dispersion (equation 4.16), electron energies can be calculated for each dispersion distance. Figure 5.9 shows a further analysis of data similar to figure

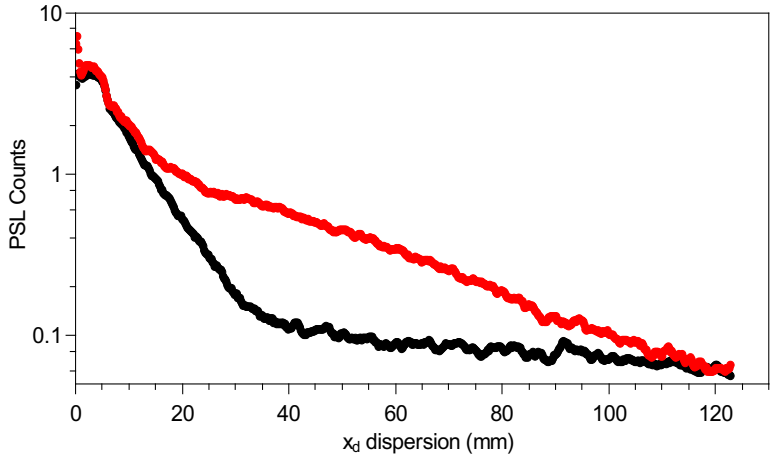

Figure 5.7: Recorded electron signal and background of signal (PSL values) on an image plate as a function of dispersion distance. Black circles represents the background noise and red circles represents the data points.

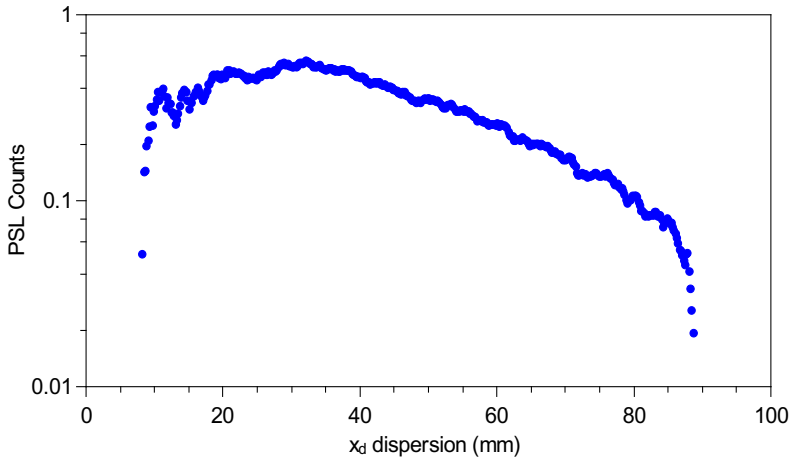

Figure 5.8: Recorded electron signal converted to PSL numbers as a function of x_d dispersion distance. The background has been subtracted.

5.8 after the conversion of PSL numbers to the number of electrons per solid angle and deduction of corresponding energy levels from the dispersion distance.

Figure 5.9 a) to f) show typical energy spectra for different shots. The electron numbers and energies show a large error for the highest energies as the

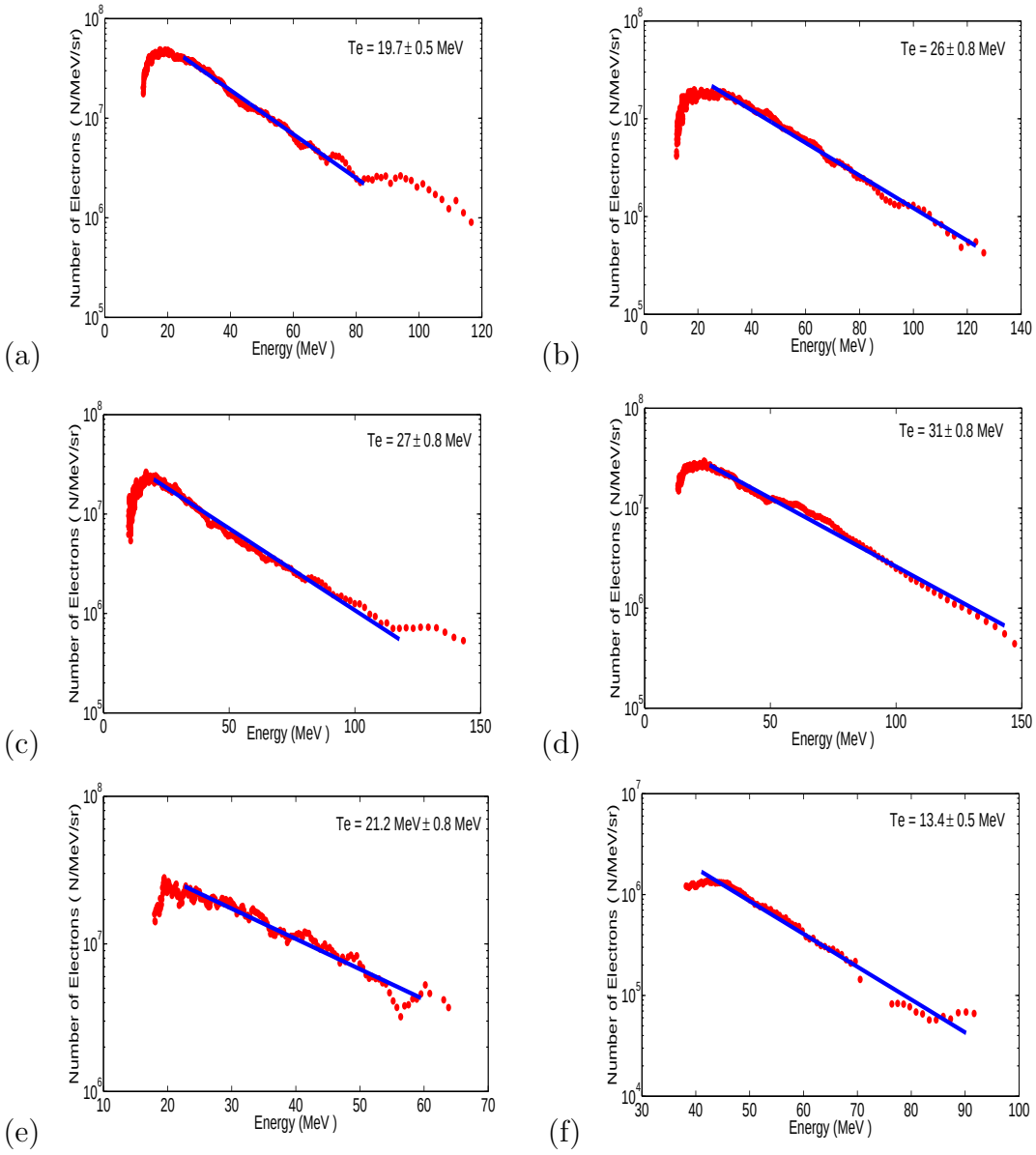

Figure 5.9: Samples of electron energy spectrum for a) 11.1 μm b) 9 μm c) 8 μm d) 7.2 μm e) 4.6 μm and f) 1.2 μm scale length showing the exponential allowing determination of the hot electron temperatures.

uncertainty of the zero point has a greater relative error (see section 4.2). By fitting an exponential to the measured electron energy spectra (see figure 5.9) electron temperatures can be determined.

The total number N_T of hot electrons per sr are evaluated from the electron energy spectra using the number of electrons in MeV/sr extrapolated to zero energy ($n(0)$) and multiplying by the deduced hot electron temperature. We can write that;

$$N_T = \int_0^\infty n(0)\exp\left(\frac{-E}{kT_{hot}}\right) dE \quad = n(0)kT_{hot}. \tag{5.1}$$

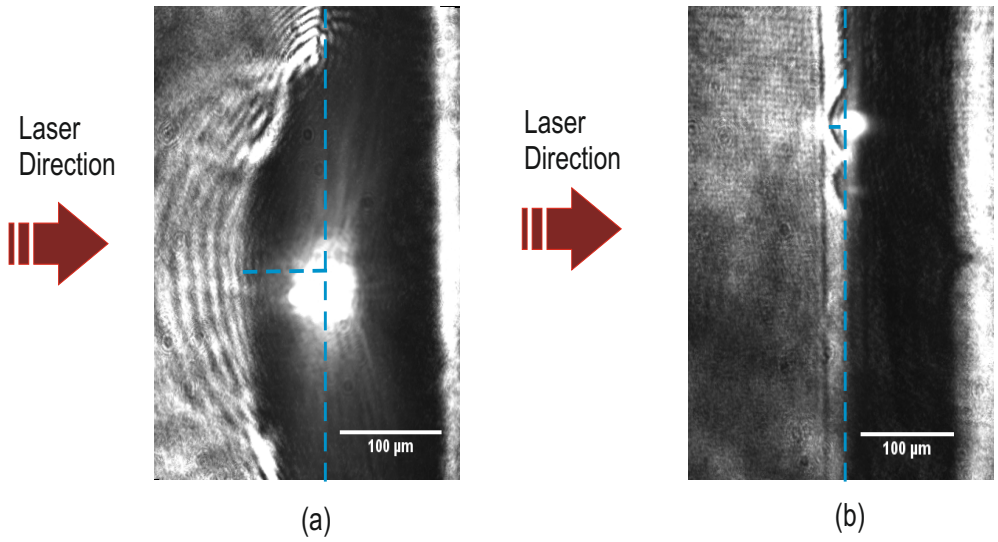

Figure 5.10: Optical probing shadowgraphy images (a) with (corresponding scale length is 5.5 μm) and (b) without prepulse (corresponding scale length is 1.2 μm). The broken line indicates the inital target surface. The bright central spot represents plasma self-emission and second harmonic production.

Measuring the extent of the region where $\theta > \theta_{max}$ from the shadowgrams, we

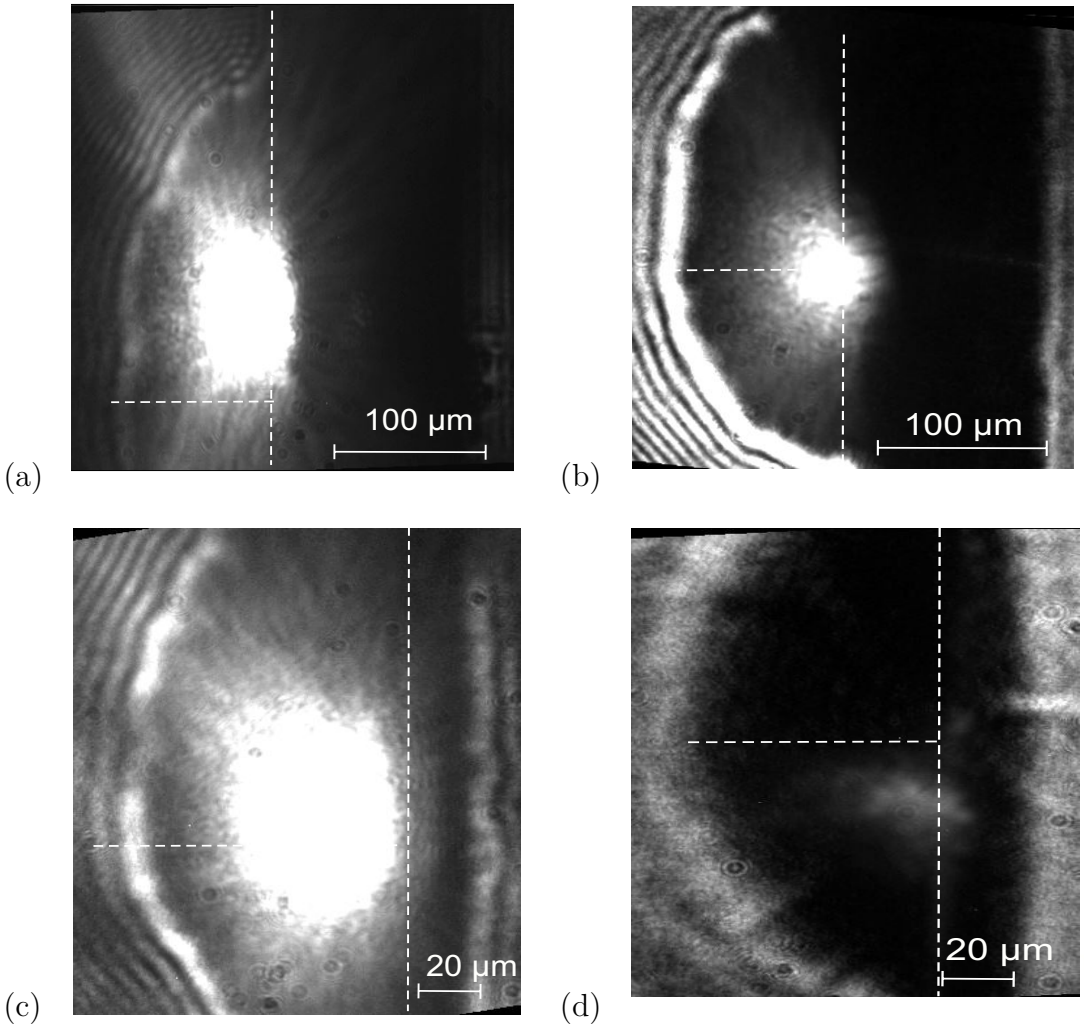

Figure 5.11: Sample shadowgraphy images for different scale lengths a) 11.1 μm b) 9 μm c) 7.2 μm d)6 μm. The vertical broken line indicates the initial target surface

have determined the density gradient,

$$\frac{dn_e(z)}{dz} = -\frac{n_e(z)}{L} = \left(\frac{\theta_{max}}{\Delta y}\right) 2n_c \tag{5.2}$$

as a function of distance z from the initial target surface. Figure 5.10 indicates the recorded shadowgraphy images with and without prepulse. The laser direction to the target is as it is shown on the figure 5.10 with red arrows and broken vertical lines indicates the initial target surface which is decided after checking the reference images taken before each shot (see figure 4.12). Figure 5.11 gives some examples of shadowgraphy images for different scale lengths.

Assuming the electron density at the original target surface is given by $n_s = Z^*(e/(m_p M))\rho$, where ρ is the solid target mass density, $Z^* \cong 6$ the average charge, M the atomic mass of the target and e, m_p the proton charge and mass, we can determine the density scale length L from the measurement of θ_{max} (see figure 5.12). Figure 5.12 shows that small variations of the pre-pulse irradiance arising due to variations of the incidence pre-pulse laser energy cause significant, but controllable changes in the plasma scale length. The scale length change is approximately linear over the range of pre pulse intensities considered, but increases approximately exponentially from the measured scale lengths for pre-pulse free irradiation.

We found that the number of hot electrons measured with the electron spectrometer increases with the plasma scale length measured by shadowgraphy (see figure 5.13).

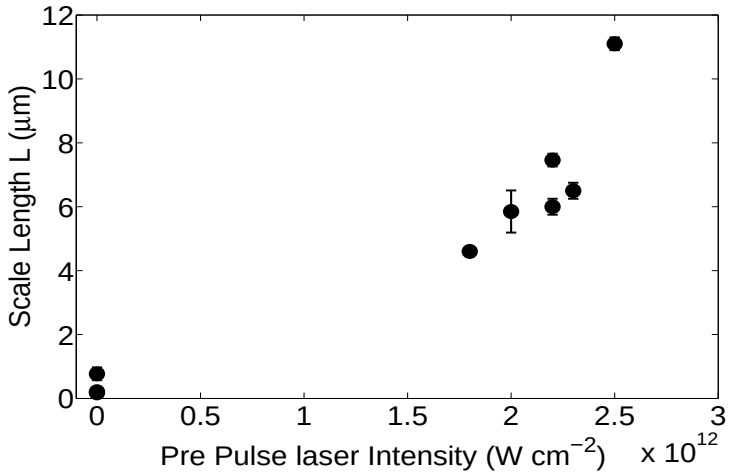

Figure 5.12: Density scale length measurement as a function of the pre-pulse laser intensity.

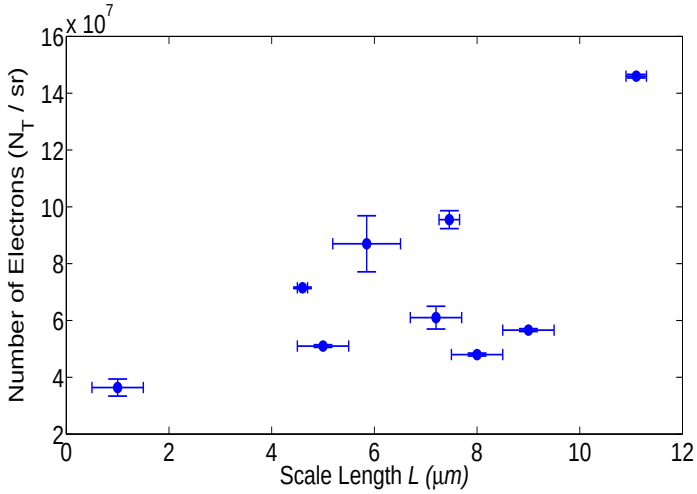

Figure 5.13: Number of measured hot electrons as a function of the measured plasma scale length.

5.4 ELPS PIC Code Simulations

The 1D code which was used in the presented work is known as the Entry Level PIC Simulation (ELPS) [78]. For the 1D code (ELPS), 7×10^5 spatial points were used with a cell size of 1×10^{-9} m. A 20 μm CH foil target with exponential

density profile and scale length L was varied from 1 to 11 μm. There were 10 particles of electron and ions in each cell. A Gaussian laser pulse shape was chosen with an intensity of 5×10^{20} W cm^{-2}. Laser wavelength and pulse duration were 1 μm and 1 ps, respectively.

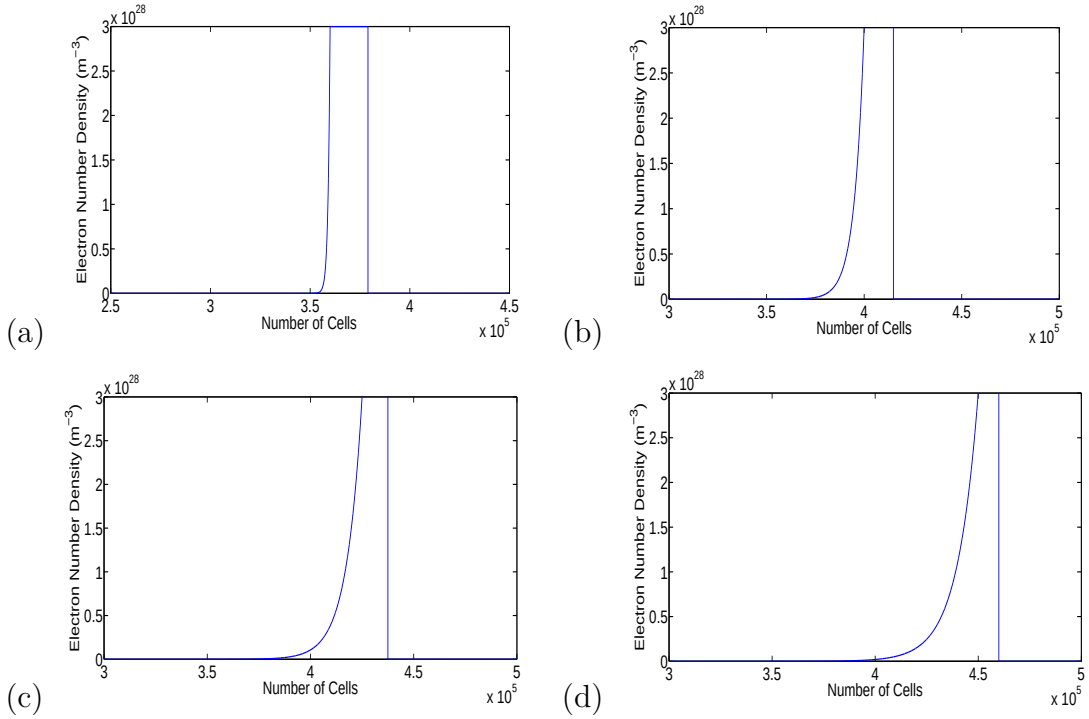

Figure 5.14: An example of electron density profiles with a) 1 μm , b) 5 μm, c) 7.5 μm and d) 10 μm scale length for ELPS PIC code simulations.

Figure 5.14 shows an example density profile set up for the simulations for 1, 5, 7.5 and 10 μm scale lengths. The slab thickness is a constant 20 μm with the scale length added in front of the main slab. The starting point of the density profile was kept constant at 350 μm.

For a 1 ps laser pulse, the electron phase space for different density profiles are shown in figure 5.15 for the output at 0.5 ps. It is clearly seen that additional scale length increases the number and energy of hot electrons.

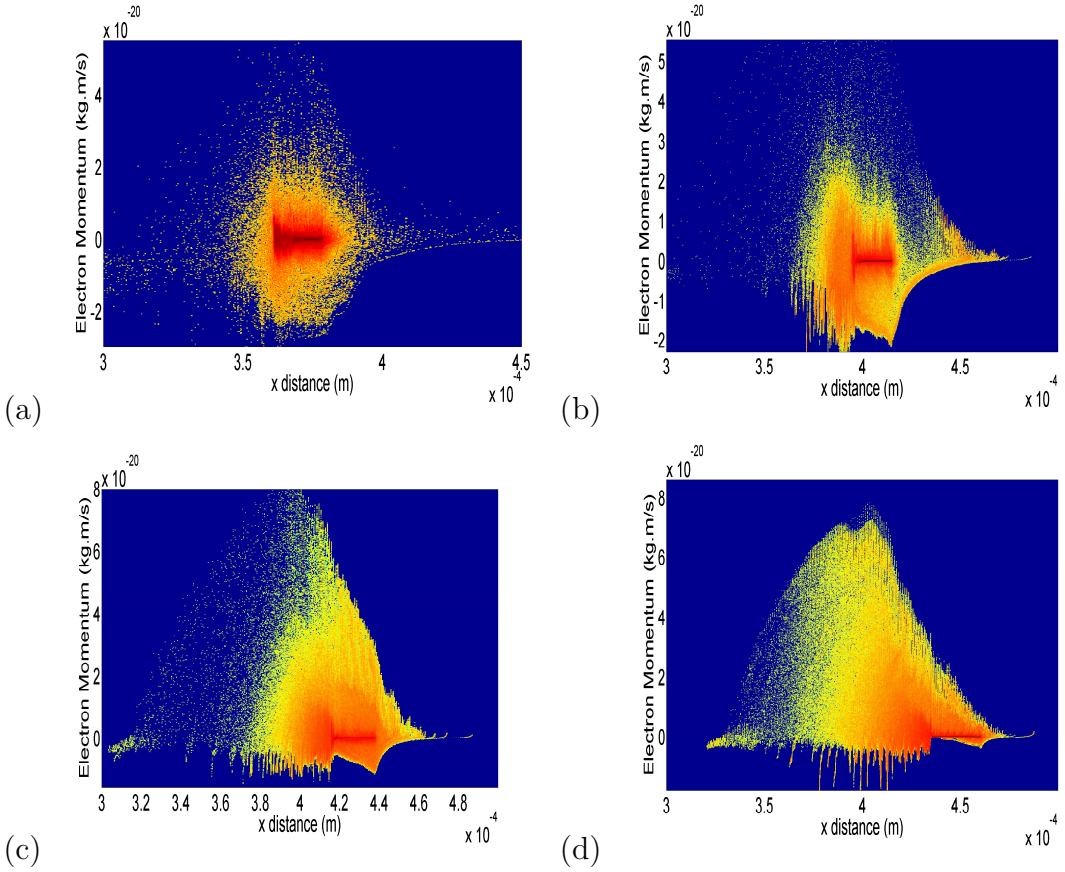

Figure 5.15: An example of the electron phase space after 0.5 ps with a) 1 μm , b) 5 μm, c) 7.5 μm and d) 10 μm scale length found using the ELPS PIC code simulations.

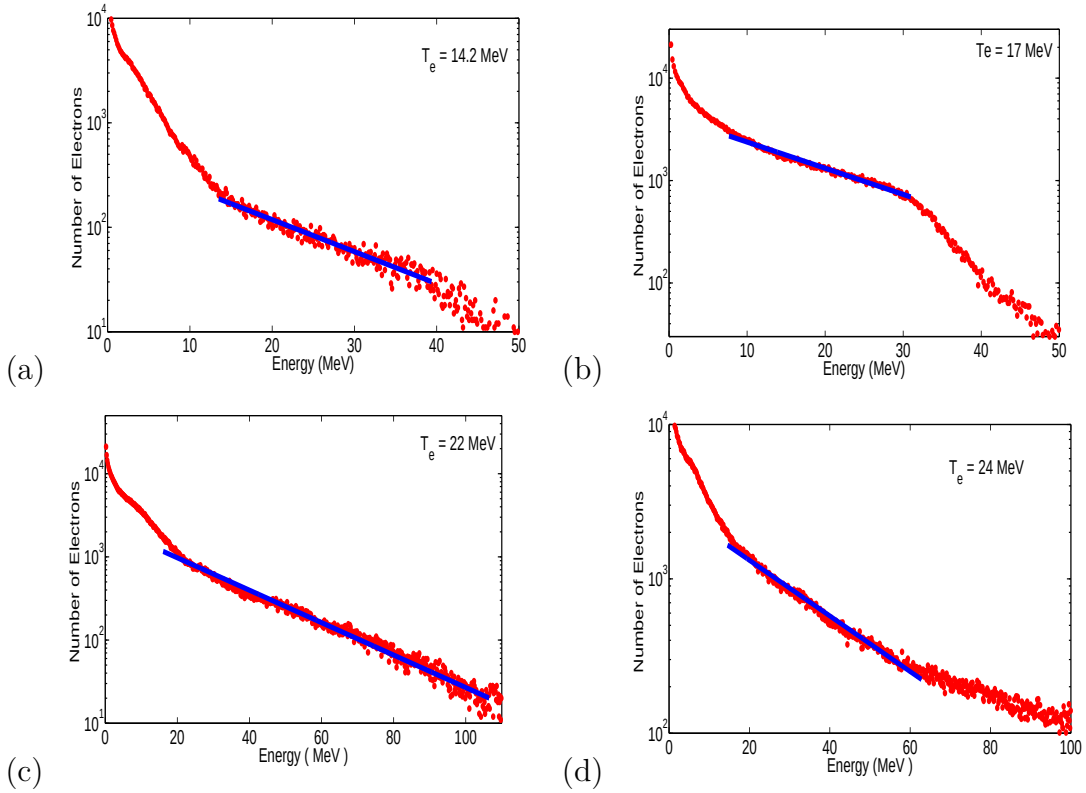

Figure 5.16: An example of electron energy spectra after 0.5 ps with a) 1 μm , b) 5 μm, c) 7.5 μm and d) 10 μm scale length for ELPS PIC code simulations.

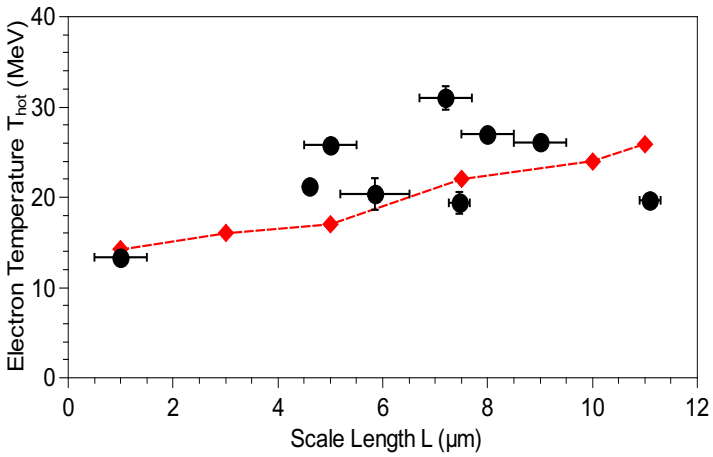

Figure 5.17: Experimental measurements of electron temperature as a function of the measured plasma scale length for a number of individual laser shots (circles). Superimposed are 1D (diamonds) PIC code simulations with the preformed scale length and following the experimental parameters.

The hot electron energy spectrum can be extracted from the simulation. Figure 5.16 shows the energy spectra for the four different density profiles plotted at figure 5.14. The electron energy spectra was extracted at 0.5 ps after the laser has delivered all of its energy to the electrons. Fitting the hot part of the spectrum gives the temperatures used to compare to the experimental results plotted on figure 5.17.

It is seen that our experimental measurements approximately follow the PIC code expectations. However, the experimental electron temperatures decreases at longer scale length ($L > 7.5\,\mu$m) which is not seen in the 1D PIC code simulations (see figure 5.17).

The simulation code shows that the fractional absorption of the main laser pulse increases with the density scale length. As expected the increased absorption produces a larger number of hot electrons with increasing scale length as observed

(figure 5.13). At longer scale lengths, the PIC simulations also show that the laser light is largely absorbed and not significantly reflected at the critical density. However, it is clear that the 1D simulation code does not accurately predict more the measured electron temperatures at longer scale length ($L > 7.5\,\mu$m). It is possible that laser self-focussing or filamentation creating lower temperature hot electrons occurs with longer scale length plasmas which would need to be simulated with a 2D code.

5.5 EPOCH 2D PIC Code Simulations

Since the 1D code was not able to explain our experimental results, a 2D PIC code EPOCH [77] was used to simulate the experimental electron temperatures. For the 2D code, the system size was 90 μm $\times$ 90 μm with a mesh resolution of 1500 $\times$ 1500 cells. For the simulation 16 particles of electrons and protons were used in a cell. The experimental variation of electron temperatures for different scale lengths with the laser irradiance of $5 \times 10^{20}\,\mathrm{W\,cm^{-2}}$ focussed on a 7 μm focal spot with an incidence angle of 40° degrees was determined. The laser wavelength and pulse duration were 1μm and 1 ps, respectively.

In the simulations, the peak electron density was limited at 100 n_c where n_c is the critical density. An exponential density profile was assumed with varying scale lengths L from 1 μm to 11 μm with a out off to zero density at 0.01 n_c.

Figure 5.18 shows the laser electric field profile predicted by the PIC code simulation after 0.5 ps with a) 5 μm , b) 11 μm scale length. It is seen that for the 5 μm scale length, the laser is reflected at the critical density (see figure 5.18 a) which explains why the hot electron temperature increases for shorter scale

lengths ($L < 7.5\mu$m). At longer scale lengths ($L > 7.5\mu$m), the laser energy is absorbed before the critical density which explains why the electron temperature decreases with longer scale lengths ($L > 7.5\mu$m). The increasing scale length also causes laser filamentation (see figure 5.18 b) inside the plasma and increases the number of accelerated electrons with lower temperatures in agreement with our experimental observations.

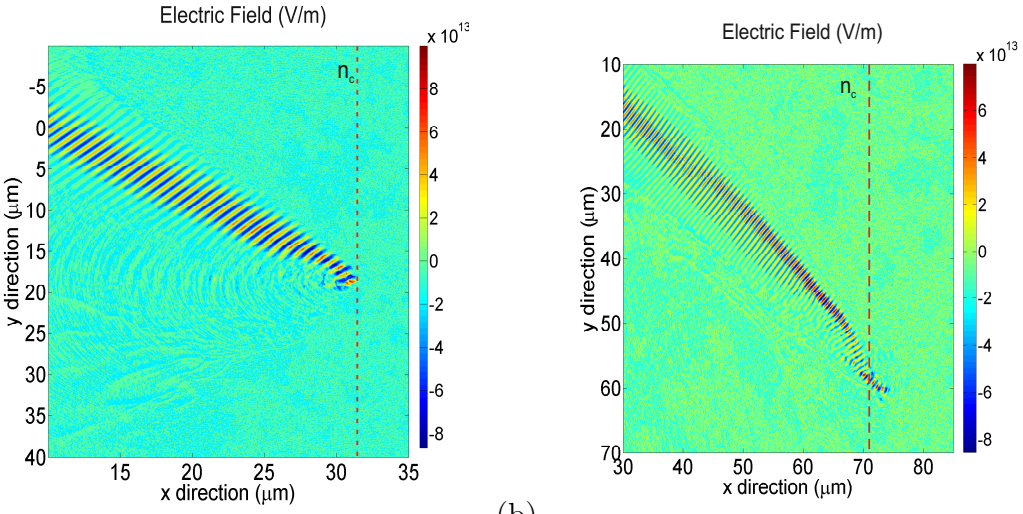

(a) (b)

Figure 5.18: An example of laser electric field profile after 0.5 ps with a) 5 μm , b) 11 μm scale length in the EPOCH 2D PIC code simulations.

The hot electron energy spectrum can be extracted from the simulation as we did for the 1D code. Figure 5.19 shows the energy spectra for the two different density profiles with the scale length L of a) 6 μm and b) 9 μm. The electron energy spectra was extracted at 0.5 ps after the laser has delivered all of its energy to the electrons. Fitting the hot part of the spectrum gives the temperatures used to compare to the experimental results plotted on figure 5.21.

Figure 5.20 compares the generated electron spectra from the 2D PIC code to

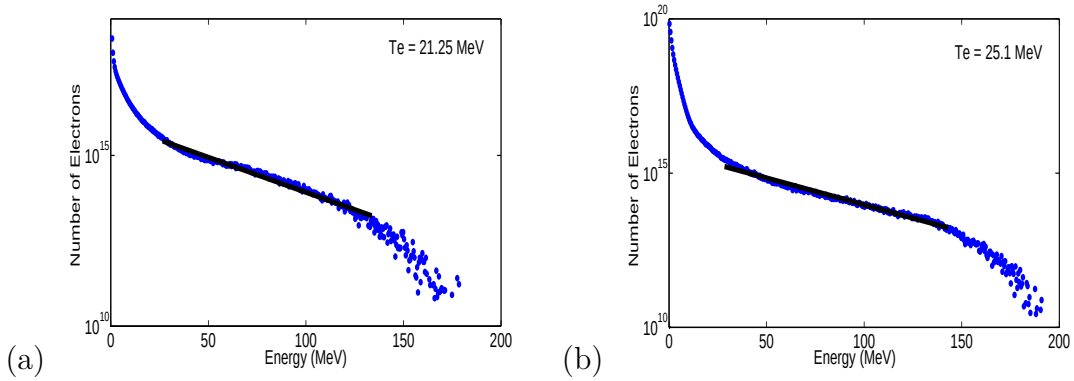

Figure 5.19: An example of exponentially fitted electron energy spectra after 0.5 ps with a) 6 μm , b) 9 μm scale length for EPOCH 2D PIC code simulations.

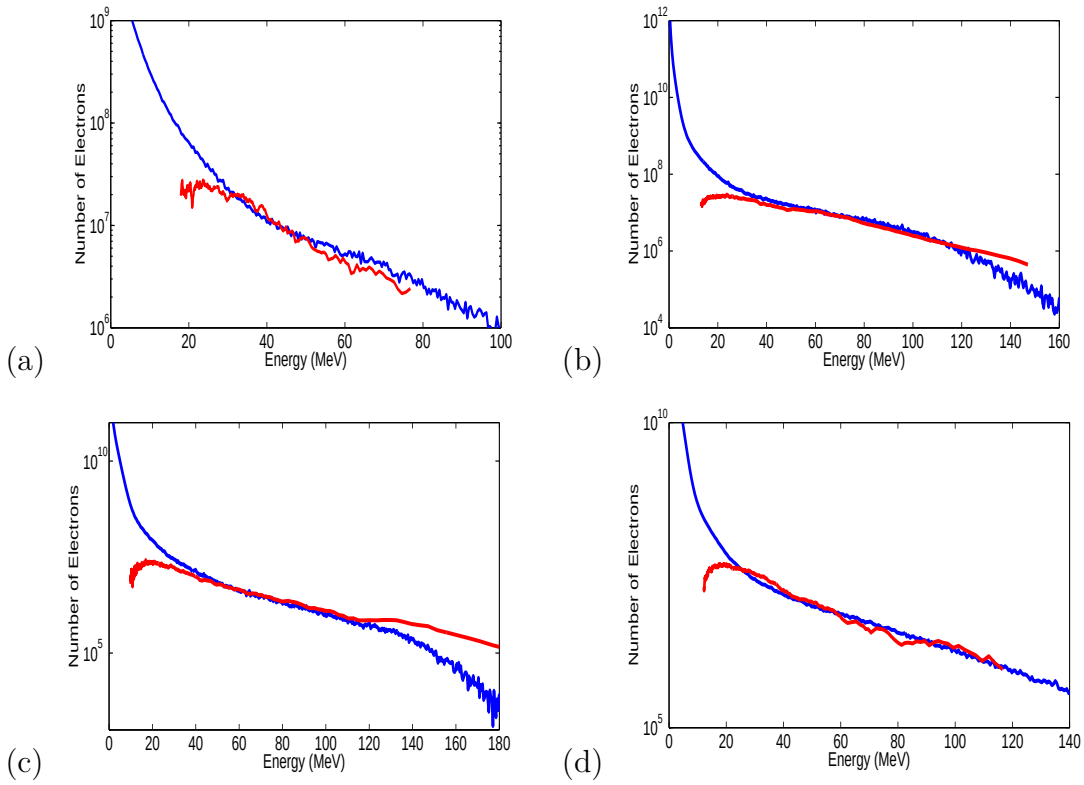

Figure 5.20: Comparison of EPOCH 2D PIC code results with experimental electron spectra for a) 6 μm , b) 7.5 μm c) 9 μm and d) 11 μm scale length. The red line represents the experimental data, the blue line is the simulation. The vertical scales are arbitrary and the spectrum are visually superimposed.

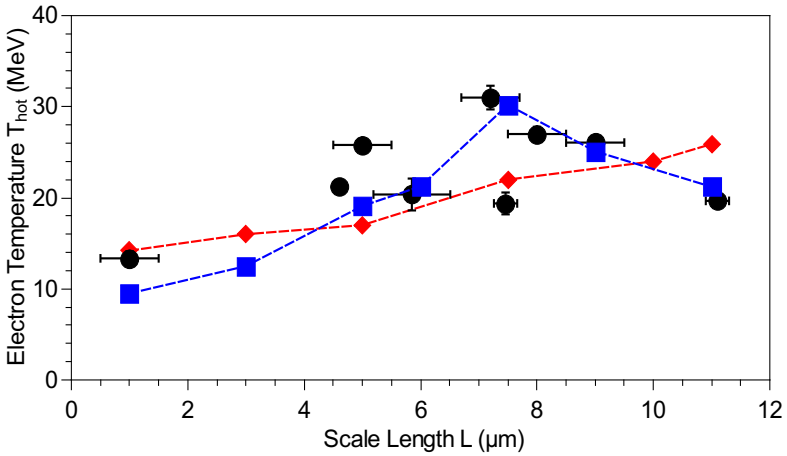

Figure 5.21: Experimental measurements of electron temperature as a function of the measured plasma scale length for a number of individual laser shots (black circles). Superimposed are 1D (red diamonds) and 2D (blue squares) PIC code simulations with the preformed scale length and following experimental parameters.

the experimental electron spectra for different scale lengths. Blue lines represent the EPOCH 2D PIC code simulation results and red line shows our experimental observations. It is seen that our experimental measurements are closely following the PIC code expectations.

Figure 5.21 summarises the results presented in this chapter for the electron temperature as a function of generated scale length. Experimental observations are shown with black circles, 1D PIC code results are presented by red diamonds and 2D PIC simulations are given by blue squares. It is clearly seen that 2D PIC code simulations are in good agreement with our experimental observations.

5.6 Conclusion

Hot electron temperatures up to 20-30 MeV have been produced by picosecond duration laser pulses focussed to intensities of $\sim 10^{20}$ W cm^{-2} with a deliberate pre-pulse on solid targets. We have presented the measurements of the number and temperature of hot electrons obtained using an electron spectrometer. The results have been correlated to the density scale length of the plasma produced by the controlled pre-pulse measured using an optical probe diagnostic. 1D PIC simulations predict electron temperature variations with plasma density scale length in approximate agreement with the experiment at shorter scale lengths ($< 7.5\,\mu$m), but were not able to predict electron temperatures at longer scale lengths. Experimentally observed electron temperatures decreased for longer scale lengths as predicted by a 2D PIC code. The agreement of the experimental and 2D simulation results at longer scale length shows that two dimensional effect are affecting the temperatures as observed by a report in a recent paper [131].

Chapter 6

Measuring Hot Electron Temperatures with an X-Ray Diode Array

6.1 Introduction

Hot electrons generated from the interaction of ultra intense laser pulses and solid density plasma have been of interest in recent years because of applications to various fields of research, such as fusion fast ignition [5, 6, 132], particle acceleration [17, 18, 53] and ultra fast x-ray source development [133, 134]. As the number and temperature of hot electrons have a strong dependence on laser intensity and other conditions such as the level of laser pre-pulse (see chapter 2), the generation of hot electrons with different laser parameters have been investigated by many research groups [9, 41, 44, 45, 135–137] (see chapter 5).

In this chapter, we have used moderate intensities ($\sim 10^{16}$ W cm^{-2}) and ultra-

short laser pulses (fs) to investigate hot electron generation. A pre-pulse, which is 10 % of the main pulse ($\sim 10^{15}$ W cm^{-2}), has been used to generate pre-plasma.

Several mechanisms that can transfer laser energy to hot electrons have been proposed such as $\mathbf{J} \times \mathbf{B}$, resonance absorption, vacuum heating, parametric instabilities (see chapter 2). These laser absorption mechanisms have strong dependences on laser intensity and plasma scale lengths. For moderate laser intensities, for example, resonance absorption varies strongly with scale length [138].

In our research, a pre-pulse duration the same as the main pulse (35 fs) with energy contrast 10 times lower than the main pulse was employed. The main 35 fs pulse interacts with a plasma of scale length 0.65 μm produced from the pre-pulse. This experimental arrangement allows resonance absorption to occur from the main pulse with a controlled plasma scale length which is not modified during the absorption process. In many experiments on resonance absorption the density profile of the plasma is modified during the absorption by, for example, profile steepening [31, 139].

Hot electrons temperatures as a function of the incident laser angle have been investigated theoretically using EPOCH 2D PIC simulations. The electron temperatures vary with the incident laser of incidence angles and with the plasma scale length in approximate agreement with experiment.

The role of the hot electrons produced by resonance absorption in heating a solid target during laser irradiation has been investigated. It is possible that hot electrons can pre heat a solid target and change the thermal transport into the target making energy transport have a highly non-linear behaviour. Experiments were undertaken with buried layer targets comprising a thin layer of iron (50 nm) buried in parylene-N (CH) plastic (substrate 200 nm thick, overlay on the laser

side 50 nm thick). Hot electrons and radiation from the laser interaction can heat the iron layer which ionises. Calculations show that if iron is heated so that Fe^{5+} ions are created, the iron layer becomes transparent to probing 59 eV photons produced by laser interaction in another plasma irradiated on a line focus [140]. The role of hot electrons and other target heating mechanisms such as radiation and thermal transport can then be evaluated.

Our experiment was undertaken at the LASERIX facility (in the Ecole Polytechnique campus). LASERIX comprises a 100 TW-class infrared laser (IR) and a laser-pumped extreme ultra-violet (EUV) laser usually operating at 13.9 nm. The infra-red laser ($\lambda = 800$ nm) delivers 20 mJ energy in 35 fs and can be focussed to a 25 μm radius enabling a laser intensity of $\sim 10^{16}$ W cm^{-2}. This type of laser can produce relatively fast electrons (> 10 keV) which heat the target [137, 141]. Our experimental results show that hot electron temperature measurements are in agreement with Beg's Scaling which gives $T_{hot} \simeq 60$ keV for 30° incidence angle (see section 2.3.2).

Bremsstrahlung hard x-ray spectrum arises from the Maxwellian distribution of electrons accelerating in the electric field of ions. The shape and intensity of bremsstrahlung is related to the hot electron distribution with a Maxwellian electron distribution producing an exponential drop of emission ε with photon energy $h\nu$ such that $\varepsilon \propto \exp(-h\nu/kT)$ [141]. In our experiment, x-ray diodes were used to measure the hot electron temperature using x-rays created by bremsstrahlung emission. The x-ray relative flux was also recorded with the diodes.

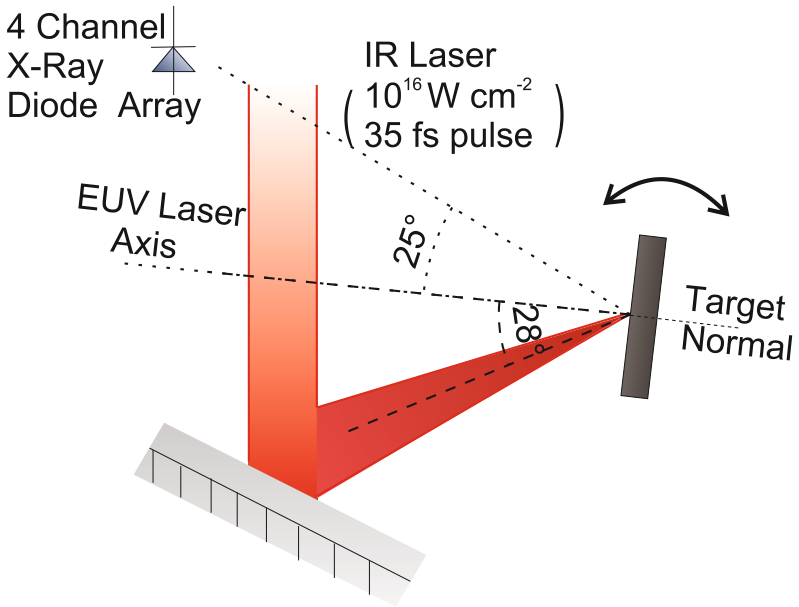

Figure 6.1: Experimental layout in the LASERIX facility. The target is rotated to alter the angle of laser incidence.

6.2 Experimental Design

The infra-red laser at the LASERIX facility delivered 0.8 μm wavelength laser pulses of 35 fs duration and shot energies 4-21 mJ with a contrast of 10^9. These pulses were focussed using an f/8 parabolic mirror to a 50 μm (FWHM) spot. A peak intensity of 3×10^{16} W cm^{-2} in a p-polarized beam with varying incident angles from 3° to 53° degrees to the target normal was produced. 10 % of the main pulse energy was taken to pre heat the target at a time 20 ps before the main pulse with a similar pulse. Plain foil targets of CH in various thicknesses from 200 nm to 650 nm were used. The targets contained a thin (50 nm) layer of iron under 50 nm of CH overlay on the laser interaction side.

Figure 6.1 shows the experimental layout of the target chamber and the diode

array. The x-ray diode array was positioned inside the target chamber with a 25° angle to the target normal facing the front side of the target as shown in figure 6.1. Short co-axial cables were used to connect BNC feedthroughs to external amplification circuity. Since random electronic noise can be picked up and amplified by the circuitry, short cables were used with the diodes isolated from one another to eliminate capacitive coupling. After amplification, oscilloscopes were used to record the signals from the diodes. The X-ray diodes were filtered using selected filters to cover different spectral ranges as described in section 4.4.

6.3 Experimental Results

With x-ray diodes, very low radiation levels in different regions of the spectrum can be detected and amplified. The hot electron temperature is determined using the signal ratios between different channels separately filtered to cover different spectral ranges (see section 4.4.2). Calibration shots to a 100 μm Al target at various incident angles of the laser pulse were taken with the same filtering on each channel (75 μm Al). Calibration coefficients were obtained as a function of angle for the response of the different channels and used to normalise the diode response when different filters were employed for each diode. Figure 6.2 shows the recorded signal taken from the 4 different diodes with the same filter (75 μm Al) at the same time. There are slight differences in the captured signal from each diode. The calibration of the different diodes was done by adjusting the least noisy part of the diode time trace for each signal to get the same response from all diodes. Figure 6.2 a) shows the initial recorded signal and figure 6.2 b) shows the same signals after this calibration adjustment. Calibration shots were taken

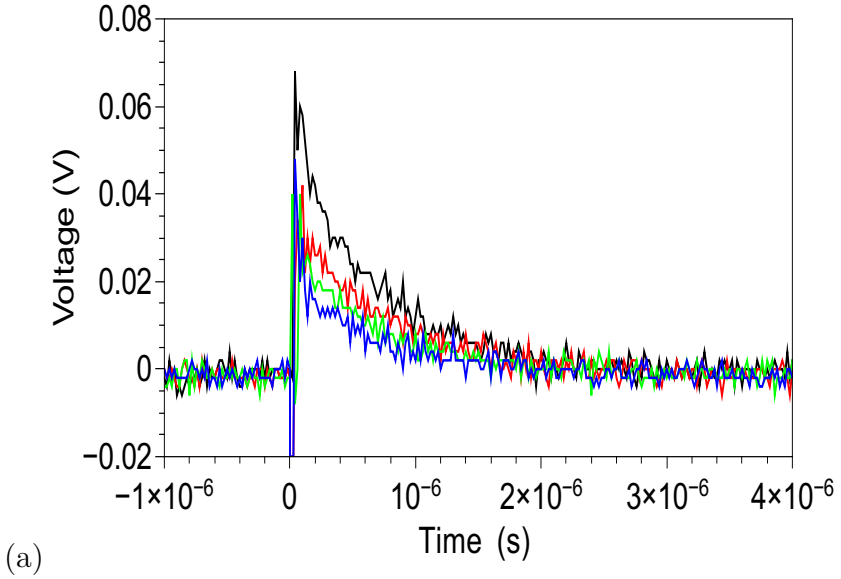

(a)

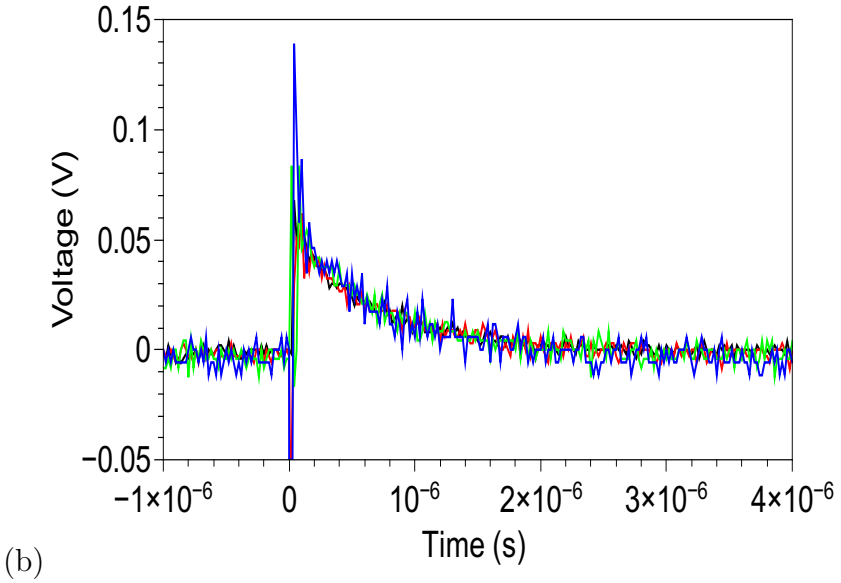

(b)

Figure 6.2: a) Recorded diode signals before adjustment for the diode relative calibrations at 8° incident angle and 9 mJ energy on an aluminium target, b)The same diode signals after the relative calibration between the diodes have been taken into account. The diodes were all filtered with 75 μm of Al.

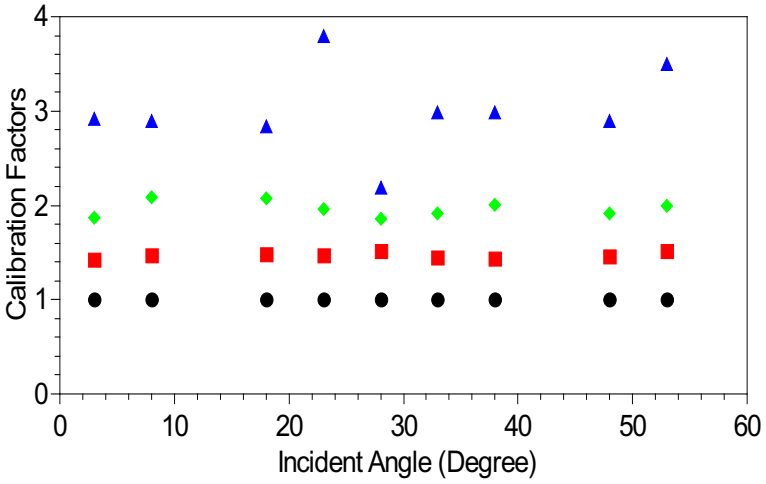

Figure 6.3: Calibrations factors as a function of incident laser angle. Blue triangles(▲) represents channel 1 , green diamonds (◆) represents channel 2, red squares (■) represents channel 3 and black circles (●) represents channel 4 (see section 4.4.2).

for different laser incident angles (figure 6.3). There was no significant variation of the calibration with the laser angle of incidence.

Figure 6.4 shows some samples of recorded signals by diodes for different laser incident angles onto targets of plastic with a buried layer of iron. In order to extract temperatures from the ratio of the recorded diode signals, the diode signals were integrated from 0.2 μs to 2 μs where there is less noise (see section 4.4.2). Following the integration of each recorded signal, extracted values from integrations were divided to each other such as channel 1 / channel 3. These ratios were used to extract the temperatures from the signal ratios (see figure 4.17). The signal recorded for channel 2 (150 μm Al filter) is higher than for channel 1 (75 μm Al filter) which was not expected. This may be associated with Fe K_α at 6.4 keV emission, so for the deduction in temperature, channel 2 was not used. For the temperatures of hot electrons and recorded signals by diodes,

the error bars were calculated from the standard deviation of different recorded shots for each angle.

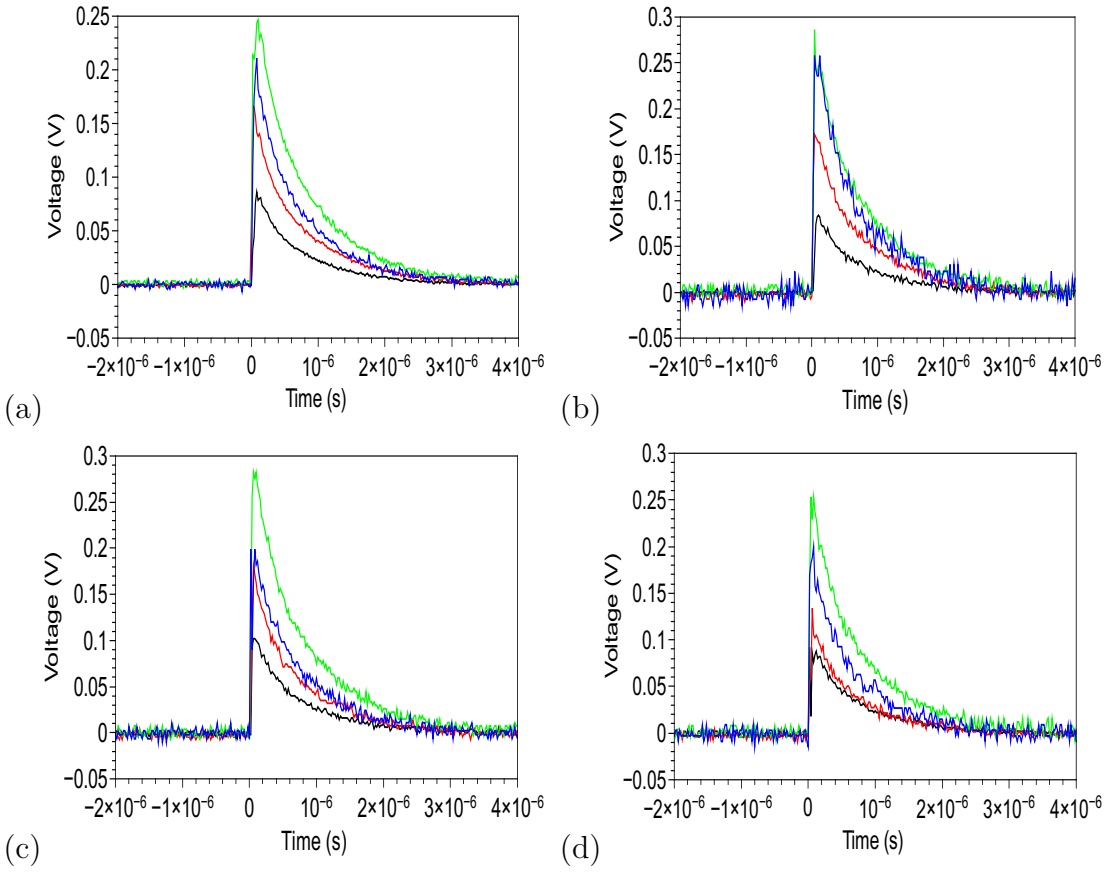

Figure 6.4: Recorded diode signals with a) 18° b) 23° c) 28° and d) 38° incident angles and 21 mJ energy on targets. Blue line represents channel 1 , green line is for channel 2, red line is for channel 3 and black line represents channel 4 (see section 4.4.2 for the filtering employed).

The measured electron temperature as a function of incident angle is given in figure 6.5. These temperatures are extracted from the ratio of channel 1 and channel 3 (see section 4.4.2). It is seen that hot electron temperatures reaches peak point at 28°. Previous theoretical researches show that the angle which gives the maximum temperature, depends on the generated plasma scale length [142]

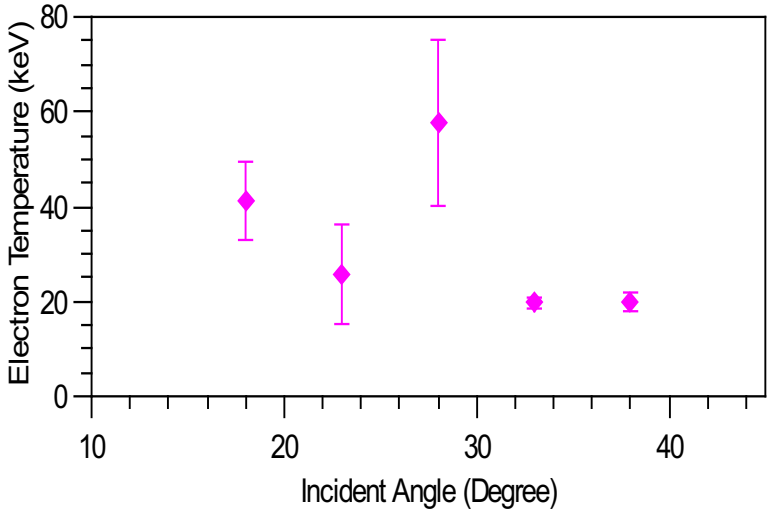

Figure 6.5: Experimentally measured electron temperature results are shown as a function of incidence angle.

due to the resonance absorption effect in moderate laser intensities.

Figure 6.6 shows the measured flux of x-rays of energy greater than approximately 5 keV or 20 keV as a function of laser incident angle measured using diodes 1 and 4. The efficiency of producing x-rays peaks at angles of incident $\simeq 30°$. The results, shown in figure 6.6, are typical of resonant absorption with a maximum yield occurring at a $\approx 30°$ incidence angle. Using the standard approximations for the scale length of optimum resonant absorption the plasma scale length L can be estimated. This scale length is $L \approx (c/\omega)(0.8/\sin\theta)^3$ where ω is the laser frequency, θ is maximum angle of absorption. The peak resonance absorption at $30°$ (see figure 6.6) corresponds to a plasma scale length of $\sim 0.55\,\mu$m.

Density profiles of the target can be investigated by using HYADES simulations for different incidence angles (supplied by L.A. Wilson). The HYADES fluid code density profile 20 ps after irradiation by a pre-pulse was used (see figure 6.7).

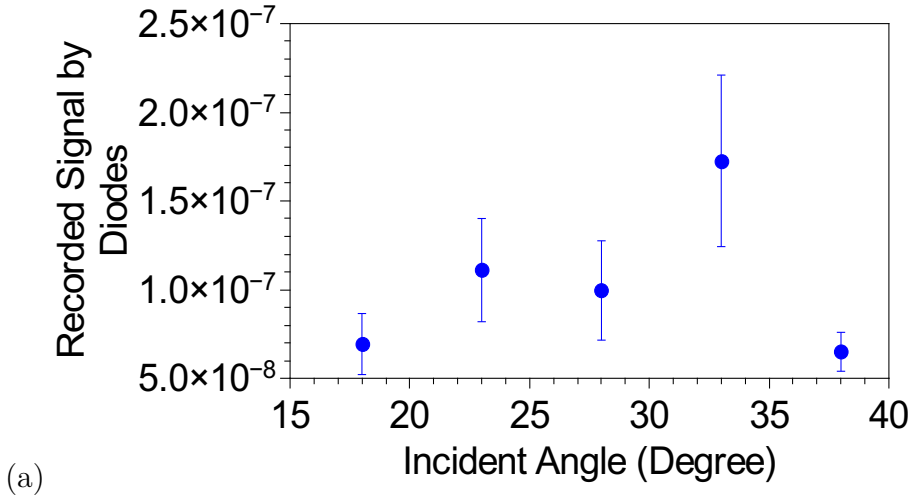

(a)

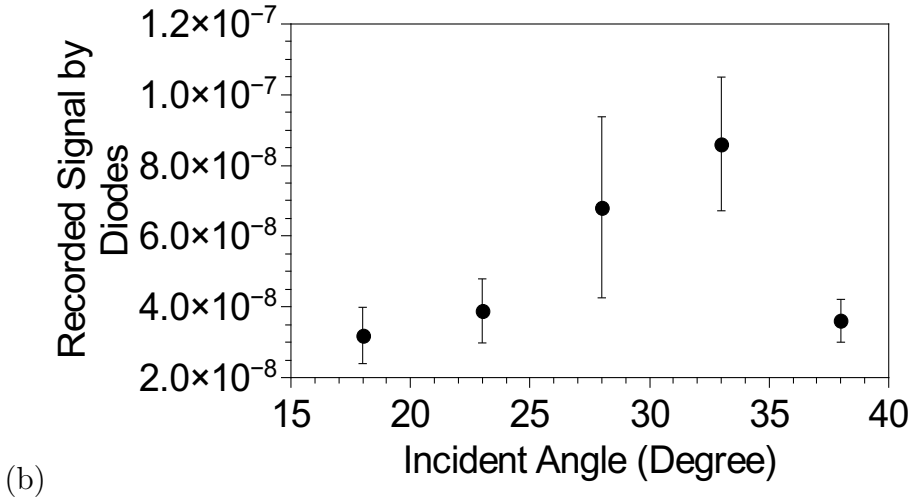

(b)

Figure 6.6: The measured flux of x-rays at energies greater than 5 keV for the LASERIX experiment as a function of incidence of the heating laser pulse of irradiance 3×10^{16} W cm^{-2} and pulse duration 35 fs. a) channel 1 recording photons of energy > 5 keV and b) channel 4 recording photons of energy > 20 keV.

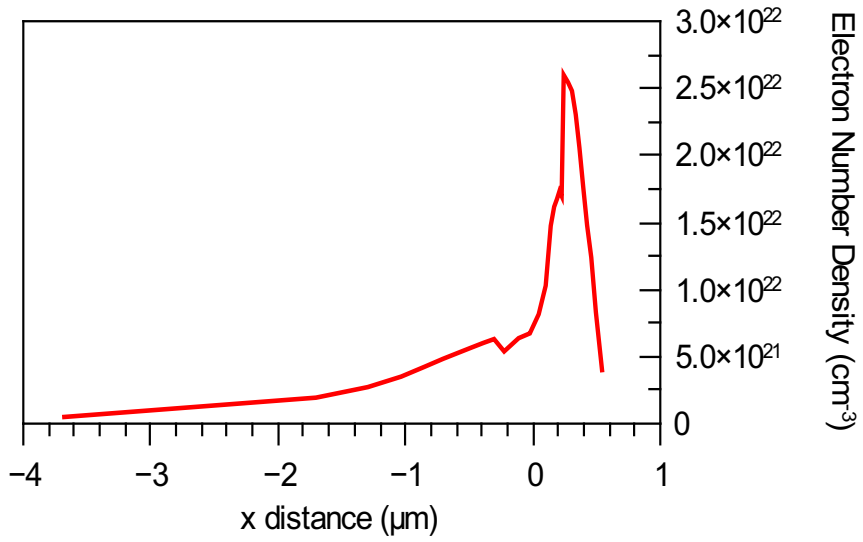

Figure 6.7: Expected electron density profile simulated by the HYADES fluid code generated by a deliberate pre-pulse (3×10^{15} W cm^{-2}) before the main pulse at 20 ps.

Figure 6.7 shows the electron density profile for 300 nm buried plastic target. 100 nm Fe buried 100 nm below the laser irradiated surface. Target was irradiated by a laser with an intensity of 3×10^{15} W cm^{-2} and 28° degree of incident angle. The scale length L has been deduced at the critical electron density by fitting $n_e = n_c \exp(-x/L)$ where n_c is the initial electron density and x is the distance from the target. By fitting the density profile to the HYADES fluid code output, a scale length $L \cong 0.65$ μm was obtained in approximate agreement with the scale length $L = 0.55$ μm deduced from the resonance absorption optimum angle measurement.

6.4 EPOCH Simulations

Simulations were undertaken using the 2D PIC code EPOCH (see section 2.6.1). Experimental parameters were chosen to simulate the hot electron generation with a laser of 0.8 μm wavelength and 35 fs pulse length and irradiance of 3×10^{16} W cm^{-2}. A Gaussian laser pulse variation in time was assumed. In the experiment, there was a deliberate pre pulse of 10% (3×10^{15} W cm^{-2}) of the main pulse with a 20 ps time delay which generated the pre-plasma. The interactions of the laser with the pre-plasma was simulated by assuming an initial exponential density ramp of specified scale length.

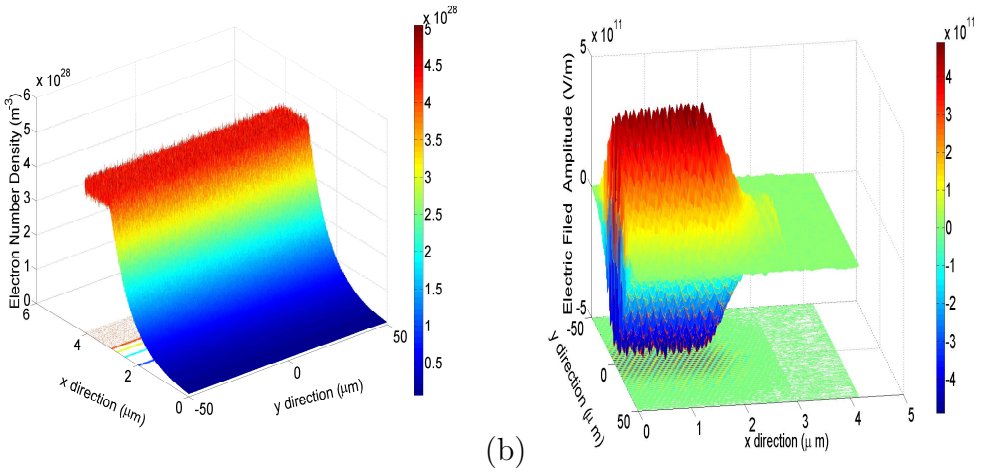

(a) (b)

Figure 6.8: a) A sample of electron number density before the laser irradiates the target with a 0.65 μm exponential scale length. b) The electric field profile for a laser with 38° incident angle and 100 μm focal spot for time 10 fs.

In the simulations, the peak electron density was limited between 0.3 n_c and 15 n_c where n_c is the critical density. An exponential density profile was assumed with a scale length of 0.65 μm (see figure 6.7 and 6.8a) which in the experiment was produced by the pre pulse as simulated by the fluid code HYADES. The laser

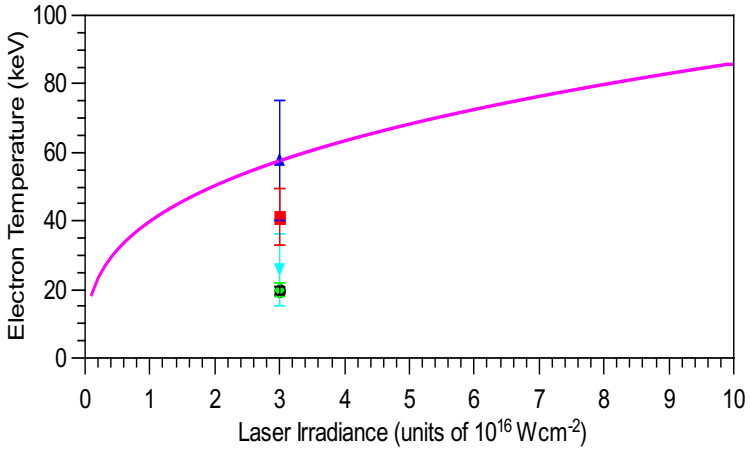

Figure 6.9: Hot electron temperature scaling suggested by Beg et al (magenta line). Measured electron temperatures for different incident angles and the same laser intensity are also shown. Blue triangle (▲) is for 28°, red square (■) is for 18°, cyan down triangle (▼) is for 23°, green diamond (◆) is for 38° and black circle (●) is for 33° degree incident angles.

incident angle has been varied from 10° to 38° degree to the target normal (see figure 6.5 figure and 6.8b).

The system size was 6 μm x 100 μm with a mesh resolution of 1024 x 1024 cells. For the simulation 16 particles were used in a cell.

Simulated electron energy distributions were used to extract the hot electron temperatures from the PIC code predictions (see figure 6.10). Transmitted emission from each channel can be calculated and ratios of the channels are used to extract the hot electron temperature by using the calculated channel signal ratio as a function of temperature (see figure 4.18). The experimental variation of electron temperatures for different angles with irradiance of 3×10^{16} W cm^{-2} is approximately constant with the Beg's scaling [45] (see figure 6.9).

To extract the electron temperature from the PIC code simulation, the number of electrons per unit energy range taken from the PIC code needs to be converted

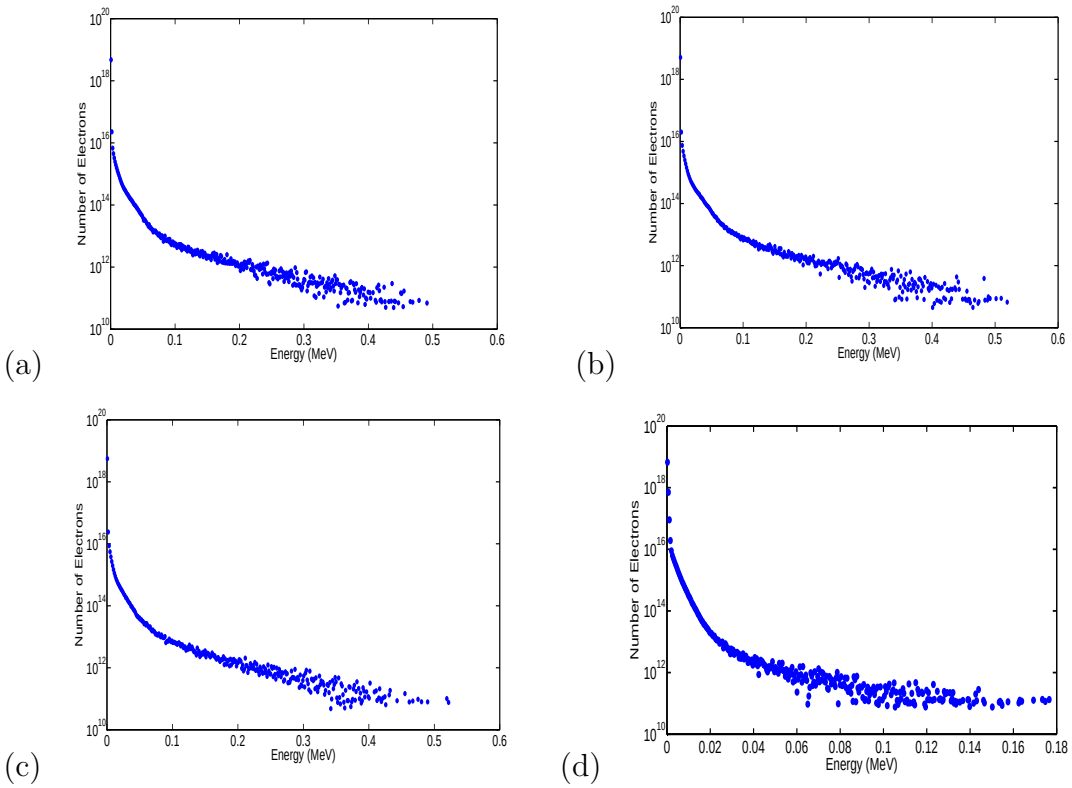

Figure 6.10: Electron energy spectrum generated from the PIC code for a) 18° degree and b)23°, c)28° and d) 38° degree angle of incident with the laser intensity of 3×10^{16} W cm^{-2} and scale length of 0.65 μm.

to the x-ray yield ε using

$$\varepsilon(E_p) \propto \int_{E_p}^{\infty} E^{-1/2} f(E) dE \tag{6.1}$$

where E is the electron energy and $f(E)$ is the electron energy distrubution function. If $f(E)$ is Maxwellian, the variation of $\varepsilon(E_p)$ can be shown to vary exponentially as $\varepsilon(E_p) \propto \exp(-E_p/kT)$ enabling a straight forward deduction of electron temperature kT from the $\varepsilon(E_p)$ variation.

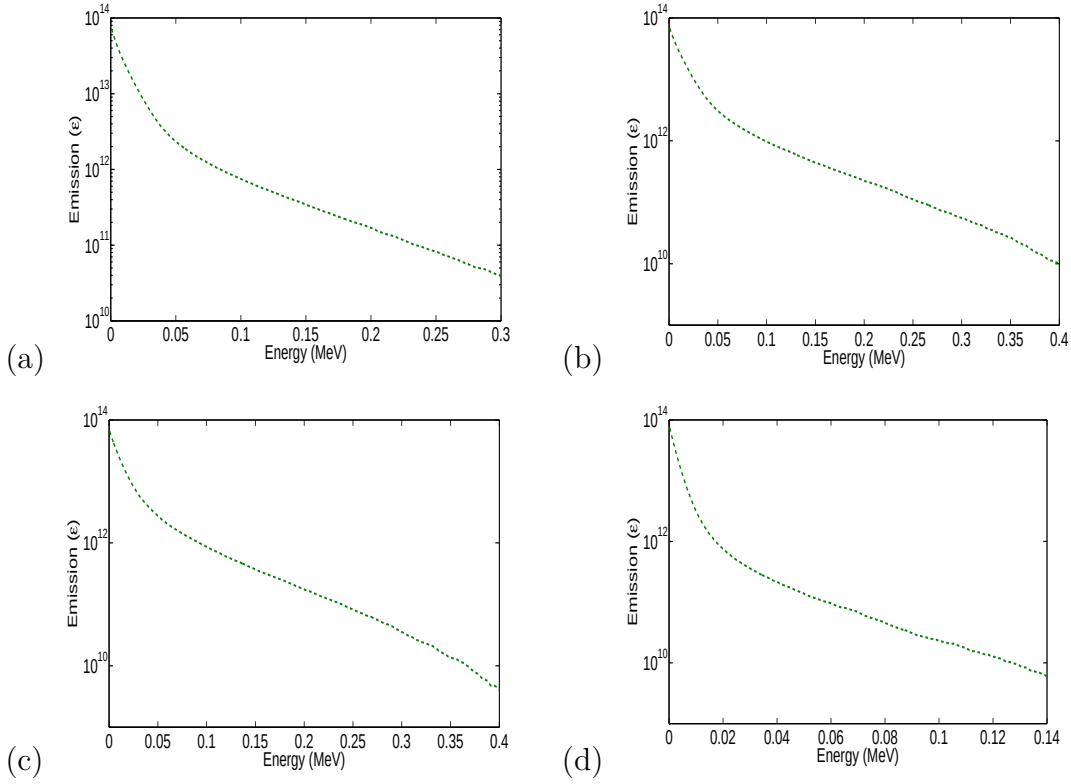

Figure 6.11: Calculated x-ray emission $\varepsilon(E_p)$ from the PIC code simulation for the generated electron energy spectra at a) 18° b) 23° c) 28° and d) 38° incident angles and $3 \times 10^{16}\,\mathrm{W\,cm^{-2}}$ irradiance. The spectra are calculated using equation 6.1.

If the electron energy distrubution $f(E)$ is non-Maxwellian or composed of two

or more electron energy distributions with different temperatures (eq. hot and thermal component), then the variation of $\varepsilon(E_p)$ can depart from an exponential variation (see figure 6.11).

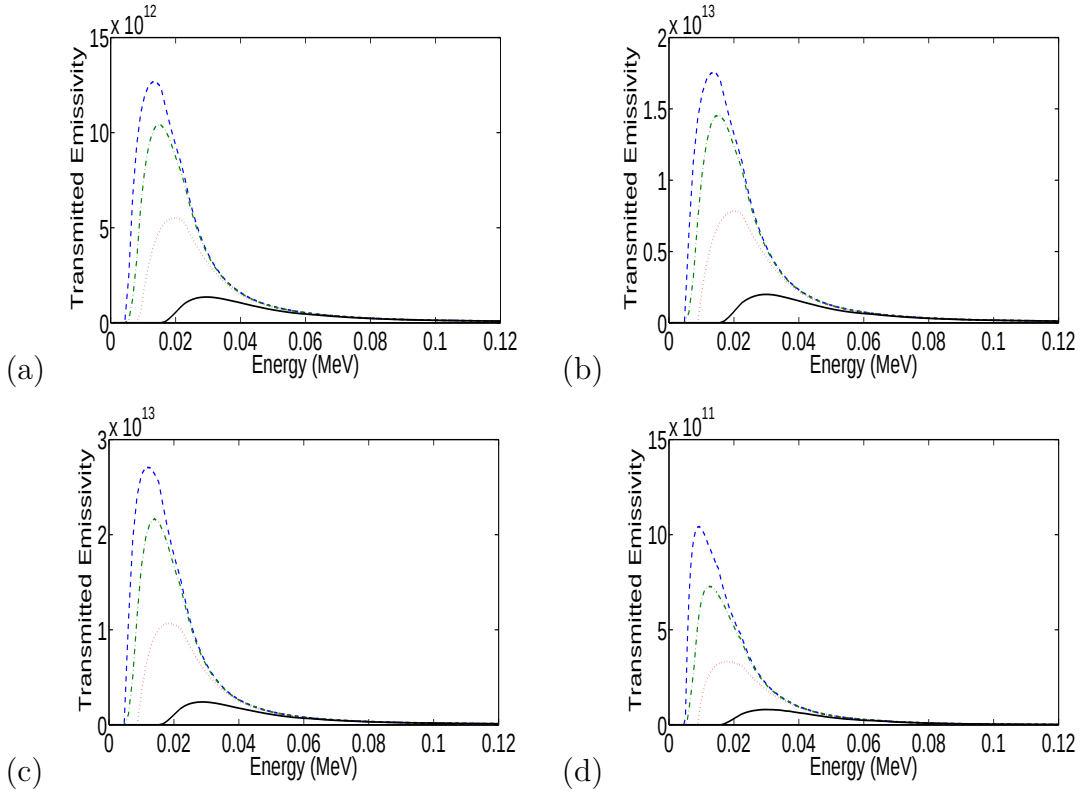

Figure 6.12: Simulated diode signals from the PIC code predicted electron energy distributions with a) 18° b) 28° c) 33° and d) 38° incident angles and $3 \times 10^{16}\,\mathrm{W\,cm^{-2}}$ irradiance. The blue line represents channel 1 , the green line is for channel 2, the red line is for channel 3 and the black line represents channel 4 (see section 4.4.2 for the filtering employed).

It is possible to use the predicted emissivity from the PIC code simulations to deduce the signals that would be produced on the diodes used in the experiment. The effect of the diode filter is illustrated in figure 6.12. Integrating the diode signal, the ratio of signals on different channel can be evaluated. The ratios are converted to temperatures using figure 4.18 which are found to be in approximate

agreement with the experimental values (see figure 6.13)

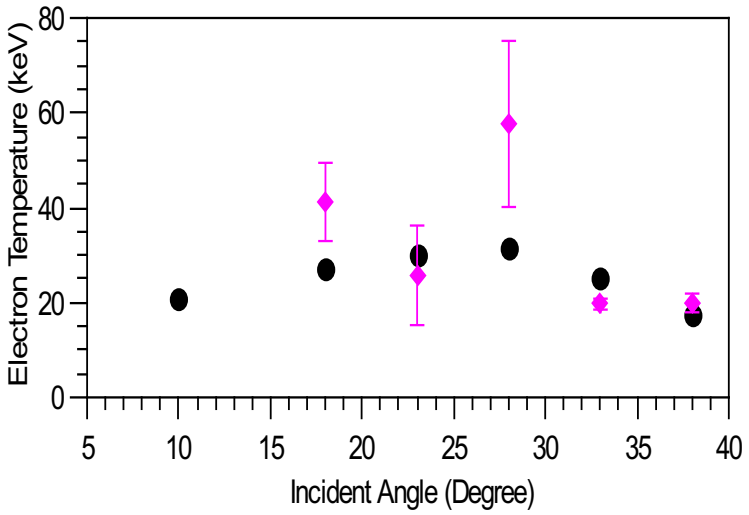

Figure 6.13: Experimentally measured electron temperatures (◆) are compared to EPOCH simulated temperatures (●) with a 0.65 μm scale length plasma.

6.5 Hot Electron Target Heating

Hot electrons are able to heat the solid target and ionise the buried iron layer so that it becomes transparent to probing EUV radiation [143]. Here we examine the level of hot electron heating which is likely to occur in the experiment discussed earlier in this chapter. As electron absorption cross sections for non relativistic electrons ($E << 0.51$ MeV) drop as $1/E^2$, the average absorption coefficient for an electron distribution with an electron temperature T (in units of 10 keV) is given by

$$\sigma_{av}(T) = \int_0^\infty \sigma_0 \frac{\exp\left(-\frac{E}{T}\right)}{E^2} dE \quad = \quad 6.5\frac{\sigma_0}{T} \quad . \tag{6.2}$$

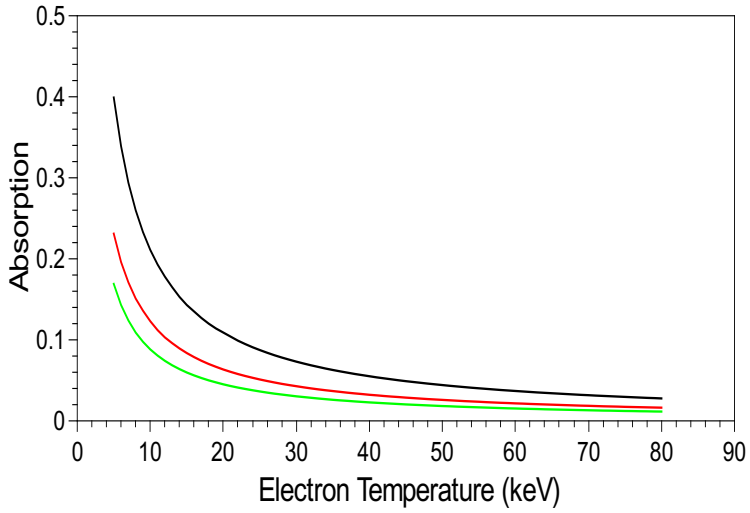

Figure 6.14: The fraction of hot electron energy absorbed in a target of 350 nm CH and 50 nm Fe as a function of the electron temperature (plotted using equations 6.2 and 6.3). The green and red curves show the absorption in the iron and plastic layer, respectively. The black curve represents the total target absorption.

An absorption A in a target layer of density ρ, thickness Δx can be derived by using the average absorption coefficient determined in equation 6.2 such that

$$A = 1 - \exp\left(-\sigma_{av}(T)\rho\Delta x\right) \quad . \tag{6.3}$$

Figure 6.14 shows the fraction of hot electron energy absorption in a target as a function of hot electron temperature. The hot electron energy absorption fraction in a 50 nm Fe layer is 0.045 for a temperature of 20 keV and for a 350 nm CH layer, the fractional absorption is 0.065 for a temperature of 20 keV which gives a total absorption of 0.11. The effect of hot electron heating can be estimated using figure 6.14 and a measurement of the number and temperature of hot electrons.

Figure 6.14 shows that at the hot electron temperatures (20 - 60 keV) measured with the diode array (figure 6.5) at the incident angles (20° - 40°) where there

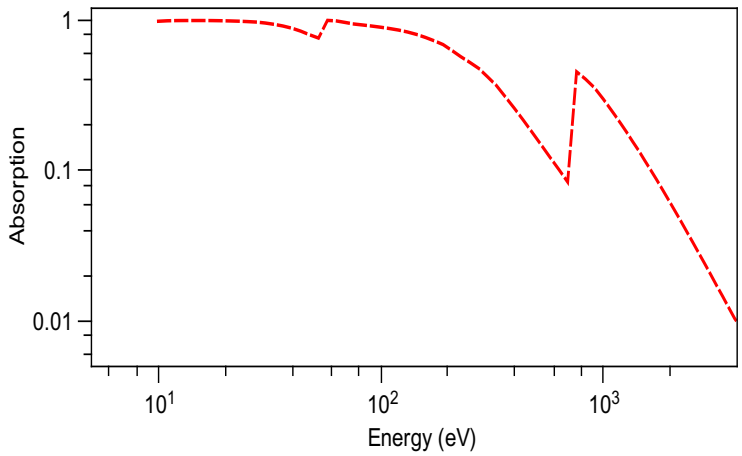

Figure 6.15: Radiation absorption in a cold solid target of 50 nm Fe as a function of photon energy. (Data is taken from CXRO [145])

are significant numbers of hot electrons (see figure 6.4), the heating of the iron layer in the target due to hot electrons is small (absorption $A < 0.1$). Modelling studies undertaken elsewhere (Shahzad et al. 2014)[144] confirm that hot electron heating of the iron layer is smaller than heating from thermal x-rays.

The transmission of 13.9 nm EUV laser radiation through the targets is illustrated in figure 6.16. The exponential transmission change of the iron layer due to ionization is well-fitted by modelling with radiation transport operating but is not affected by hot electron heating of the target.

Due to their long range penetration into solids, the above analysis shows that it is difficult for electrons to act as a significant source of heating in buried layer target experiments [146, 147]. Radiation absorption by bound-free processes is much larger (see eg figure 6.15), provided the photon energies are higher than the ionization energies present in the buried layer.

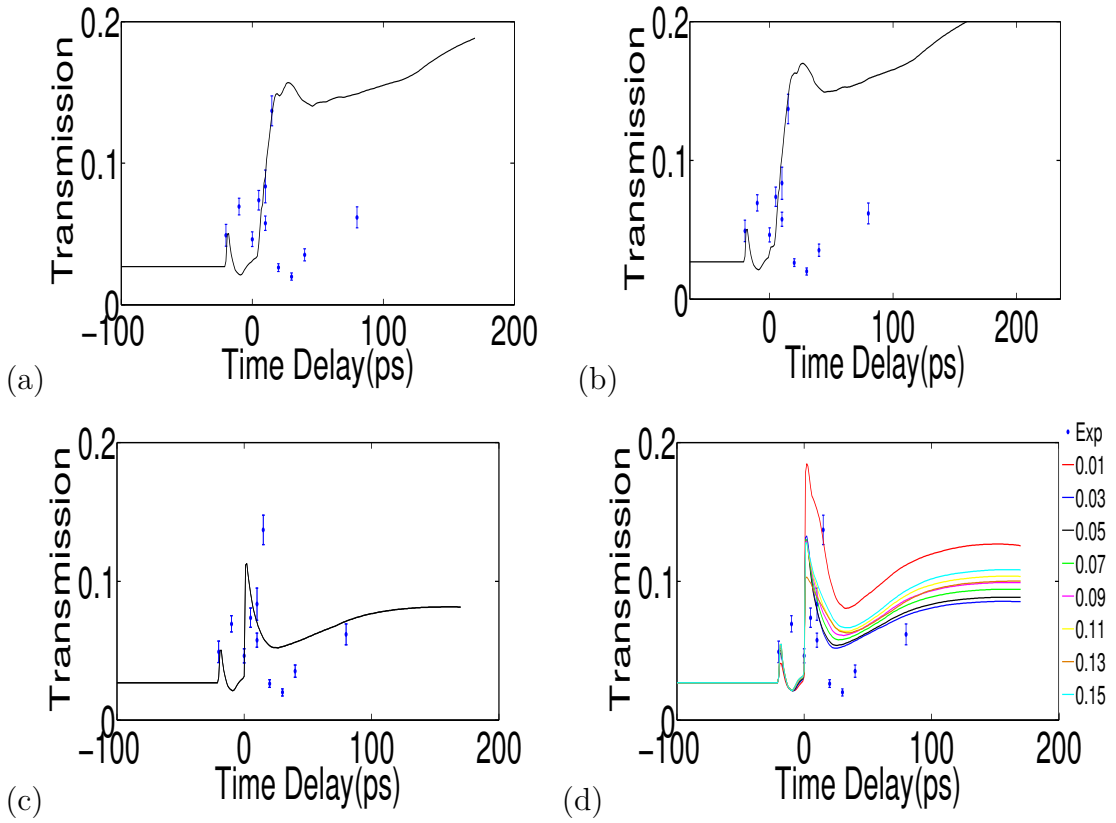

Figure 6.16: Transmitted EUV laser light superimposed with HYADES transmission simulations for a) radiation and hot electron heating turned off, b) Only hot electron heating is on the process, radiaton heating is off, c) radiation heating is turned on, hot electron heating is turned off and d) radiation and hot electron heating turned on and simulated for varying flux limiter. Laser irradiance was $3 \times 10^{16}\,\mathrm{W\,cm^{-2}}$ with an incident angle of 18°. The flux limiter was set at 0.05. (Figure is taken from M.Shahzad et al. [140])

6.6 Conclusion

In this chapter, the generation of laser produced hot electrons has been discussed for an experiment with an intensity of 3×10^{16} W cm^{-2}, wavelength of 0.8 μm and a target which has been heated with a pre-pulse of energy of 10% (3×10^{15} W cm^{-2}) of the main pulse. Ultra-short pulses do not modify the density profile generating hot electrons and so enable resonance absorption without density profile modification. It has been observed theoretically and experimentally that the hot electron temperature has a dependence on the laser incident angle due to the resonant absorption process. Absorption reaches a peak around 30 degrees angle of incidence which implies that the scale length of the plasma is 0.55 μm as also approximately obtained with HYADES fluid code simulations. Calculations show that hot electron heating of the buried iron layer in the targets is not significant for electrons with temperatures greater than a few keV. However, coronal radiation emission produce x-rays of energy $\approx$ 1 keV which are strongly absorbed by a buried iron layer. The conclusion from this work is that hot electrons are not generally suitable for isochoric heating of buried layer targets.

Chapter 7

Conclusions

This thesis has examined the production of hot electrons during laser interactions in the irradiance range 10^{16} to 10^{20} $\mathrm{W\,cm^{-2}}$. This intensity regime is accessible with modest ultra-short lasers at 10^{16} $\mathrm{W\,cm^{-2}}$ where resonance absorption dominates the acceleration of electrons. At higher irradiances (10^{18}-10^{20} $\mathrm{W\,cm^{-2}}$), petawatt class lasers are required where $\mathbf{J} \times \mathbf{B}$ acceleration of electrons becomes important. We have studied laser interactions where a deliberate pre-pulse has produced an expanding plasma into which a high irradiance laser interacts creating the hot electrons. The number of hot electrons produced at 10^{20} $\mathrm{W\,cm^{-2}}$ has been shown to linearly increase with the measured scale length of the plasma produced by a pre-pulse indicating that the electron acceleration is a volume ($\mathbf{J} \times \mathbf{B}$) effect. Resonance absorption as discussed in chapter 6 has been shown (chapter 2) to not increase in a simple linear proportionality.

In a final experiment, we have examined the role of hot electrons in heating solid targets and conclude that even at lower irradiances (10^{16} $\mathrm{W\,cm^{-2}}$) with relatively low energy hot electrons, their role in heating a target to high temperatures (> 10 eV) is limited.

Chapter 2 of this thesis has discussed the background theory behind laser

plasma interactions in plasmas. Laser absorption processes, fast electron generation and penetration in solids and plasma emissivities which are relevant to later work are reviewed. In order to understand laser produced electron acceleration, single electron motion in an electro magnetic field is discussed and the effect of a plasma channel with associated electric field examined in chapter 3. The theory of generating an ion channel due to the ponderomotive expulsion of electrons has been introduced.

We have shown that ion channels can be formed by the ponderomotive force and the generated electric field in a channel can affect hot electron acceleration in the direction of the laser beam for tightly focussed laser beams. Due to the energetic electrons which have been observed and presented in chapter 5, we have discussed electron acceleration in channels since tightly focussed laser beams can generate a channel and it has been shown in previous work that it is possible to accelerate electrons in channels. Our modelling suggests that parametric channel acceleration requires a tight focus or a self-focussing effect so that the laser beam has a diameter close to the diffraction limit.

The diagnostics which have been used during this work have been introduced in chapter 4. An electron spectrometer dispersion and error measurements are considered in detail. The fringing field of the electron spectrometer is considered in some detail along with a discussion of the effect of the geometry of the circular magnetic pole pieces on the electron spectrometer dispersion. We have shown that the fringing field of the electron spectrometer can effect the dispersion by 40 %. We have shown an error analysis of the electron spectra and temperature measurements.

Optical probe shadowgraphy which is used to get information on plasma den-

sity profiles and scale lengths has been introduced in chapter 4. X-ray diodes used in the thesis to measure plasma electron temperatures via x-ray emission are also discussed.

Measurements of electron spectra produced by ultra intense laser solid interactions at intensities up to 10^{20} W cm^{-2} with measured scale length of the plasma produced by a laser pre pulse are presented in chapter 5. High energy electrons of temperature 20-30 MeV were produced with a laser of 160 J energy on target and focussed to a 7 μm focal spot following a pre-pulse with intensities up to 10^{12} W cm^{-2} and energies up to 20 J on a 300 μm focal spot. 1D and 2D PIC code simulations have been run to understand the experimental results. The 1D PIC code temperatures are in approximate agreement for lower scale length plasmas ($L < 7.5\,\mu$m). However, the measured electron temperature with longer scale length plasmas dropped down unlike the code predicted values. There is good evidence that 2D effect influenced the generated hot electrons and indeed 2D code predictions using the EPOCH code are in good agreement with the experimental observations of electron temperatures. Our simulation results (chapter 3) show that with realistic plasma channels formed by the ponderomotive force, additional electron acceleration due to the channel is small. This is consistent with our observation (chapter 5) that the electron temperature decreases with large scale length plasma where channel formation can occur.

The LASERIX facility (intensity 10^{16} W cm^{-2}) with a shorter laser pulse (35 fs) has been used to generate hot electrons. Experimental and simulation work at LASERIX has been described in chapter 6. The laser irradiation had a prepulse 20 ps before the main pulse to create a pre-plasma with short scale lengths ($\approx$ 0.5 μm). Targets comprised 400 nm CH above 100 nm of Fe buried in the target.

Hot electron generation was investigated as a function of laser incident angle. The EPOCH code has been run for different angles and different scale lengths and the simulations compared to experimental electron temperature results. The generated electron temperatures are in agreement for a 0.65 μm scale length density profile. Ultra-short pulses do not modify the density profile generating hot electrons and so enable resonance absorption without density profile modification. It has been observed theoretically and experimentally that the hot electron temperature has a dependence on the laser incident angle due to the resonant absorption process. Analytic solution of resonance absorption as well as HYADES fluid code simulations show that the plasma scale length is approximately 0.55 - 0.65 μm in agreement with the experimental measurements. Calculations showed that hot electron heating of the buried iron layer in the targets is not significant for hot electrons with temperatures more than a few keV. However, coronal radiation emission produces x-rays of energy $\approx$ 1 keV which are mostly absorbed by a buried iron layer. The conclusion from this work is that hot electrons are not generally suitable for isochoric heating to high temperatures ($>$ 10 eV) in buried layer targets.

Appendix A

List of Publications

O. Culfa, G.J. Tallents, E. Wagenaars, C.P. Ridgers, R.J. Dance, A.K. Rossall, R.J. Gray, P. McKenna, C.D.R. Brown, S.F. James, D.J. Hoarty, N. Booth, A.P.L. Robinson, K.L. Lancaster, S.A. Pikuz, A.Ya. Faenov, T. Kampfer, K.S. Schulze, I. Uschmann and N.C. Woolsey. "Hot Electron Production in Laser Solid Interactions with a Controlled Pre-Pulse", *Physics of Plasmas*, 21:043106 (2014).

M. Shahzad and O. Culfa and A.K. Rossall and G.J. Tallents and L.A. Wilson and S.J. Rose and O. Guilbaud and S. Kazamias and M. Pittman and K. Cassou and J. Demailly and O. Delmas and A. Mestrallain and M. Farjardo and D. Ros . "Diagnosis of energy transport in iron buried layer targets using an extreme ultraviolet laser ", *Submitted to Phys.Plasmas*, (2014).

M. Shahzad and G.J. Tallents and O. Culfa and A.K. Rossall and L.A. Wilson and S.J. Rose and O. Guilbaud and S. Kazamias and M. Pittman and K. Cassou and J. Demailly and O. Delmas and A. Mestrallain and M. Farjardo and D. Ros . "Diagnosis of radiation heating in iron buried layer targets ", *14 th International*

Conference for X-Ray Lasers,In press by Springler, (2014).

S.B. Hansen, J. Colgan, A.Ya. Faenov, J. Abdallah, S.A. Pikuz, I.Yu. Skobelev, E. Wagenaars, N. Booth, O. Culfa, R.J. Dance, G.J. Tallents, R.G. Evans, R.J. Gray, T. Kaempfer, K.L. Lancaster, P. McKenna, A.K. Rossall, , K.S. Schulze, I. Uschmann, A.G. Zhidkov, and N.C. Woolsey. "Detailed analysis of hollow ions spectra from dense matter pumped by X-ray emission of relativistic laser plasma.", *Physics of Plasmas*,21: 031213 (2014).

J. Colgan, J. Abdallah, A.Ya. Faenov, S.A. Pikuz, E. Wagenaars, N. Booth, O. Culfa, R.J. Dance, R.G. Evans, R.J. Gray, T. Kaempfer, K.L. Lancaster, P. McKenna, A.K. Rossall, I.Yu. Skobelev, K.S. Schulze, I. Uschmann, A.G. Zhidkov and N.C. Woolsey. "Exotic Dense-Matter States Pumped by a Relativistic Laser Plasma in the Radiation-Dominated Regime.", *Phys.Rev.Lett.* 110: 125001 (2013).

S.A. Pikuz, A.Ya. Faenov, J. Colgan, R.J. Dance, J. Abdallah, E. Wagenaars, N. Booth, O. Culfa, R.G. Evans, R.J. Gray, T. Kaempfer, K.L. Lancaster, P. McKenna, A.K. Rossall, I.Yu. Skobelev, K.S. Schulze, I. Uschmann, A.G. Zhidkov, N.C. Woolsey. "Measurement and simulations of hollow atom X-ray spectra of solid-density relativistic plasma created by high-contrast PW optical laser pulses.", *HEDP* 9: 560-567 (2013).

G. Chatterjee, P.K. Singh, A.P.L. Robinson, N. Booth, O. Culfa, R.J. Dance, L.A. Gizzi, R.J. Gray, J.S. Green, P.Koester, G.R. Kumar, L.Labate, Amit D.

Lad, K.L. Lancaster, J. Pasley, N.C. Woolsey, P.P. Rajeev. "Micron-Scale Mapping of Megagauss Magnetic Fields in Petawatt Laser-Solid Interactions.", *Physics of Plasmas* arXiv:1307.7856 (2013).

N.C. Woolsey, S.A. Pikuz, A.Ya Faenov, R.J. Dance, E. Wagenaars, N. Booth, O. Culfa, R.G. Evans, R.J. Gray, T. Kaempfer, K. Lancaster, P. McKenna, A.K. Rossall, I.Yu Skobelev, K.S. Schulze, I. Uschmann, A.G. Zhidkov, J. Abdallah Jr., J. Colgan. "Exotic hollow atom states pumped by relativistic laser plasma in a radiation dominant regime.", *Bulletin of the American Physical Society 55th Annual Meeting of the APS Division of Plasma Physics* , 58:16 (2013)

G.J. Tallents, M. Shahzad, A.K. Rossall, O. Guilbaud, S. Kazamias, M. Pittman, K. Cassou, J. Demailly, O. Delmas, A. Mestrallain, V. Aslanyan, O. Culfa, L.A. Wilson, M. Farjardo, D. Ros. "Probing of laser-irradiated solid targets using extreme ultraviolet radiation.", *X-Ray Lasers and Coherent X-Ray Sources: Development and Applications X,*,Proc. SPIE 8849 (2013)

G. Chatterjee, P.K. Singh, Amit D. Lad, A.P.L. Robinson, N. Booth, J.S. Green, K.L. Lancaster, P. Koester, L.A. Gizzi, R.J. Gray, R.J. Dance, O. Culfa, J. Pasley, N.C. Woolsey, G.R. Kumar, P.P. Rajeev. "Spatial and Temporal Evolution of Megagauss Magnetic Fields in Petawatt Laser-Solid Interactions in the Fast Ignition Regime.", *Bulletin of the American Physical Society 54th Annual Meeting of the APS Division of Plasma Physics* , 57:12 (2012)

L.M.R. Hobbs, D.J. Hoarty, P. Allan, C.R.D. Brown, M.P. Hill, S.F. James,

R. Shepherd, K.L. Lancaster, R.J. Gray, E. Wagenaars, R.J. Dance, A.K. Rossall, O. Culfa, N.C. Woolsey. "Demonstration of short pulse laser heating of solid targets to temperatures of 600 eV at depths exceeding 30 μm using the Orion high power laser.", *Bulletin of the American Physical Society 54th Annual Meeting of the APS Division of Plasma Physics* , 57:12 (2012)

N. Booth, J. Green, K. Lancaster, A.P.L. Robinson, P.P. Rajeev, O. Culfa, R.J. Dance, J. Pasley, N.C. Woolsey, G. Chatterjee, P. Singh, G.R. Kumar, P. Hakel, R.C. Mancini, L.A. Gizzi, P. Koester, L. Labate and R. Gray. "Multi Mega-Gauss magnetic field and electron anisotropy measurements in ultra-relativistic plasmas.", *39th EPS Conference on Plasma Physics 2012*, 1:105-108 (2012)

References

[1] John Wesson. *Tokamaks.* Clarendon Press-Oxford, 2004. 1

[2] Denis Keefe. *Ann. Rev. Nucl. Part. Sci*, 32:391–441, 1982. 1

[3] John Lindl. *Physics of Plasmas*, 2(11):3933, 1995. 1, 3

[4] J. Nuckolls, L. Wood, A. Thiessen, and G. Zimmerman. *Nature*, 239:139–142, 1972. 1

[5] M. Tabak, J. Hammer, M.E. Glinsky, W.L. Kruer, S.C. Wilks, J. Woodworth, E.M. Campbell, M.D. Perry, and R.J. Mason. *Phys.Plasmas*, 1:1626–1635, 1994. 2, 28, 86, 111

[6] R. Kodama, P.A. Norreys, K. Mima, A.E. Dangor, R.G. Evans, H. Fujita, Y. Kitagawa, K. Krushelnick, T. Miyakoshi, N. Miyanaga, T. Norimatsu, S.J. Rose, T. Shozaki, K. Shigemori, A. Sunahara, M. Tampo, K.A. Tanaka, Y. Toyama, T. Yamanaka, and M. Zepf. *Nature*, 412:798–802, 2001. 2, 111

[7] J. Meyer ter Vehn. *Plasma Phys. Cont. Fusion*, 43:A113–A125, 2001. 2

[8] W.L. Kruer, E.M. Campbell, C.D. Decker, S.C. Wilks, J. Moody, T. Orzechowski, L. Powers, L.J. Suter, B.B. Afeyan, and N. Dague. *Plasma Phys. Cont. Fusion*, 41:A409–A417, 1999. 2

[9] S.C. Wilks, A.B. Langdon, T.E. Cowan, M. Roth, M. Singh, S.P. Hatchett, M.H. Key, D.M. Pennington, A. MacKinnon, and R.A. Snavely. *Phys.Plasmas*, 8:542, 2001. 2, 7, 111

[10] M. Borghesi, J. Fuchs, S.V. Bulanov, A.J. Mackinnon, P.K Patel, and M. Roth. *Fusion Science and Tech.*, 49:412–439, 2005. 2, 7

[11] P.A. Norreys, R. Allott, R.J. Clarke, J. Collier, D. Neely, S.J. Rose, M. Zepf, M. Santala, A.R. Bell, K. Krushelnick, A.E. Dangor, N.C. Woolsey, R.G. Evans, H. Habara, T. Norimatsu, and R. Kodama. *Phys.Plasmas*, 7:3721, 2000. 6

[12] T. Nakamura, H. Sakagami, H. Nagatomo T. Johzaki, K.Mima, and James Koga. *Phys.Plasmas*, 14:103105, 2007.

[13] J.J. Honrubia and J. Meyer ter Vehn. *Plas.Phys.Cont.Fus.*, 51:014008, 2009. 6

[14] P.M. Nilson, A.A. Solodov, J.F. Myatt, W. Theobald, P.A. Jaanimagi, L. Gao, C. Stoeckl, R.S. Craxton, J.A. Delettrez, B. Yaakobi, J.D. Zuegel, B.E. Kruschwitz, C. Dorrer, J.H. Kelly, K.U. Akli, P.K. Patel, A.J. Mackinnon, R. Betti, T.C. Sangster, and D.D. Meyerhofer. *Phys. Rev. Lett.*, 105:235001, 2010. 6

[15] Paul Gibbon. *Short Pulse Laser Interactions with Matter*. Imperial College Press, 2005. 6, 23, 42, 44, 88

[16] A.G. MacPhee, L. Divol, A.J. Kemp, K.U. Akli, F.N. Beg, C.D. Chen, H.Chen, D.S. Hey, R.J. Fedosejevs, R.R. Freeman, M. Henesian, M.H. Key,

S. Le Pape, A. Link, T. Ma, A.J. Mackinnon, V.M. Ovchinnikov, P.K. Patel, T.W. Phillips, R.B. Stephens, M. Tabak, R. Town, Y.Y. Tsui, L.D. Van Woerkom, M.S. Wei, and S. C. Wilks. *Phys.Rev.Lett.*, 104:055002, 2010. 7

[17] P. McKenna, F. Lindau, O. Lundh, D.C. Carroll, R.J. Clarke, K.W.D. Ledingham, T. McCanny, D. Neely, A.P.L. Robinson, L. Robson, P.T Simpson, C.G. Wahlstrom, and M. Zepf. *Plasma Phys. Control. Fusion*, 49:B223–B231, 2007. 7, 30, 111

[18] P. McKenna, K.W.D. Ledingham, J.M. Yang, L. Robson, T. McCanny, S. Shimizu, R.J. Clarke, D. Neely, K. Spohr, R. Chapman, R.P. Singhal, K. Krushelnick, M.S. Wei, and P.A. Norreys. *Phys.Rev.E*, 70:036405, 2004. 111

[19] A. Maksimchuk, S. Gu, K. Flippo, D. Umstadter, and V.Yu. Bychenkov. *Phys. Rev. Lett.*, 84:4108–4111, 2000.

[20] R.A. Snavely, M.H. Key, S.P. Hatchett, T.E. Cowan, M.Roth, T.W. Phillips, M.A. Stoyer, E.A. Henry, T.C. Sangster, M.S. Singh, S.C. Wilks, A. MacKinnon, A. Offenberger, D.M Pennington, K. Yasuike, A.B. Langdon, B.F. Lasinski, J. Johnson, M.D. Perry, and E.M. Campbell. *Phys. Rev. Lett.*, 85:2945–2948, 2000.

[21] L. Willingale, A.G.R. Thomas, P.M. Nilson, M.C. Kaluza, S. Bandyopadhyay, A.E. Dangor, R.G. Evans, P. Fernandes, M.G. Haines, C. Kamperidis, R.J. Kingham, S. Minardi, M. Notley, C.P. Ridgers, W. Rozmus, M. Sherlock, M. Tatarakis, M.S. Wei, Z. Najmudin, and K. Krushelnick. *Phys. Rev. Lett.*, 84:4108–4111, 2000. 7, 9, 28

[22] B.J. Albright, L. Yin, Kevin J. Bowers, B.M. Hegelich, K.A. Flippo, T.J.T. Kwan, and J. C. Fernandez. *Physics of Plasmas*, 14:094502, 2007. 8

[23] L. Yin, B.J. Albright, B. Hegelich, K.J. Bowers, K.A. Flippo, T.J.T. Kwan, and J.C. Fernandez. *Physics of Plasmas*, 14:056706, 2007.

[24] D. Jung, L. Yin, D.C. Gautier, H.C. Wu, S. Letzring, B. Dromey, R. Shah, S. Palaniyappan, T. Shimada, R.P. Johnson, J. Schreiber, D. Habs, J.C. Fernandez, B.M. Hegelich, and B. J. Albright. *Physics of Plasmas*, 20:083103, 2013. 8

[25] A.P.L. Robinson, M. Zepf, S. Kar, R.G. Evans, and C. Bellei. *New Journal of Physics*, 10:013021, 2008. 9

[26] B. Qiao, M. Zepf, M. Borghesi, B. Dromey, M. Geissler, A. Karmakar, and P. Gibbon. *Phys.Rev.Lett.*, 105:155002, 2010.

[27] A.P.L Robinson, R.M.G.M Trines, N.P. Dover, and Z. Najmudin. *Plasma Phys. Control. Fusion*, 54:115001, 2012. 9

[28] L. Willingale, S.P.D. Mangles, P.M. Nilson, R.J. Clarke, A.E. Dangor, M.C. Kaluza, S. Karsch, K.L. Lancaster, W.B. Mori, Z. Najmudin, J. Schreiber, A.G.R. Thomas, M.S. Wei, and K. Krushelnick. *Phys. Rev. Lett.*, 96:245002, 2006. 9

[29] J.S Green, N.P Dover, M. Borghesi, C.M Brenner, F.H Cameron, D.C Carroll, P.S Foster, P. Gallegos, G. Gregori, P. McKenna, C.D Murphy, Z. Najmudin, C.A.J Palmer, R. Prasad, L. Romagnani, K.E Quinn,

J. Schreiber, M.J.V Streeter, S. Ter-Avetisyan, O. Tresca, M. Zepf, and D Neely. *Plas.Phys.Cont.Fus.*, 56:084001, 2014.

[30] J. Psikal, O. Klimo, S. Weber, and D. Margarone. *Phys.Plasmas*, 21:073108, 2014. 9

[31] W.L. Kruer. *The physics of laser plasma interactions.* California, Addison - Wesley Publishing Company, 1988. 13, 14, 15, 18, 19, 24, 37, 42, 44, 87, 112

[32] J.T. Larsen and S.M. lane. Code commercially available from cascade applied sciences inc.,larsen@casinc.com. *JQSRT*, 51, 1994. 13

[33] Shalom Eliezer. *The interaction of high power lasers with plasmas.* IOP Publishing, 2002. 14, 17, 24, 44, 88

[34] W.L. Kruer and K. Estabrook. *Phys.Fluids.*, 28:430, 1985. 14, 26

[35] S.C. Wilks and W.L. Kruer. *IEEE Journal of Quantum Electronics*, 33:11, 1997. 14, 19

[36] S.C. Wilks, W.L. Kruer, M. Tabak, and A.B. Langdon. *Phys.Rev.Lett.*, 69:9, 1992. 14, 27

[37] D. Giulietti and L.A. Gizzi. *La Rivista del Nuovo Cimento*, 21:1, 1998. 17

[38] L. Schlessinger and J. Wright. *Phys.Rev.A*, 20:1934–1945, 1979. 18

[39] S. Pfalzner. *An introduction to inertial confinement fusion.* CRC press, 2006. 19, 24

[40] F. Brunel. *Phys.Rev.Lett.*, 59:52, 1987. 21

[41] P. Gibbon and A.R. Bell. *Phys.Rev.Lett.*, 68:1535–1538, 1992. 23, 27, 87, 111

[42] M.K. Grimes, Y.S. Lee, A.R. Rundquist, and M.C. Downer. *Phys.Rev.Lett.*, 82:4010, 1999. 23

[43] L.M. Chen, J. Zhang, Q.L. Dong, H. Teng, and T.J. Liang. *Phys.Plasmas*, 8:2925, 2001. 23

[44] M.G. Haines, M.S. Wei, F.N. Beg, and R.B. Stephens. *Phys.Rev.Lett*, 102(045008), 2009. 24, 27, 28, 87, 111

[45] F.N. Beg, A.R. Bell, A.E. Dangor, C.N. Danson, A.P. Fews, M.E. Glinsky, B.A. Hammel, P. Lee, P.A. Norreys, and M. Tatarakis. *Physics of Plasmas*, 4:447–458, 1997. 24, 27, 111, 123

[46] P. McKenna, D. Neely, R. Bingham, and D.A. Jaroszynski. *Laser plasma interactions and applications*. Scottish Graduate Series, 2013. 26

[47] D.W. Forslund, J.M. Kindel, and K. Lee. *Phys.Rev.Lett*, 39(284), 1977. 27

[48] F. Brunel. *Phys.Fluids.*, 31:2714, 1988. 27

[49] P. Gibbon and E. Forster. *Plasma Phys.Control.Fusion*, 38:769, 1996. 28

[50] W.T. Chu, B.A. Ludewigt, and T.R. Renner. *Rev. Sci. Instrum.*, 64:2055, 1993. 28

[51] T. Tajima, D. Habs, and X. Yan. *Rev. Accl. Sci. Tech.*, 02:201–228, 2009.

[52] K.W.D. Ledingham, P. McKenna, and R.P. Singhal. *Science*, 300:5622, 2003.

[53] P. McKenna, D.C. Carroll, O. Lundh, F. Nurnberg, K. Markey, S. Bandyopadhyay, D. Batani, R.G. Evans, R. Jafer, Saty Kar, D. Neely, D. Pepler, M.N. Quinn, R. Redaelli, M. Roth, C.G. Wahlstrom, X.H. Yuan, and Matthew Zepf. *Laser And Particle Beams*, 26(4):591–596, 2008. 87, 111

[54] Y. Sentoku, T.E. Cowan, A. Kemp, and H. Ruhl. *Phys.Plasmas*, 10(2009), 2003. 28, 87

[55] T. Tajima and J.M. Dawson. Laser electron Accelerator. *Physical Review Letters*, 43(4):267–270, 1979. 28

[56] A. Pukhov and J. Meyer-Ter-Vehn. *Applied Physics B.*, 74:355–361, 2002. 49, 88

[57] S. Atzeni and J. Meyer-Ter-Vehn. *The Physics of Inertial Fusion.* Oxford University Press, 2004. 28, 30, 44

[58] A. Pukhov, Z.-M. Sheng, and J. Meyer-ter Vehn. *Physics of Plasmas*, 6(7):2847, 1999. 28, 49, 88

[59] Robert B. Palmer. *Journal of Applied Physics*, 43(7):3014, 1972. 29

[60] E.D. Courant, C. Pellegrini, and W. Zakowicz. *Physical Review A*, 32(5):2813–2823, 1985.

[61] Iddo Wernick and T.C. Marshall. *Physical Review A*, 46(6):3566–3568, 1992. 29

[62] C. Gahn, G. Tsakiris, A. Pukhov, J. Meyer-ter Vehn, G. Pretzler, P. Thirolf, D. Habs, and K. Witte. *Physical Review Letters*, 83(23):4772–4775, 1999. 29

[63] S. Kneip, S. Nagel, C. Bellei, N. Bourgeois, A. Dangor, A. Gopal, R. Heathcote, S. Mangles, J. Marquès, A. Maksimchuk, P. Nilson, K. Phuoc, S. Reed, M. Tzoufras, F. Tsung, L. Willingale, W. Mori, A. Rousse, K. Krushelnick, and Z. Najmudin. *Physical Review Letters*, 100(10):105006, 2008. 50, 72

[64] Hai-Cheng Wu, Bai-Song Xie, Ming-Ping Liu, Xue-Ren Hong, Shan Zhang, and M.Y. Yu. *Physics of Plasmas*, 16(7):073108, 2009.

[65] Y. Glinec, J. Faure, A. Lifschitz, J.M. Vieira, R.A. Fonseca, L.O. Silva, and V. Malka. *EPL (Europhysics Letters)*, 81(6):64001, 2008. 29

[66] M. Santala, M. Zepf, I. Watts, F. Beg, E. Clark, M. Tatarakis, K. Krushelnick, A. Dangor, T McCanny, I Spencer, R. Singhal, K. Ledingham, S. Wilks, A. Machacek, J. Wark, R Allott, R. Clarke, and P. Norreys. *Physical review letters*, 84(7):1459–62, 2000. 30, 87

[67] R. Stephens, R. Snavely, Y. Aglitskiy, F. Amiranoff, C. Andersen, D. Batani, S. Baton, T. Cowan, R. Freeman, T. Hall, S. Hatchett, J. Hill, M. Key, J. King, J. Koch, M. Koenig, A. MacKinnon, K. Lancaster, E. Martinolli, P. Norreys, E. Perelli-Cippo, M. Rabec Le Gloahec, C. Rousseaux, J. Santos, and F. Scianitti. *Physical Review E*, 69(6):066414, June 2004.

[68] K. Lancaster, J. Green, D. Hey, K. Akli, J. Davies, R. Clarke, R. Freeman, H. Habara, M. Key, R. Kodama, K. Krushelnick, C. Murphy, M. Nakatsutsumi, P. Simpson, R. Stephens, C. Stoeckl, T. Yabuuchi, M. Zepf, and P. Norreys. *Physical Review Letters*, 98(12):125002, 2007. 30

[69] A.R. Bell, A.P.L. Robinson, M. Sherlock, R.J. Kingham, and W. Rozmus. *Plasma Physics and Controlled Fusion*, 48(3):R37–R57, 2006. 30

[70] J. Davies. *Physical Review E*, 65(2):026407, 2002.

[71] R. Mason. *Physical Review Letters*, 96(3):035001, 2006. 30

[72] Kenneth S.Krane. *Introductory nuclear physics.* John Wiley and sons, 1988. 31

[73] NIST. http://physics.nist.gov/physrefdata/xraymasscoef/chap2.html, December 2013. 32, 83

[74] A.R. Bell, J.R. Davies, S. Guerin, and H. Ruhl. *Plasma Physics and Controlled Fusion*, 39:653–659, 1997. 33

[75] H.M. Milchberg, R.R. Freeman, S.C. Davey, and R.M. More. *Physical Review Letters*, 61(20):2364–2367, 1988. 34

[76] D. Salzman. *Atomic Physics in Hot Plasmas.* Oxford University Press, 1998. 34, 36

[77] Extendable PIC Open Collaboration project UK. http://ccpforge.cse.rl.ac.uk/gf/project/epoch, April 2013. 37, 106

[78] A.P.L. Robinson, R.M.G.M. Trines, J. Polz, and M. Kaluza. *Plasma Phys. Control.Fusion*, 53(065019), 2011. 39, 101

[79] C.K. Birdsall and J.M. Dawson. *Plasma physics via computer simulations.* McGraw-Hill, 1985. 39

[80] M. Shahzad, G.J. Tallents, A.B. Steel, L. Hobbs, D.J. Hoarty, and J.Dunn. *Phys.Plasmas*, 21(082702), 2014. 48

[81] A.V. Arefiev, B.N. Breizman, M. Schollmeier, and V.N. Khudik. *Phys.Rev.Lett.*, 108, 2012. 49, 50

[82] A. Pukhov, D an der Brugge, and I. Kostyukov. *Plasma Phys.Control.Fusion*, 52(124039), 2010. 49

[83] Alexey V. Arefiev, Marius Schollmeier, and Vladimir N. Khudik. *AIP Conference Proceedings*, 1507(1):363–368, 2012. 50, 56

[84] S.P.D. Mangles, B.R. Walton, M. Tzoufras, Z. Najmudin, R.J. Clarke, A.E. Dangor, R.G. Evans, S. Fritzler, A. Gopal, C. Hernandez-Gomez, W.B. Mori, W. Rozmus, M. Tatarakis, A.G.R. Thomas, F.S. Tsung, M.S. Wei, and K. Krushelnick. *Phys. Rev. Lett.*, 94:245001, 2005. 50, 88

[85] B.R. Walton, S.P. Mangles, Z. Najmudin, M. Tatarakis, M.S. Wei, A. Gopal, C. Marle, A.E. Dangor, K. Krushelnick, S. Fritzler, V. Malka, R.J. Clarke, and C. Hernandez-Gomez. *Phys.Plasmas*, 13:113103, 2006.

[86] C. Gahn, G.D. Tsakiris, G. Pretzler, K.J. Witte, P. Thirolf, D. Habs, C. Delfin, and C.-G. Wahlstrom. *Phys.Plasmas*, 9:987, 2002. 50

[87] S.P.D. Mangles. *Measurement of Relativistic Electrons from Intense Laser Plasma Interactions*. PhD thesis, Department of Physics,Plasma Physics Group,Imperial College London, 2005. 60, 66, 70, 74

[88] M. Lezius, S. Dobosz, D. Normand, and M. Schmidt. *Phys.Rev.Lett.*, 80:261–264, 1998. 65

[89] C.D. Murphy. Private communications. 67, 69

[90] FUJIFILM. http://www.fujifilm.com, April 2013. 70, 72

[91] G. Fiksel, F. J. Marshall, C. Mileham, and C. Stoeckl. *Review of Scientific Instruments*, 83(086103), 2012. 70

[92] Kazuo A. Tanaka, T. Yabuuchi, T. Sato, R. Kodama, Y. Kitagawa, T. Takahashi, T. Ikeda, Y. Honda, and S. Okuda. *Review of Scientific Instruments*, 76(1):013507, 2005. 70, 72, 74

[93] I.J. Paterson, R.J. Clarke, N.C. Woolsey, and G. Gregori. *Measurement Science and Technology*, 19:095301, 2008. 70

[94] D. Taylor, E. Liang, T. Clarke, A. Henderson, P. Chaguine, X. Wang, G. Dyer, K. Serratto, N. Riley, M. Donovan, and T. Ditmire. *High Energy Density Physics*, 9(2):363–368, 2013. 72, 87

[95] S. Cipiccia, M.R. Islam, B. Ersfeld, R.P. Shanks, E. Brunetti, G. Vieux, X. Yang, R.C. Issac, S.M. Wiggins, G.H. Welsh, M.-P. Anania, D. Maneuski, R. Montgomery, G. Smith, M. Hoek, D.J. Hamilton, N.R.C. Lemos, D. Symes, P.P. Rajeev, V.O. Shea, J.M. Dias, and D.A. Jaroszynski. *Nature Physics*, 7(11):867–871, 2011.

[96] S. Kneip, S. Nagel, S. Martins, S. Mangles, C. Bellei, O. Chekhlov, R. Clarke, N. Delerue, E. Divall, G. Doucas, K. Ertel, F. Fiuza, R. Fonseca, P. Foster, S. Hawkes, C. Hooker, K. Krushelnick, W. Mori, C. Palmer, K. Phuoc, P. Rajeev, J. Schreiber, M. Streeter, D. Urner, J. Vieira, L. Silva, and Z. Najmudin. *Physical Review Letters*, 103(3):035002, 2009. 72, 87

[97] S.G. Gales and C.D. Bentley. *Review of Scientific Instruments*, 75(10):4001, 2004. 72

[98] S. Masuda, E. Miura, K. Koyama, and S. Kato. *The Review of scientific instruments*, 79(8):083301, 2008. 72

[99] N. Nakanii, K. Kondo, T. Yabuuchi, K. Tsuji, K.A. Tanaka, S. Suzuki, T. Asaka, K. Yanagida, H. Hanaki, T. Kobayashi, K. Makino, T. Yamane, S. Miyamoto, and K. Horikawa. *The Review of scientific instruments*, 79(6):066102, 2008. 72

[100] Y. Amemiya, T. Matsushita, A. Nakagawa, Y. Satow, J. Miyahara, and J.-I Chikawa. *Nuclear Instruments and Methods in Physics Research Section A*, 266:645–653, 1988. 73

[101] J. Miyahara, K. Takahashi, Y. Amemiya, N. Kamiya, and Y. Satow. *Nuclear Instruments and Methods in Physics Research Section A*, 246:572–578, 1986. 73

[102] A. Mancić, J. Fuchs, P. Antici, S.A. Gaillard, and P. Audebert. *The Review of scientific instruments*, 79(7):073301, 2008. 73

[103] I.H. Hutchinson. *Principels of Plasma Diagnostics*. Cambridge University Press, 2002. 76

[104] A.A. Ovsyannikov and M.F. Zhukov. *Plasma Diagnostics*. Cambridge International Science Publishing, 2005. 76

[105] O.F. Kostenko, A.V. Ovchinnokov, O.V. Chefonov, S.A. Romashevskiy,

V.P. Petrovskiy, N.E. Andreev, and M B Agrana. *Phys.Scr*, 89:075605, 2014. 78

[106] A.K. Rossall, L.M.R. Gartside, S. Tripathi, D.S. Munda, N.K. Gupta, L.J. Dhareshwar, J. Gaffney, S.J. Rose, and G.J. Tallents. *J.Phys.B:At.Mol.Opt.Phys*, 43:155403, 2010.

[107] T.D. Donnelly, M. Rust, I. Weiner, M. Allen, R.A. Smith, C.A. Steinke, S. Wilks, J Zweiback, T.E. Cowan, and T Ditmire. *J.Phys.B:At.Mol.Opt.Phys*, 34:L313–L320, 2001. 78

[108] Donald A. Neamen. *Semiconductor Physics And Devices* . McGraw-Hill Higher Education, 2003. 78, 80

[109] S.M Sze. *Physics of Semiconductor Devices*. John Wiley & Sons, Toronto, 1969. 78, 80

[110] A.G. Chynoweth and K.G. McKay. *Physical Review E*, 108(1):29–34, 1957. 80

[111] F. Scholze, H. Rabus, and G. Ulm. *Journal of Applied Physics*, 84(5):2926–2939, 1998. 80

[112] OSI Optoelectronics company. http://www.osioptoelectronics.com/, December 2013. 80, 81

[113] H.O. Funsten, D.M. Suszcynsky, S.M. Ritzau, and R. Korde. *IEEE Trans. Nuc. Sci*, 44:2561–2565, 1997. 81

[114] S.J. Gitomer, R.D. Jones, F. Begay, A.W. Ehler, J.F. Kephart, and R. Kristal. *Phys.Fluids*, 29(2679), 1986. 87

[115] K. Krushelnick, E.L. Clark, R. Allott, F.N. Beg, C.N. Danson, A. Machacek, V. Malka, Z. Najmudin, D. Neely, P.A. Norreys, M.R. Salvati, M.I.K. Santala, M. Tatarakis, I. Watts, M. Zeph, and A.E. Dangor. *IEEE Transactions on plasma science*, 28:1110–1155, 2000. 87

[116] W.P. Leemans, B. Nagler, A.J. Gonsalves, Cs. Toth, K. Nakamura, C.G.R. Geddes, E. Esarey, C.B. Schroeder, and S.M. Hooker. *Nat.Phys*, 2:696–699, 2006. 87

[117] G. Malka, M.M. Aleonard, J.F. Chemin, G. Claverie, M.R. Harston, J.N. Scheurer, V. Tikhonchuk, S. Fritzler, V. Malka, P. Balcou, G. Grillon, S. Moustaizis, L. Notebaert, E. Lefebvre, and N. Cochet. *Phys.Rev.E.*, 66(066402), 2002. 87

[118] A. Maksimchuk, S. Gu, K. Flippo, and D. Umstadter. *Phys.Rev.Lett.*, 84:4108 – 4111, 2000. 87

[119] M. Allen, P.K. Patel, A. Mackinnon, D. Price, S. Wilks, and E. Morse. *Phys.Rev.Lett.*, 93(265004), 2004. 87

[120] R.P. Drake, E.A. Williams, P.E. Young, K. Estabrook, W.L. Kruer, H.A. Baldis, and T.W. Johnston. *Phys.Rev.Lett.*, 60:1018–1021, 1988. 87

[121] R.E. Turner, K. Estabrook, E.A. Drake, E.A. Williams, H.N. Kornblum, W.L. Kruer, and E.M. Campbell. *Physical Review Letters*, 57(14):1725–1728, 1986.

[122] H.A. Baldis, K. Estabrook, and W. Johnston. *Physical Review Letters*, 62(24):2829–2832, 1989.

[123] H. Figueroa, C. Joshi, H. Azechi, N.A. Ebrahim, and K. Estabrook. *Phys.Fluids*, 27(1887), 1984. 87

[124] N.A. Ebrahim, H.A. Baldis, C. Joshi, and R. Benesch. *Phys.Rev.Lett.*, 45:1179–1182, 1980. 87

[125] J.D. Moody, H.A. Baldis, D.S. Montgomery, K. Estabrook, S. Dixit, and C. Labaune. *Journal of fusion energy*, 12(3), 1993. 87

[126] E.G. Gamaly. *Phys.Fluids B*, 5(3765), 1993. 88

[127] A.V. Arefiev, B.N. Breizman, M. Schollmeier, and V.N. Khudik. *Phys.Rev.Lett*, 108(145004), 2012. 88

[128] A.P.L. Robinson, A.V. Arefiev, and D. Neely. *Phys. Rev. Lett.*, 111:065002, 2013. 88

[129] M.H. Key, M.D. Cable, T.E. Cowan, K.G. Estabrook, B.A. Hammel, S.P. Hatchett, E.A. Henry, D.E. Hinkel, J.D. Kilkenny, J.A. Koch, W.L. Kruer, A.B. Langdon, B.F. Lasinski, R.W. Lee, B.J. MacGowan, A. MacKinnon, J.D. Moody, M.J. Moran, A.A. Offenberger, D.M. Pennington, M.D. Perry, T.J. Phillips, T.C. Sangster, M.S. Singh, M.A. Stoyer, M. Tabak, G.L. Tietbohl, M. Tsukammoto, K. Wharton, and S.C. Wilks. *Physics of Plasmas*, 5:1966, 1998. 88

[130] A.J. Mackinnon, Y. Sentoku, P.K. Patel, D.W. Price, S. Hatchett, M.H. Key, C. Andersen, R. Snavely, and R.R. Freeman. *Phys.Rev.Lett.*, 88(215006), 2002. 88

[131] R.J. Gray, D.C. Carroll, X.H. Yuan, C.M. Brenner, M. Burza, M. Coury, K.L. Lancaster, X.X. Lin, Y.T. Li, D. Neely, M.N. Quinn, O. Tresca, C-G. Wahlstrom, and P. McKenna. *New Journal of Physics*, 16:113075, 2014. 110

[132] K.A. Tanaka, R. Kodama, H. Fujita, M. Heya, N. Izumi, Y. Kato, Y. Kitagawa, K. Mima, N. Miyanaga, T. Norimatsu, A. Pukhov, A. Sunahara, K. Takahashi, M. Allen, H. Habara, T. Iwatani, T. Matusita, T. Miyakosi, M. Mori, H. Setoguchi, T. Sonomoto, M. Tanpo, S. Tohyama, H. Azuma, T. Kawasaki, T. Komeno, O. Maekawa, S. Matsuo, T. Shozaki, Ka Suzuki, H. Yoshida, T. Yamanaka, Y. Sentoku, F. Weber, T.W. Barbee Jr., and L. DaSilva. *Physics of Plasmas*, 7:2014–2022, 2000. 111

[133] M. Yoshida, Y. Fujimoto, Y. Hironaka, K.G. Nakamura, K. Kondo, M. Ohtani, and H. Tsunemi. *Applied Physics Letters*, 73:2393, 1998. 111

[134] T. Guo, Ch. Spielmann, B.C. Walker, and C.P.J. Barty. *Rev. Sci. Instrum.*, 72:41, 2001. 111

[135] S.P.D. Mangles, C.D. Murphy, Z. Najmudin, A.G.R. Thomas, J.L. Collier, A.E. Dangor, E.J. Divall, P.S. Foster, J.G. Gallacher, C.J. Hooker, D.A. Jaroszynski, A.J. Langley, W.B. Mori, P.A. Norreys, F.S. Tsung, R. Viskup, B.R. Walton, and K. Krushelnick. *Nature*, 431:535–538, 2004. 111

[136] G. Malka and J.L. Miquel. *Phys.Rev.Lett.*, 77:75–78, 1996.

[137] L.M. Chen, J. Zhang, Q.L. Dong, H. Teng, T.J. Liang, L.Z. Zhao, and Z.Y. Wei. *Phys.Plasmas*, 8:2925, 2001. 111, 113

[138] P. Gibbon and E. Forster. *Plasma Phys. Control. Fusion.* 112

[139] O.L. Landen, D.G. Stearns, and E.M. Campbell. *Phys.Rev.Lett.*, 63:1475–1478, 1989. 112

[140] M. Shahzad, G.J. Tallents, O. Culfa, A.K. Rossall, L.A. Wilson, S.J. Rose, O. Guilbaud, S. Kazamias, M. Pittman, K. Cassou, J. Demailly, O. Delmas, A. Mestrallain, M. Farjardo, and D. Ros. Diagnosis of radiation heating in iron buried layer targets. *14 th International Conference for X-Ray Lasers,In press by Springler*, 2014. 113, 130

[141] H. Teng, J. Zhang, Z.L Chen, Y.T. Li, X.Y. Peng, and J.X. Ma. *Phys.Rev.E*, 67:026408, 2003. 113

[142] Yun-Qian Cui, Wei-Min Wang, Zheng-Ming Sheng, Yu-Tong Li, and Jie Zhang. *Plasma.Phys.Control.Fusion*, 55:085008, 2013. 118

[143] L.A. Wilson, G.J. Tallents, J. Pasley, D.S. Whittaker, S.J. Rose, O. Guilbaud, K. Cassou, S. Kazamias, S. Daboussi, M. Pittman, O. Delmas, J. Demailly, O. Neveu, and D. Ros. *Phys. Rev. E*, 86:026406, 2012. 127

[144] M. Shahzad, O. Culfa, A.K. Rossall, G.J. Tallents, L.A. Wilson, S.J. Rose, O. Guilbaud, S. Kazamias, M. Pittman, K. Cassou, J. Demailly, O. Delmas, A. Mestrallain, M. Farjardo, and D. Ros. Diagnosis of radiation heating in iron buried layer targets. *Under preparation for submission*, 2014. 129

[145] The Center for Xray optics. http://henke.lbl.gov/cgi-bin/filter.pl, July 2014. 129

[146] K. Nazir, S.J. Rose, A. Djaoui, G.J. Tallents, M.G. Holden, P.A. Norreys, J. Zhang P. Fews, and F. Failles. *App.Phys.Lett.*, 69:3686, 1996. 129

[147] D.J. Hoarty, S.F. James, C.R.D. Brown, B.M. Williams, H.K. Chung, J.W.O. Harris, L. Upcraft, B.J.B. Crowley, C.C. Smith, and R.W. Lee. *HEDP*, 6:105–108, 2010. 129